Studies towards Acceleration of Relativistic Electron Beams in Laser-driven Dielectric Microstructures

Dissertation

zur Erlangung des Doktorgrades
am Institut für Experimentalphysik
im Fachbereich Physik
der Universität Hamburg

vorgelegt von

Willi Kuropka

aus Dresden

Hamburg
Dezember 2019

Gutachter/innen der Dissertation	Dr. Ralph W. Aßmann Prof. Dr. Franz X. Kärtner
Zusammensetzung der Prüfungskommission	Dr. Ralph W. Aßmann Prof. Dr. Franz X. Kärtner Dr. Klaus Flöttmann Prof. Dr. Wolfgang Hillert
Vorsitzende/r der Prüfungskommission	Prof. Dr. Günter H. W. Sigl
Datum der Disputation	29. Mai 2020
Vorsitzender des Fach-Promotionsausschusses Physik	Prof. Dr. Günter H. W. Sigl
Leiter des Fachbereichs Physik	Prof. Dr. Wolfgang Hansen
Dekan der Fakultät für Mathematik, Informatik und Naturwissenschaften	Prof. Dr. Heinrich Graener

Eidesstattliche Versicherung

Hiermit versichere ich an Eides statt, die vorliegende Dissertationsschrift selbst verfasst und keine anderen als die angegebenen Hilfsmittel und Quellen benutzt zu haben. Die eingereichte schriftliche Fassung entspricht der auf dem elektronischen Speichermedium. Die Dissertation wurde in der vorgelegten oder einer ähnlichen Form nicht schon einmal in einem früheren Promotionsverfahren angenommen oder als ungenügend beurteilt.

Ort, Datum

Unterschrift

Abstract

In this work an approach to relativistic electron acceleration employing laser-driven dielectric microstructures (DLA) is considered. New DLA designs were developed, a simulation code for efficient DLA simulation was devised, the capabilities of dielectric microstructures as particle beam diagnostic devices were investigated and a laser induced damage threshold measurement setup was implemented and tested.

To leverage well developed near-infrared laser sources new DLAs were designed that are robust against realistic manufacturing tolerances and exhibit a predicted increased electron transmission of up to 44 % of the charge and longitudinal acceptance of around 2 fs, but are still able to produce GV/m acceleration gradients. A great challenge is the numerical simulation of long interaction lengths of electrons with the short drive laser wavelengths present in DLAs due to the high demand in computation resources needed by the large simulation domain compared to the wavelength. A novel method was developed, which is able to efficiently model meter long DLAs without any resonant particle approximations by use of transfer maps generated from a single-period electromagnetic field simulation and a limited set of particle tracking simulations. In PIC simulations hundreds of DLA periods can be modeled using a high performance computing cluster. With the code presented in this work a meter long DLA (hundred thousands of periods) can be simulated on a workstation. This PhD work includes the numerical investigation of particle beam diagnostics capabilities of DLAs, namely as transverse deflecting structures and as new passive and active bunch length measurement devices for ultra-short particle bunches in the sub-femto second regime. All the presented methods are very compact in the particle beam line compared to existing methods.

An experiment was devised to test the designed DLAs by injection of an electron bunch from a conventional state-of-the-art radio frequency accelerator with the potential to show first increase of the average energy of a relativistic electron beam in a DLA device. In contrast all experiments up to today are only modulating the particle beam energy. Finally an experimental setup was designed and implemented to measure the short pulse laser induced damage threshold of DLAs with characterization measurements taken on a bulk material.

Zusammenfassung

Die vorgelegte Arbeit befasst sich mit einem Ansatz zur Beschleunigung von relativistischen Elektronen unter Einsatz von dielektrischen lasergetriebenen Mikrostrukturen. Neue DLA Designs wurden entwickelt, eine effiziente Methode zur numerischen Simulation meterlanger DLA wurde programmiert, die Möglichkeiten der DLA als Teilchenstrahldiagnostik wurden untersucht und ein Experiment zur Messung der Schadenstoleranz gegenüber kurzen Laserpulsen wurde implementiert und getestet.

Um die fortgeschrittene Infrarotlasertechnologie zu nutzen wurden neue DLA-Strukturen entwickelt, welche eine gute Toleranz gegenüber realistischen Fertigungsungenauigkeiten besitzen und eine erhöhte Elektronentransmission von bis zu 44 % zeigen und auch die longitudinal Akzeptanz auf ca. 2 fs erhöhen und gleichzeitig Beschleunigungsgradienten im GV/m-Bereich aufweisen. Eine große Herausforderung in diesem Feld ist die numerische Simulation langer DLA, da der zu modellierende Simulationsraum sehr groß gegen die aufzulösende Wellenlänge ist. In der vorliegenden Arbeit wurde eine neue Simulationsmethode entwickelt um lange DLA-Interaktionen effizient zu modellieren. Meterlange DLAs werden ohne die Annahme einer resonanten Teilcheninteraktion mit Hilfe von Transportabbildungen für jeweils eine DLA-Periode modelliert. Es ist nur eine Simulation des elektromagnetischen Feldes für eine Periode notwendig sowie eine limitierte Anzahl von Simulationen der Trajektorien von Testteilchen. In einer PIC Simulation ist eine Modellierung von einigen 100 Perioden möglich, jedoch nur unter Verwendung eines high performance computing clusters. Die präsentierte Methode kann meterlange DLA (hunderttausende Perioden) auf einer Workstation modellieren. Die Arbeit befasst sich außerdem auf Basis numerischer Simulationen mit dem Potenzial von DLAs zur Teilchenstrahldiagnostik: Als sogenannte „transverse deflecting structures“ und als neue passive und aktive Messung der Länge von Elektronenpaketen im sub-femtosekunden Bereich. Die diskutierten Methoden versprechen sehr hohe Kompaktheit gegenüber der Teilchenstrahltransportlinien im Vergleich zu bereits existierenden Methoden.

Ein Experiment wurde entwickelt um das DLA-Design zu testen. Es sollen Elektronenpakete von einem state-of-the-art Radiofrequenzbeschleuniger in den DLA injiziert werden mit dem Potenzial erste Nettobeschleunigung relativistischer Elektronen in DLA zu zeigen. Alle bisher durchgeführten Experimente haben lediglich die Energie des Teilchenstrahls moduliert. Zuletzt wurde ein Experiment entwickelt und implementiert um die Schadenstoleranz von DLAs bezüglich kurzer Laserpulse zu messen. Der Aufbau wurde mit Hilfe von Messungen an dielektrischen Substraten charakterisiert.

Acronyms

AC	Alternating Current
ACHIP	Accelerator on a CHip International Program
ARES	Accelerator Research Experiment at Sinbad
ASTRA	A Space charge Tracking Algorithm
AXSIS	Frontiers in Attosecond X-ray Science, Imaging and Spectroscopy
CERN	Conseil européen pour la recherche nucléaire
CVBG	Chirped Volume Bragg Grating
CPA	Chirped Pulse Amplification
EA1	Experimental Area 1 at ARES
DAQ	Data AQuisition
DC	Direct Current
DESY	Deutsches Elektronen SYnchrotron
DLA	Dielectric Laser Accelerator
FAU	Friedrich-Alexander-Universität
FEL	Free Electron Laser
FROG	Frequency Resolved Optical Gating
FWHM	Full Width Half Max
Ho:YLF	Holmium doped Ytterbium-Lithium-Floride (crystal)
IP	Interaction Point
LHC	Large Hadron Collider
LWFA	Laser Wake Field Acceleration
PD	Photo Diode
PIC	Particle-In-Cell (code)
PSI	Paul Scherrer Institut
PWFA	Plasma Wake Field Acceleration
RF	Radio Frequency
RMS	Root Mean Square
SINBAD	Short INnovative Bunches and Accelerators at Desy
SPR	Smith-Purcell Radiation
TDS	Transverse Deflecting Structure
TFP	Thin Film Polarizer
TW	Traveling Wave structure

Acknowledgments

I would like to thank Dr. Ralph W. Aßmann and Prof. Dr. Franz X. Kärtner for advising this thesis. Special thanks also to Dr. Ulrich Dorda, Frank Mayet, Dr. Huseyin Cankaya, Dr. Francois Lemery and Daniel Marx for daily close collaboration and contributions to this research. Also I would like to thank all my colleagues from MPY-1 for all the instructional discussions on various topics and Dr. Klaus Flöttmann for answering lots of accelerator physics questions. Very special thanks goes to the Gordon and Betty Moore Foundation for funding this research and the entire ACHIP collaboration that strongly influenced this work, especially to Y. Miao and Johannes Illmer for manufacturing the DLA samples and Joel R. England, Pietro Musumeci and David Cesar for insights on the experiments conducted at UCLA and SLAC. I want to thank DESY and the University of Hamburg for the opportunity to conduct this research. Another very important but sometimes less scientific role in the completion of this work played: Florian Christie, Philipp Amstutz, Christian Henkel, Patrick Rauer, Immo Bahns and Max Kellermeier. Finally I want to thank my family and friends for their support and especially the wonderful Lioba Jarju.

Contents

List of Figures

List of Tables

Introduction

In this work dielectric gratings were explored with respect to their use as laser driven electron accelerators and related electron beam diagnostics. In chapter 1 the work is motivated with a short historical overview of particle accelerators and their use cases. An introduction to the novel accelerator technologies in current research and development is given. Also the capabilities of the state-of-the-art technology and the challenges for future development are reviewed. The dedicated long-term accelerator research and development facility SINBAD at DESY is presented. Chapter 2 gives the relevant theory on particle accelerators and dielectric gratings as well as some basic considerations on laser induced damage in dielectrics, which pose the major limitations on achievable acceleration gradients in these kind of structures.

Chapter 3 is concerned with the numerical modeling of dielectric accelerating structures and the interaction with electrons. New designs for grating type dielectric laser accelerators were devised to balance achievable charge transmission and accelerating gradients. A DLA simulation code is also presented that attacks the challenge of modeling large interaction lengths much greater than the drive laser wavelength making the design of meter long DLAs possible.

In chapter 4 the numerical models were used to investigate the diagnostic capabilities of dielectric gratings employed as transverse deflecting structures and as a passive bunch length diagnostic. The measurement of sub-fs particle bunch lengths and longitudinal charge profiles poses an important challenge in accelerator physics and ultra-fast science that can potentially be tackled using passive or laser driven dielectric microstructures. This is especially challenging for high particle energy facilities like free electron lasers where the radio frequency transverse deflecting structures currently in use to conduct these measurements are rather expensive.

In chapter 5 an experiment using an externally generated electron bunch is described and the performance is predicted using various numerical methods. Due to the unique properties of the conventional radio-frequency accelerator used for the experiment it is possible to show net energy gain in a dielectric laser accelerator at relativistic electron energies with acceleration gradients of around 1 GV/m. This is the first net energy gain experiment using DLAs with relativistic electrons proposed, to our best knowledge. The experiments with relativistic electron beams conducted earlier were only able to show the modulation of particle energy. Using pulse front tilt technology and a mm long fused silica DLA record absolute energy gains of MeV are predicted.

Chapter 6 contains the description and documentation of a preliminary short-pulse laser-induced damage threshold experiment for dielectrics. An automated setup was designed to enable the necessary row-testing in an efficient manner. This important

topic poses the main limitation on achievable acceleration gradients in DLAs. Experimental data at the desired laser wavelengths and laser pulse lengths for microstructured dielectrics is not available in the literature.

Finally in chapter 7 the work is concluded and an overview on the potential of the conducted research is given. For each topic a point of view is elaborated on how the research can be continued.

1 Particle Accelerators and their Future

This chapter gives a short overview on particle accelerator technology and why the research on novel techniques for particle acceleration is a relevant research topic. The dedicated accelerator research and development facility SINBAD at DESY is presented as well as the relevant equipment for this work. Also two major candidates for novel particle acceleration, plasma acceleration and dielectric laser acceleration, are briefly introduced in this chapter.

1.1 Charged Particle Acceleration

The first particle accelerators were the cathode-ray tubes invented by Karl Ferdinand Braun around 1900. It is a direct current device that accelerates so-called cathode rays to an anode. The cathode rays were later found to be electrons. Vacuum tubes became the technology from which the television was derived. DC voltage devices found their peak in the van-der-Graaff- and Cockcroft-Walton-accelerator types which can produce particle beams in the MeV regime and were a crucial tool used for early nuclear physics in the 1930s [1].

The first radio frequency (RF) based charged particle accelerators [2, 3] paved the way to high-performance, high-energy, large-scale facilities in the 1930s. These were longer linear vacuum tubes with so-called drift tubes. A high frequency AC voltage is applied to the drift tubes so that the particles are accelerated between the tubes. The length of the dirft tubes is increased as the particle velocity increases leading to long devices for high particle energies. To achieve a more compact setup the cyclotron [4] was invented. A circular machine that uses a big electromagnet to force particle beams on spiral trajectories. The circular shape makes it possible to use the same acceleration RF device repeatedly. An AC voltage is used to accelerate the particles in a gap between two electrodes. The revolution frequency does not depend on the particle energy for non-relativistic energies. No high-voltage is necessary but rather a constant frequency voltage oscillator. The resulting particle beam from the AC accelerators is inherently bunched. Metallic resonators (standing wave cavities) or disk-loaded waveguides with high quality factors are used to achieve high acceleration voltages with moderate power levels. Due to the circular machine the expensive RF equipment is used very efficiently, since the particle beam passes it often.

A very popular version of a circular accelerator is the synchrotron [5]. The field strength of the magnets forcing the particle beam on a ring-like trajectory is increased with the particle energy, thus keeping the orbit of the particle beam constant. A very

important concept of the synchrotron is the decoupling of the machine components into the different beam line elements, improving scalability.

The largest particle accelerator is the storage ring Large Hadron Collider (LHC) at CERN with a 27 km circumference. Storage rings are optimized for particle beam lifetime whereas synchrotrons are used for rapid particle acceleration. The biggest facilities leverage the properties of superconductors to build bending magnets strong enough to keep the radii of the machines reasonable. The particle beam requirements are derived from the necessity to have high interaction rates and as high as possible particle energy as well as precise control over it. So what is needed are small transverse beam sizes and emittances and a high peak current. Since the interaction rates are still small compared to the number of particles per bunch, preserving the particle beam in a storage ring makes the particle physics experiments significantly more efficient.

Many of the large scale particle accelerators nowadays are synchrotron radiation sources. Also High peak currents and short bunches are important, since these correlate to intensity and pulse length of the produced radiation.

X-ray radiation generation is the major application nowadays driving innovations in many fields from solid state physics and material science to biology, pharmacology and medicine. The most advanced circular machines for that application are diffraction limited storage rings like MAX IV [6] and the planned PETRA IV [7]. They are able to produce transversely coherent radiation due to the high transverse beam quality that can be achieved. The light pulse lengths produced are in the order of pico-seconds.

The new generation light sources, free electron lasers [8, 9], are able to deliver (partially) longitudinally coherent light and x-ray pulse lengths below 100 fs [10, 11]. Particle energies in the GeV regime are most suitable to reach the short wavelengths needed for diffraction experiments. The accelerator technology also went superconducting for the acceleration cavities [12] to achieve higher quality factors and higher efficiency. FELs can use the lower wall current losses in superconducting cavities to run a quasi-continuous high average power radiation output [13].

Higher particle energies propose various challenges onto circular particle accelerators. For light particles like electrons and positrons the main limiting factor are synchrotron radiation losses. The smaller the ring and the higher the particle energy the higher are the losses per revolution around the ring. So free electron lasers and recent collider designs [14] for electrons and positrons are linear designs minimizing synchrotron radiation losses.

For hadrons with particle energies desired for particle physics experiments the limiting factor for circular machines is the maximum achievable dipole magnet strength to force the beam on smaller radii. The superconducting magnets at LHC can produce magnetic fields of 8.3 T [15]. Although at the LHC synchrotron radiation from the proton beam is detectable it is not producing significant losses but rather radiation protection challenges [16].

One of the strategies to achieve higher particle energies and better beam qualities has been enlarging the facilities. Though the accelerator community is confident that even larger machines are possible to be implemented [17], other directions of research

are important to be considered. Especially securing the funding for the larger machines has been challenging in the past [18].

New approaches try to reduce the footprint of the facilities significantly. One of the limiting factors for the size of the machines is the maximum achievable acceleration gradient. The state-of-the-art RF technology in the X-band regime (12 GHz) is able to produce gradients around 100 MV/m [19]. The superconducting Tesla technology used in the EuropeanXFEL [11] can achieve gradients of 40 MV/m. The main limitation for high accelerating gradients in charged particle acceleration structures are break down phenomena of the materials used. Most modern RF accelerators operate at L-band (1.3 GHz) or S-band (3 GHz) frequencies [20]. RF breakdown, pulse heating and field emission are the main issues with metallic structures going to high acceleration gradients [21]. It is obvious that kilometer long facilities are needed to get into the TeV particle energy regime with the recent RF technology in a linear machine.

A few approaches are being researched towards the goal of high-gradient particle accelerators, trying to leverage the progress that has been achieved in laser science and technology. The recent laser technology is able to produce very high field strengths. Unfortunately these free space laser beams cannot be used directly to linearly accelerate particles. The laser fields have to be transformed using different methods. Several methods are being researched that can be used to accelerate charged particles with high acceleration gradients decreasing the drive wavelengths and using different approaches for the transformation of the fields, even ponderomotive higher order effects in free space [22]. Plasma based acceleration and dielectrics based acceleration are further discussed in the following sections.

The high acceleration gradients and short electron bunch lengths achievable can lead to very compact devices also opening up new applications for electron accelerators. For example ultra-fast electron diffraction in the MeV particle energy regime as well as electron microscopy. Also synchrotron radiation sources for applications where only low photon flux is needed as in material inspection for electronics production.

1.2 SINBAD and ARES

1.2.1 SINBAD

Short and INnovative Bunches and Accelerators At Desy (SINBAD) is a long-term dedicated accelerator research and development facility at DESY Hamburg. It is situated in the infrastructure of a former synchrotron radiation source. It will host several independent experiments covering a broad range of novel particle acceleration technologies. The two initial experiments starting operation in 2019/20 will be The Accelerator Research Experiment at SINBAD (ARES) [24] and Frontiers in Atto-second X-ray Science: Imaging and Spectroscopy (AXSIS) [25]. AXSIS is an European Research Council funded project to implement a compact THz-driven electron accelerator to drive an inverse Compton-scattering X-ray source. It is foreseen to implement additional experiments over the next few years including research on a kHz repetition rate TW class laser system

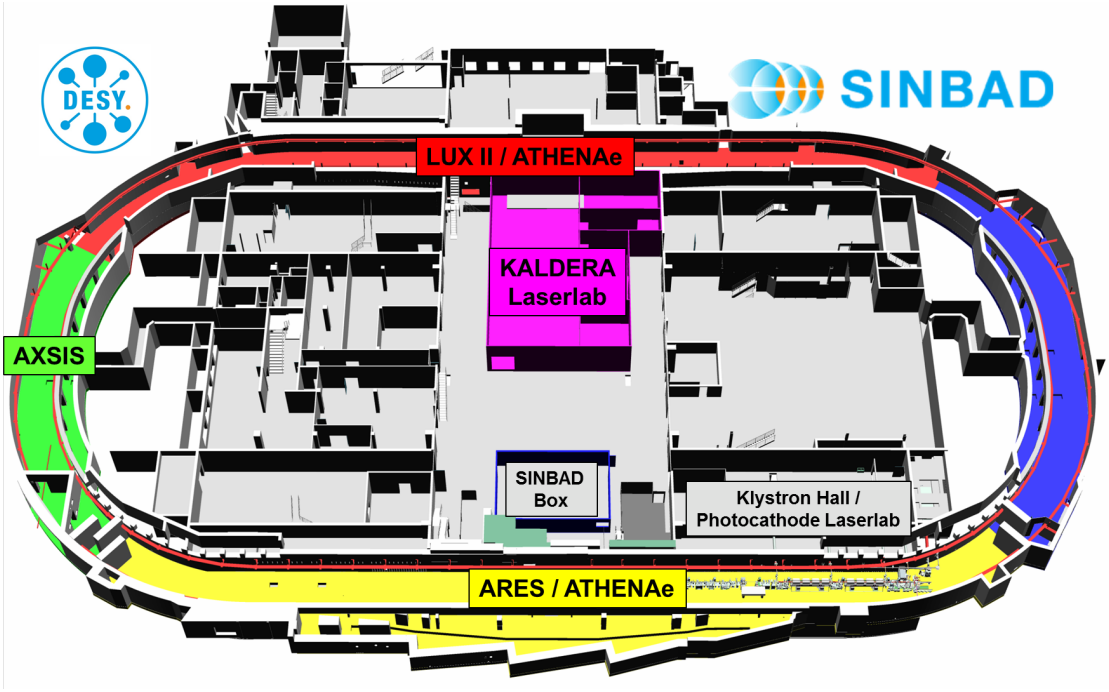

Figure 1.1: An overview of the SINBAD facility with the foreseen experiments AXSIS, ARES, KALDERA and LUX II. The DLA experiments are foreseen to be carried out at ARES. Figure taken from the accelerator research and development at DESY website [23].

(KALDERA) and extending the LUX activities. An overview of the SINBAD facility in the future state can be found in figure 1.1.

1.2.2 ARES

ARES is a normal conducting S-band radio-frequency electron linear accelerator focused on studying various compression techniques to produce sub-fs electron bunches and injecting them into novel particle accelerator structures.

ARES' operates at a frequency of 2.998 GHz. Figure 1.2 shows a CAD rendering of the linac and a schematic of the accelerator area relevant for first DLA experiments is given in figure 1.3. It is planned to reach particle energies of up to 155 MeV by means of two traveling wave copper structures. Mainly two bunch compression techniques will be used to reach ultra-short bunches in the (sub-)fs regime. The first is velocity bunching, in which the particle bunch is set off-crest of the accelerating field in the first traveling wave structure to achieve a longitudinal chirp in particle energy. Since the particle energy is still low the different particle velocities in the head and the tail of the bunch will lead to a longitudinal focus in the second traveling wave structure. There the particle energy is significantly increased by setting the electron bunch on the crest of the accelerating

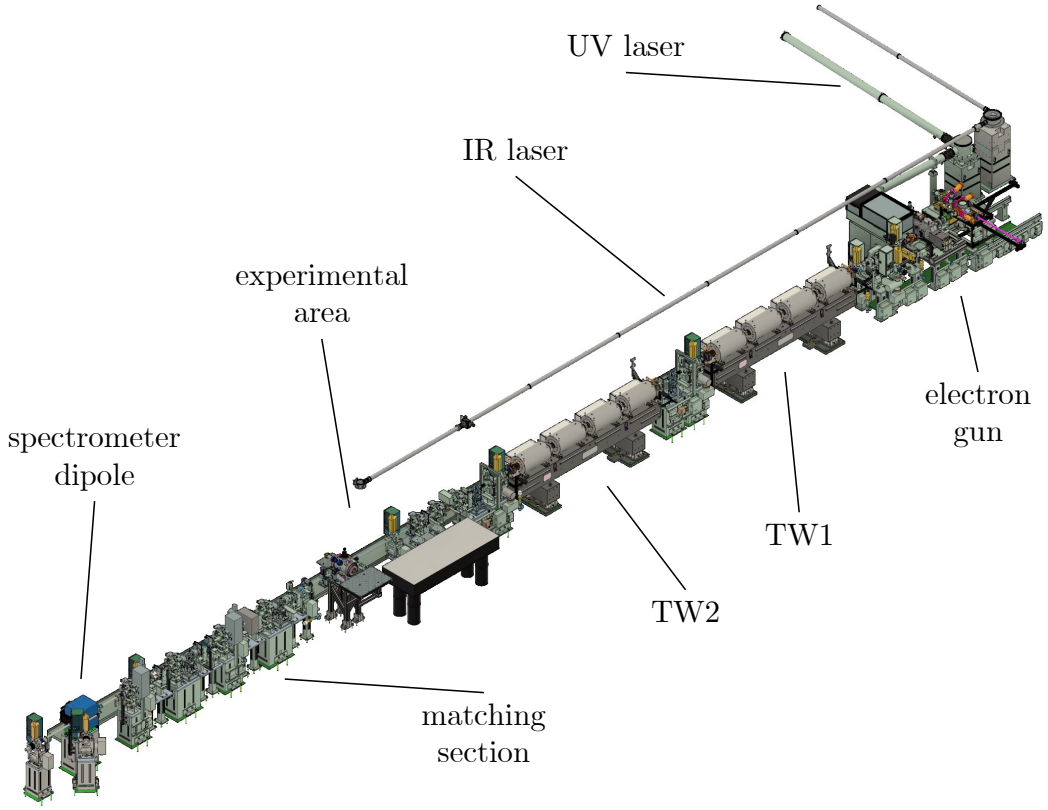

Figure 1.2: Overview of the ARES linac. The ultra-violet (UV) laser beam line leads from the photocathode laser laboratory to the cathode of the electron gun. Downstream of the gun a solenoid magnet and the low energy electron beam diagnostic devices are installed. Two traveling wave structures (TW1 and TW2) will be used to accelerate the electron beam. A focusing quadrupole triplet for beam matching to the experimental area is downstream of the second traveling wave structures. It is followed by the experimental area which comprises a multi-purpose vacuum chamber and an optical table. Before the energy spectrometer dipole a set of four quadrupoles is installed to match the beam.

fields making the particle velocities in the bunch approximately equal and preserving the short bunch length. This technique allows simultaneous compression and acceleration of non-yet-fully-relativistic beams by a shear in longitudinal phase space. This is the technique that will be employed for the DLA experiments.

Longitudinal compression can also be achieved using again a longitudinal chirp of the electron bunch and dispersion in a magnetic chicane, leading to a dependence of the path length on electron energy. The longitudinal phase space can be further manipulated using a collimator in the dispersive section of the chicane. An overview of the electron

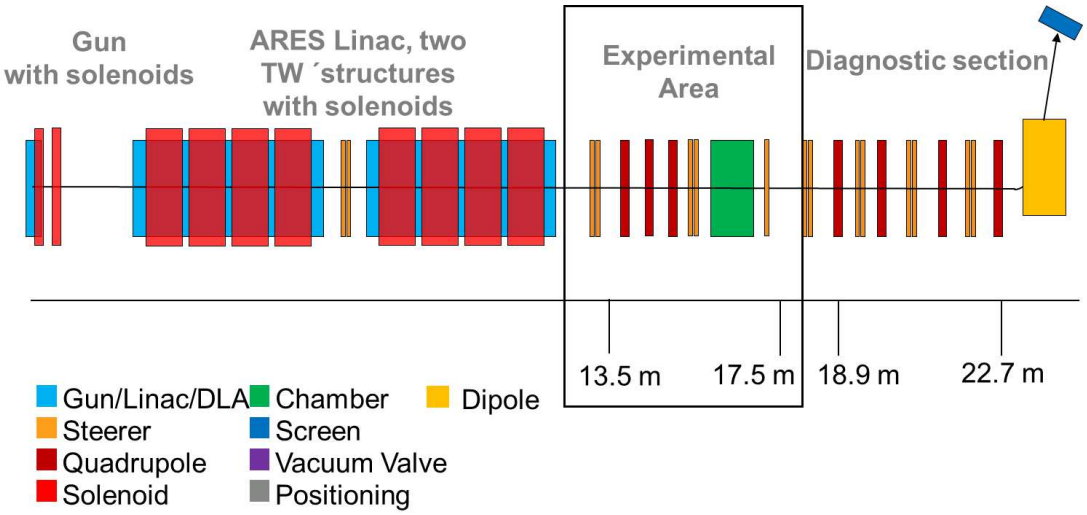

Figure 1.3: An overview of the relevant section of the ARES linac. The experimental area is located behind two traveling wave accelerating structures. Figure taken from [26] by the author.

Table 1.1: ARES Electron Beam Parameters

Energy	100 MeV (incl. Bunch compression)
Charge	0.05 to 20 pC typically (up to 1 nC)
Repetition rate	Single pulse @ 50 Hz
Bunch length	few fs to sub-fs
Transverse norm. emittance	< 0.5 mm mrad
Arrival time jitter	< 10 fs RMS

beam parameters achievable in simulations can be seen in table 1.1.

1.2.3 Near Infrared Laser Source

ARES is equipped with a near infrared laser source. A Holmium fiber laser oscillator synchronized to the master oscillator of ARES seeds a Ho:YLF amplifier system from Q-peak. It consists of a band-width enhanced multi-pass amplifier and a single pass amplifier stage as depicted in figure 1.4. The amplifier is pumped by a 50 W IPG Thulium pump laser. It can deliver 1 kHz or 5 kHz repetition rates. The amplifier is a chirped pulse amplification system [27] equipped with chirped volume bragg gratings as dispersive elements. The compressed laser pulses exhibit a pulse length of 3 ps [28]. A Kagome-fiber is available for spectral broadening and further pulse compression. Pulse lengths of 0.5 ps can be achieved [29]. In table 1.2 the achievable output laser parameters are listed. Output energies are shown in figure 1.5 and the spectral pulse properties are

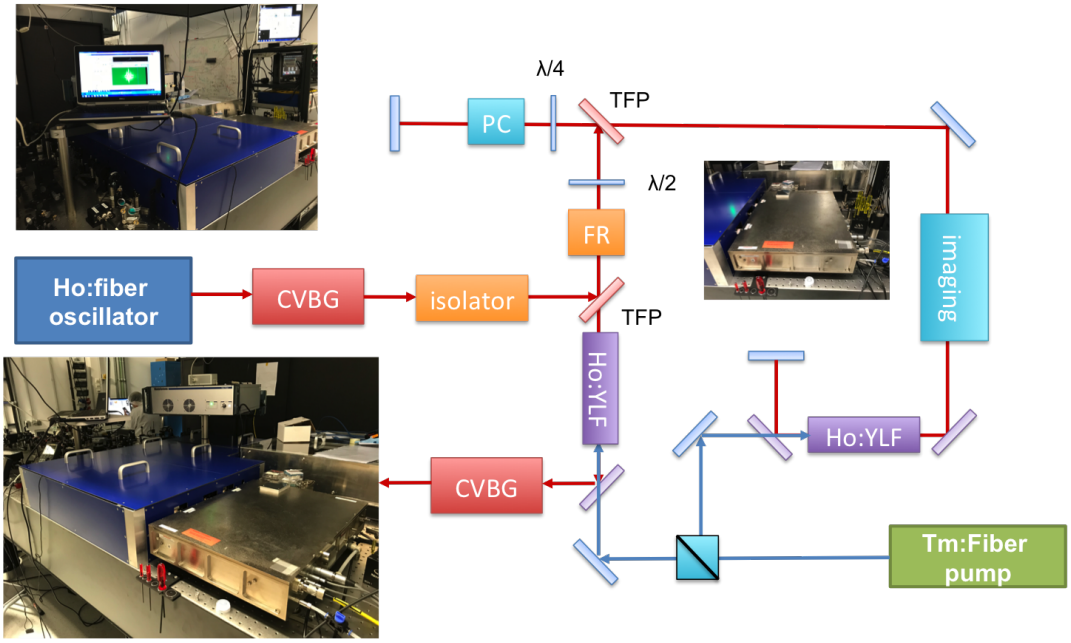

Figure 1.4: Scheme of the Holmium amplifier system (courtesy Huseyin Cankaya). A Holmium fiber laser synchronized to the ARES master oscillator is used to seed a two stage Ho:YLF amplifier system. Chirped volume bragg gratings (CVBG) are used to decompress the seed laser pulse before and to compress the output pulse after amplification. An isolator attenuates the back reflection to the seed. Stage one is a multi-pass amplification using a pulse picker comprised of a Faraday-rotator (FR), thin-film polarizer (TFP), half and quarter wave plates controlled by a pockels cell (PC) that is switched by a high-voltage power supply. The active medium is the Ho:YLF crystal on the right side. It is followed by a single-pass amplifier comprised of the Ho:YLF crystal on the left side. Both stages are pumped by a 50 W Thulium fiber laser. The photographs show the system in the laboratory.

shown in figure 1.6.

Table 1.2: Ho:YLF Amplifier System

	Amplifier	**Kagome-fiber**
Output energy (mJ)	1.9	0.5
Repetition rate (kHz)	1 or 5	1 or 5
Pulse length FWHM (ps)	3	0.5

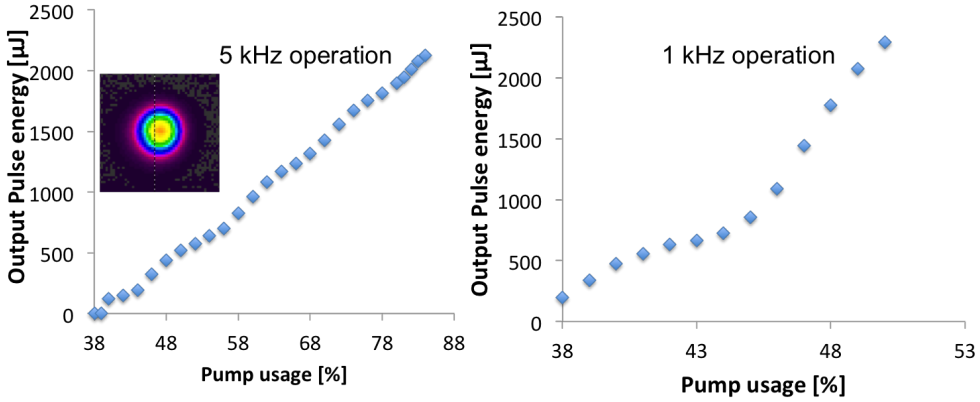

Figure 1.5: Output pulse energy of the Ho:YLF amplifier over pump laser power in percent. On the left the data is plotted for 5 kHz operation and on the right for 1 kHz. The inlay on the left shows a Pyrocamera image of the transverse beam profile. The maximum pump laser power is 50 W. (courtesy H. Cankaya, CFEL)

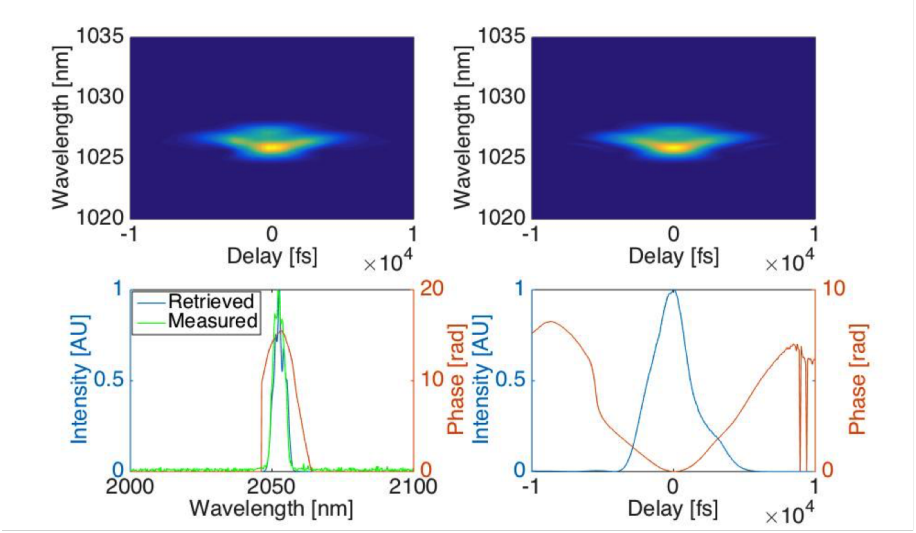

Figure 1.6: FROG analysis of the compressed output pulse from the Ho:YLF amplifier. The upper left plot shows the measured FROG trace and the upper right plot the retrieved trace. The lower left plot shows the measured and retrieved spectra of the pulse and the lower right plot the temporal pulse profile. (courtesy H. Cankaya, CFEL)

1.3 Plasma Acceleration

A plasma is an ionized gas that consists of ions and electrons. It is macroscopically neutral but due to the large mass differences between the ions and the electrons a perturbation of the plasma by an external electromagnetic field can lead to oscillations of the electrons and local, temporal charge separation. By injecting a laser pulse or charged particle bunch into the plasma a propagating plasma wave can be created. The charge separation in the wake of this wave can lead to very strong electromagnetic fields. The wake fields can be used to accelerate charged particles [30, 31]. The achievable maximum acceleration fields can be as high as hundreds of GV/m with the current absolute energy record for an electron beam of 7.8 GeV within a 20 cm plasma capillary at the BELLA facility in Berkeley [32].

The external perturbation driver can be a laser pulse or a particle bunch injected into the plasma. This leads to the differentiation of LWFA - laser wake field acceleration and PWFA - plasma wake field acceleration. Depending on the properties of the driver and the surrounding plasma the accelerated electrons can be gathered from the plasma itself, which is called internal injection. Alternatively a witness bunch is injected behind the driver and is accelerated in the wake field which is called external injection.

DESY is largely involved in the research effort with LUX [33], an experiment to probe the radiation generation capabilities of LWFA and internal injection. Also, FLASHforward [34] is a PWFA experiment situated within the FLASH free electron laser. It can use internal injection or the GeV electron beam from the FLASH injector as external beam. An external injection LWFA is in commissioning at the REGAE facility [35].

The SINBAD facility and ARES will be one of the cornerstones of ATHENA [36]. It is a collaborative project within the Helmholtz Association to bring the new plasma based technologies to user readiness as radiation source injectors. The main areas to improve are the shot-to-shot and long term stability of the plasma elements and high peak power drive laser systems. Also the capturing of the particle beams after the plasma interaction is a challenge.

1.4 Dielectric Laser Acceleration and ACHIP

Another approach to make high laser fields usable for particle accelerators are dielectric laser accelerators (DLA). Dielectric structures are illuminated with coherent light from a laser source. The near fields of these structures can be used to accelerate particles. The following work is focused on an approach looking primarily into phase grating type structures driven by a near infrared laser source. The idea to use the coherent radiation from a MASER (microwave amplification by stimulated emission of radiation) [37] to accelerate charged particles was proposed shortly after its development [38]. But the highest intensities in the peta-watt peak power regime [39] are achieved by the LASER (light amplification by stimulated emission of radiation) in the near-infrared wavelength regime.

The use of dielectrics and their favorable properties is not limited to the near-infrared

and optical regime. The AXSIS project uses THz-fields to drive dielectric lined metallic waveguides aiming at acceleration gradients of hundreds of MV/m to drive a Compton-scattering source [25].

Dielectric laser accelerators use the high damage threshold of dielectric materials in the near-infrared to optical regime to take advantage of the high fields achievable by the laser sources. No high quality factors, compared to metallic cavities are involved, which makes the use of short intense laser pulses possible. The achievable gradients lie in the single digit GV/m regime. With an experimentally demonstrated record peak gradient of 1.8 GV/m [40].

A dedicated 5-year research effort was launched after initial proof-of-principle experiments at Friedrich-ALexander-Universität Erlangen for non-relativistic electrons [41] and at the Stanford Linear Accelerator Center (SLAC) for relativistic electrons [42]: The ACHIP Collaboration (Accelerator on a Chip International Program) [43, 44] funded by the Gordon and Betty Moore Foundation. Its goals are to push the frontiers of DLA technology for relativistic and non-relativistic electron acceleration and to develop a compact multi-stage prototype reaching the MeV electron energy regime. Figure 1.7 shows a photograph of a fused silica grating type DLA device for a laser wavelength of 800 nm as used in the first experiments.

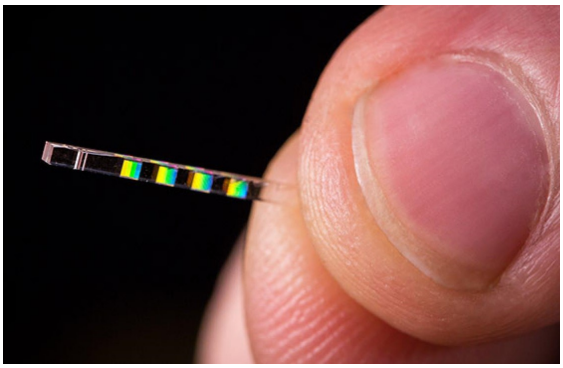

Figure 1.7: Fused silica grating type DLA for 800 nm drive laser wavelength as used in the first DLA experiments at SLAC and UCLA. Four gratings can be seen as the yellow-to-blue areas from visible light diffraction. The narrow area on left tip are alignment channels. Picture taken from the ACHIP collaboration website [44].

This work aims at the continuation of the efforts to investigate relativistic electron acceleration and manipulation. All relativistic experiments conducted previously were only able to interact with only a small fraction of the electron beam inside the DLA. The electron bunches injected were significantly longer than the drive laser wavelength only modulating the electron beam energy. The experiments proposed and simulated in this work aim at significantly higher electron transmission and at showing a mean gain in electron bunch energy. Figure 1.8 illustrates the effective and maximum acceleration gradients and also the mean energy gains achieved in the experiments conducted to date

and the predicted performance of the DLA experiment proposed in this work.

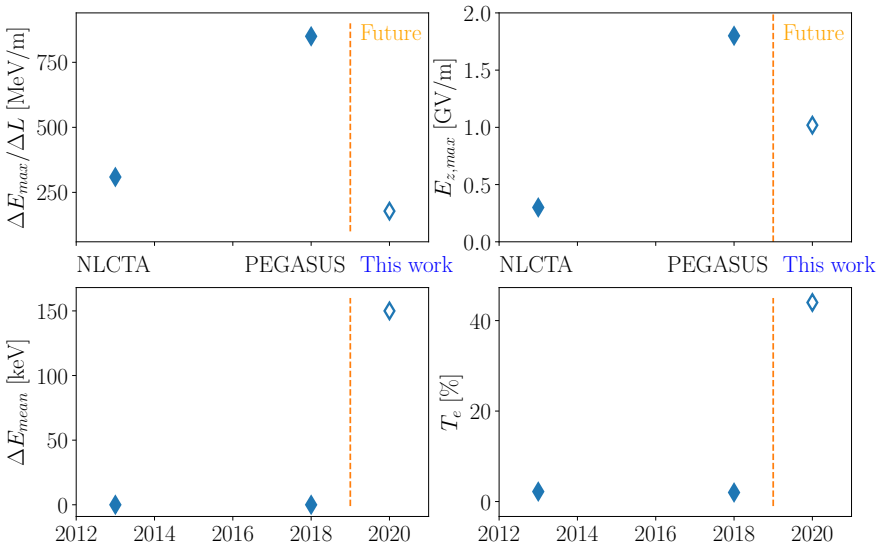

Figure 1.8: The upper left plot shows the maximum energy change of an electron interacting with the DLA ΔE divided by its effective length ΔL. On the upper right plot the maximum accelerating field $E_{z,max}$ is plotted. The lower left plot shows the mean energy gain of an electron bunch interacting with the DLA ΔE_{mean} and the lower right plot shows the electron beam transmission T_e through the DLA aperture. The filled diamonds are the experiments at NLCTA [42] and PEGASUS [45, 40] and the blank diamnods are the predicted performance of the experiment proposed in this work.

The collaboration comprises the Stanford University, FAU Erlangen, Purdue University, École Polytechnique Fédérale de Lausanne (EPFL), Technische Universität Darmstadt, University of California Los Angeles (UCLA), National Tsing Hua University and the national laboratories Deutsches Elektronen Synchrotron (DESY), Paul Scherrer Institut (PSI), Stanford Linear Accelerator Center (SLAC), Los Alamos National Laboratory (LANL) and also the companies Tech-X Corporation and Hamamatsu Corporation. The research activity covers the whole spectrum from development of the structure design and particle source designs, simulation of electrodynamics for power transport and particle dynamics, nano-fabrication of the structures and electron sources to the experimental investigation of the DLAs by particle beams from conventional RF accelerators.

The smaller dimensions of the DLA devices compared to the RF machines are one of the challenges inherent to this technology. For fabrication the techniques from the

semiconductor industry can be leveraged to produce low cost devices, once the manufacturing recipes are developed. The short wavelengths limit the free apertures for particle beams and pose strong limits for the longitudinal particle bunch length. Diagnostics and beam manipulation capabilities have to be integrated into the devices with the appropriate precision and are another important research topic within the collaboration [46, 47]. The dielectric based structures investigated in this work can also be attractive candidates for high-resolution, low-cost particle beam diagnostic devices for RF based particle accelerators.

One of the goals of ACHIP is the implementation of a multi-stage GV/m gradient on-chip prototype that can reach an absolute energy gain in the MeV regime for relativistic and non-relativistic electrons. The second goal is to study capabilities of dielectric structures for radiation generation, beam manipulation and sub-fs particle beam diagnostics. This work is a precursor for the relativistic electron acceleration goal by designing an experiment to show net energy gain of an ultra-short electron bunch in a DLA and exploring the achievable beams from long interaction DLAs. It also pushes the second goal by presenting investigations of the particle beam diagnostic capabilities of DLAs.

2 Theory of Dielectric Micro-scale Accelerators

This chapter will give a brief overview of the physical base and theoretical background of dielectric structure based charged particle acceleration techniques. At first a quick introduction to the terms needed from electrodynamics and accelerator physics is given. The second section provides a short introduction to the various applicable dielectric schemes. For a detailed review refer to [48]. The third part will illustrate the dielectric grating scheme investigated in this work in more detail. The chapter continues with the fourth section about the theory for short-pulse, laser-induced damage to dielectrics. The damage due to short pulse laser irradiation is usually the limiting factor in achievable acceleration gradient for the devices discussed here.

2.1 Accelerator Physics Introduction

A short overview is given here to introduce the relevant concepts and terms. The following section is mainly based on the textbooks [49] and [50]. Different sources are cited where used.

2.1.1 Maxwell's Equations

This section is partially based on the authors master thesis [51].

Accelerator physics is concerned with the dynamics of charged particles in electromagnetic fields. Thus, the starting point are Maxwell's equations, which will be formulated in a fashion suited to describe the behavior of charged particles accurately:

$$\nabla \cdot \mathbf{D} = \rho \tag{2.1}$$

$$\nabla \cdot \mathbf{B} = 0 \tag{2.2}$$

$$\nabla \times \mathbf{E} = -\frac{\partial}{\partial t}\mathbf{B} \tag{2.3}$$

$$\nabla \times \mathbf{H} = \mathbf{J} + \frac{\partial}{\partial t}\mathbf{D} \tag{2.4}$$

The ∇ is the nabla or del operator and the bold quantities represent vectors. In the following three components on a cartesian coordinate system are assumed. Gauss' law

in equation 2.1 states that the charge density distribution ρ is the source of the electric displacement or electric flux density $\mathbf{D}$. The magnetic flux density $\mathbf{B}$ has no sources, as stated in equation 2.2. Faraday's law 2.3 describes that a change of the magnetic flux density $\frac{\partial}{\partial t}\mathbf{B}$ leads to a curl in the electric field $\mathbf{E}$, which is connected to the induction process. The fourth equation 2.4 is Ampere's law with the added influence of the electric displacement $\mathbf{D}$. It states that the source of curls in the magnetic field $\mathbf{H}$ are caused by electric currents $\mathbf{J}$ and changes over time in electric displacement $\frac{\partial}{\partial t}\mathbf{D}$.

The flux densities and fields are connected by the permittivity ϵ and permeability μ. $\epsilon_0 = 8.854 \times 10^{-12}\,\mathrm{A\,s\,V^{-1}\,m^{-1}}$ and $\mu_0 = 4\pi\,\mathrm{N\,A^{-2}}$ are the permittivity and permeability of vacuum. The properties of the background material have an effect on the electric and magnetic fields and are included by introducing the polarization $\mathbf{P}$ and magnetization $\mathbf{M}$. The polarization models the electric dipole moment per volume inside the material. And accordingly the magnetic dipole moment per volume is modeled by the magnetization.

$$\mathbf{D} = \epsilon_0\mathbf{E} + \mathbf{P} \tag{2.5}$$

$$\mathbf{B} = \mu_0(\mathbf{H} + \mathbf{M}) \tag{2.6}$$

The polarization and magnetization depend again on the fields. In the following dependency they are limited to the first order:

$$\mathbf{P} = \epsilon_0\chi_e\mathbf{E} \tag{2.7}$$

$$\mathbf{M} = \chi_m\mathbf{H} \tag{2.8}$$

The first order electric susceptibility χ_e and magnetic susceptibility χ_m are frequency dependent proportionalities. Higher order terms and polarization dependencies can be modeled expanding equations 2.7 and 2.8. Substituting equation 2.7 into 2.5 and 2.8 into 2.6 leads to:

$$\mathbf{D} = \epsilon_0(1 + \chi_e)\mathbf{E} = \epsilon_0\epsilon_r\mathbf{E} \tag{2.9}$$

$$\mathbf{B} = \mu_0(1 + \chi_m)\mathbf{H} = \mu_0\mu_r\mathbf{H} \tag{2.10}$$

where

$$\epsilon_r = (1 + \chi_e) \tag{2.11}$$

$$\mu_r = (1 + \chi_m) \tag{2.12}$$

Generally the resulting quantities relative permittivity ϵ_r and relative permeability μ_r

are tensors and depend on the direction of the electric and magnetic fields. The following derivation is limited to isotropic, homogenous materials, which makes these quantities scalars. The materials considered in this work exhibit magnetic properties very close to those of vacuum, consequently $\mu_r = 1$.

2.1.2 Electromagnetic Potentials

A practical extension of these concepts is the expression of the magnetic flux density by a vector potential $\mathbf{A}$. This is possible due to equation 2.2.

$$\mathbf{B} = \nabla \times \mathbf{A} \tag{2.13}$$

Using equations 2.3 and 2.13 one can also describe the electric field using potentials:

$$\nabla \times \mathbf{E} = -\frac{\partial}{\partial t}\mathbf{B} = -\frac{\partial}{\partial t}(\nabla \times \mathbf{A}) \tag{2.14}$$

This can be rearranged to give:

$$\nabla \times (\mathbf{E} + \dot{\mathbf{A}}) = 0 \tag{2.15}$$

With the $\dot{}$ notation as the first derivative with respect to time. A possible solution is:

$$\mathbf{E} = -\frac{\partial \mathbf{A}}{\partial t} - \nabla\varphi \tag{2.16}$$

The gradient of a scalar potential was added, which is still compatible with Maxwell's equations. This makes it possible to impose a suitable condition on the scalar potential function φ. Now combining the modified Ampere's law 2.4 with equations 2.9 and 2.10 yields:

$$\nabla \times \mathbf{B} = \mu_0\mu_r\mathbf{J} + \epsilon_0\epsilon_r\mu_0\mu_r\dot{\mathbf{E}} \tag{2.17}$$

Substituting equations 2.13 and 2.15 and using the relation $\epsilon_0\mu_0 = 1/c^2$, where c is the vacuum speed of light, yields the equation as an expression of the potentials:

$$\nabla \times (\nabla \times \mathbf{A}) = \mu_0\mu_r\mathbf{J} + \frac{\epsilon_r\mu_r}{c^2}(-\ddot{\mathbf{A}} - \nabla\dot{\varphi}) \tag{2.18}$$

Using the algebraic relation $\nabla \times (\nabla \times \mathbf{A}) = \nabla(\nabla\mathbf{A}) - \nabla^2\mathbf{A}$ and rearranging leads to the following equation:

$$\nabla^2\mathbf{A} - \frac{\epsilon_r\mu_r}{c^2}\ddot{\mathbf{A}} = -\mu_0\mu_r\mathbf{J} + \nabla(\nabla\mathbf{A} + \frac{\epsilon_r\mu_r}{c^2}\dot{\varphi}) \tag{2.19}$$

Imposing the condition $\nabla\mathbf{A} + \frac{\epsilon_r\mu_r}{c^2}\dot{\varphi} = 0$ on the scalar potential function φ yields the wave equation:

$$\nabla^2\mathbf{A} - \frac{\epsilon_r\mu_r}{c^2}\ddot{\mathbf{A}} = -\mu_0\mu_r\mathbf{J} \tag{2.20}$$

Similarly a wave equation for the scalar potential can be derived:

$$\nabla^2\varphi - \frac{\epsilon_r\mu_r}{c^2}\ddot{\varphi} = -\frac{\rho_f}{\epsilon_0} \tag{2.21}$$

These second order differential equations might be integrated to derive the actual potentials. The vector potential $\mathbf{A}$ is defined by the placement of the currents in the considered space and the scalar potential φ is defined by the charge density distribution in the considered space. For arbitrary spatial and time varying current and charge density distributions the integration might be far from trivial and only approachable via numerical methods. By knowing these potentials the fields can be calculated as shown above. These relations allow a design of fields to guide beams and make it possible to calculate the fields from charged particle beams. The expression of the electromagnetic fields in the form of a vector potential and a scalar potential together with the description of the (moving) charged particles as charge and current densities will allow leveraging the Hamiltonian formalism to derive the dynamics of particle ensembles in these fields.

2.1.3 The Equations of Motion for a Single Charged Particle

The interaction of charged particles with electromagnetic fields is described by the Lorentz force F_L, where q is the electrical charge of the particle:

$$\mathbf{F_L} = q(\mathbf{E} + \mathbf{v} \times \mathbf{B}) \tag{2.22}$$

Of interest are the changes of the properties of the charged particle over time. Thus, the change in particle momentum, which guides its motion and the kinetic energy are given by:

$$\Delta p = \int \mathbf{F_L} dt \tag{2.23}$$

$$\Delta E_{kin} = \int \mathbf{F_L} d\mathbf{s}. \tag{2.24}$$

Writing the kinetic energy and using equation 2.22, splitting the sum under the integral and substituting $d\mathbf{s} \rightarrow \mathbf{v}dt$ amounts to:

$$\begin{aligned} \Delta E_{kin} &= \int \mathbf{F_L} d\mathbf{s} \\ &= q \int [\mathbf{E} + (\mathbf{v} \times \mathbf{B})] d\mathbf{s} \\ &= q \int \mathbf{E} d\mathbf{s} + q \int (\mathbf{v} \times \mathbf{B}) \mathbf{v} dt. \end{aligned} \tag{2.25}$$

In the last part of the equation the second integral is always equal to 0, if there are

no magnetic fields in longitudinal direction. By determining the electric field strength and the path of the particle through the field the change in energy can be calculated. To predict the path the change in momentum of the particle is needed. Introducing the relativistic velocity $\boldsymbol{\beta} = \mathbf{v}/c$ and the Lorentz-factor $\gamma = \sqrt{1-\beta^2}^{-1}$ and using the rest mass m one can write the relativistic momentum $\mathbf{p} = \gamma m \mathbf{v}$ and its derivative:

$$\frac{d\mathbf{p}}{dt} = m\gamma\frac{d\mathbf{v}}{dt} + m\mathbf{v}\frac{d\gamma}{dt}. \tag{2.26}$$

And substitute

$$\frac{d\gamma}{dt} = \frac{d\gamma}{d\beta}\frac{d\beta}{dt} = \gamma^3\frac{\beta}{c}\frac{dv}{dt}. \tag{2.27}$$

with equation 2.26, the equation of motion is:

$$\mathbf{F} = \frac{d\mathbf{p}}{dt} = m\Big(\gamma\frac{d\mathbf{v}}{dt} + \gamma^3\frac{\beta}{c}\frac{dv}{dt}\mathbf{v}\Big). \tag{2.28}$$

For forces parallel to the propagation of the particle the equation reduces to:

$$\frac{d\mathbf{p}_\parallel}{dt} = m\gamma^3\frac{d\mathbf{v}_\parallel}{dt}. \tag{2.29}$$

And for forces perpendicular to the propagation:

$$\frac{d\mathbf{p}_\perp}{dt} = m\gamma\frac{d\mathbf{v}_\perp}{dt}. \tag{2.30}$$

From the two equations 2.29 and 2.30 it is obvious how different the longitudinal and transverse dynamics are especially for ultra relativistic particles with $\gamma \gg 1$.

2.1.4 Electromagnetic Waves

Part of this work is focused on the analysis of the fields inside dielectric structures without any free charged particle interaction. So the next objective is looking at Maxwell's equations without sources:

$$\nabla\cdot\mathbf{D} = 0 \tag{2.31}$$

$$\nabla\cdot\mathbf{B} = 0 \tag{2.32}$$

$$\nabla\times\mathbf{E} + \frac{\partial}{\partial t}\mathbf{B} = \mathbf{0} \tag{2.33}$$

$$\nabla\times\mathbf{H} - \frac{\partial}{\partial t}\mathbf{D} = \mathbf{0} \tag{2.34}$$

To solve this homogenous differential equation system one ansatz is the plane wave:

$$\mathbf{E} = \mathbf{E_0} e^{j(\mathbf{k}\cdot\mathbf{r}-\omega t)} \tag{2.35}$$

$$\mathbf{B} = \mathbf{B_0} e^{j(\mathbf{k}\cdot\mathbf{r}-\omega t)} \tag{2.36}$$

Using equations 2.9 and 2.10 the Helmholtz wave equation follows:

$$(\nabla^2 + \epsilon_0\epsilon_r\mu_0\mu_r\omega^2)\begin{pmatrix}\mathbf{E}\\ \mathbf{B}\end{pmatrix} = \mathbf{0} \tag{2.37}$$

Substituting the plane wave ansatz into the wave equation yields the condition $|\mathbf{k}| = k = \omega\sqrt{\epsilon_0\epsilon_r\mu_0\mu_r}$. The phase velocity c_m and the refractive index n are given by:

$$c_m^2 = \frac{\omega^2}{k^2} = \frac{1}{\epsilon_0\epsilon_r\mu_0\mu_r} = \frac{c^2}{\epsilon_r\mu_r} \tag{2.38}$$

$$n = \frac{c}{c_m} = \pm\sqrt{\epsilon_r\mu_r} \tag{2.39}$$

Since this is a linear equation system any linear combination of these general fundamental solutions is a solution too. Using superpositions of the plane wave solution and constructing fitting boundary conditions is already a powerful tool in calculating fields for many different scenarios i.e. the fields in dielectric gratings. It can also be shown that without any transport of matter energy can be transported by electromagnetic waves propagating through vacuum. And thus power can radiate away from accelerated charged particles.

2.1.5 Energy Conservation

The energy conservation in a charged-particle/electromagnetic-field system can be expressed as :

$$\frac{d}{dt}\int u dV + \int \mathbf{JE} dV + \oint \mathbf{Sn} da = 0 \tag{2.40}$$

Where

$$u = \frac{1}{2}\epsilon_0(E^2 + c^2B^2), E = |\mathbf{E}|, B = |\mathbf{B}| \tag{2.41}$$

$$\mathbf{S} = \frac{1}{\mu_0}[\mathbf{E}\times\mathbf{B}] \tag{2.42}$$

The first part on the l.h.s in equation 2.40 stands for the energy taken out of the field or put into the field. The energy density u is dependent on the squares of the field

amplitudes E and B. The second part is the energy change of the particles inside the considered system and the third part is energy that is radiated out of the system or into the system. The Poynting vector $\mathbf{S}$ describes the energy transported through a unit surface element and the vector $\mathbf{n}$ is the normal vector on the plane defined by the cross product in equation 2.42. The surface defined for the third integral is the surface which is enclosing all charges and currents considered.

2.1.6 Hamiltonian Formalism

This section is based on United States Particle Accelerator School course material by Todd Satogata [52].

The forces involved have to be conservative to employ Hamiltonian dynamics to describe the system. The Lorentz force from equation 2.22 is not generally conservative since the term including the magnetic flux density $\mathbf{B}$ depends on velocity and thus on momentum. Here one can use the vector potential introduced above in equation 2.13. A so-called canonical momentum is defined

$$\mathbf{P} \equiv \mathbf{p} + q\mathbf{A} \tag{2.43}$$

resulting in a conservative canonical force:

$$\mathbf{F_{can}} \equiv \frac{d\mathbf{P}}{dt} \tag{2.44}$$

$$\nabla \times \mathbf{F_{can}} = 0. \tag{2.45}$$

The so-called Hamiltonian H represents the total energy of the considered system. It consists of the relations between positions and canonical momenta:

$$H(\mathbf{x}, \mathbf{P}; t) = E_{kin}(\mathbf{x}, \mathbf{P}) + E_{pot}(\mathbf{x}, \mathbf{P}; t) \tag{2.46}$$

with E_{kin} as the kinetic energy and E_{pot} as the potential energy. From the canonical pairs the equations of motion are given by Hamilton's equations:

$$\dot{\mathbf{x}} = \nabla_{\mathbf{P}} H \tag{2.47}$$

$$\dot{\mathbf{P}} = -\nabla H \tag{2.48}$$

The operator $\nabla_{\mathbf{P}}$ is noted with respect to the canonical momenta.

The Hamiltonian can be written from the total energy of a relativistic particle:

$$H = \sqrt{m^2c^4 + p^2c^2} \tag{2.49}$$

$$H = \sqrt{m^2c^4 + c^2[p_x^2 + p_y^2 + p_z^2]} \tag{2.50}$$

To employ Hamilton's equations one writes equation 2.50 in terms of the canonical momenta from equation 2.43:

$$H = c\sqrt{(P_x - qA_x)^2 + (P_y - qA_y)^2 + (P_z - qA_z)^2} + q\varphi. \tag{2.51}$$

Finally the time t is exchanged with the position s as the independent variable under the assumption that the particle moves in z-direction. This exchange leads to the expression of the longitudinal coordinates in time and energy, since the conjugate momentum to t is $-H$. The negative Hamiltonian is equivalent to the negative total Energy U. A Hamiltonian is retrieved with the following six coordinates and the path length s as independent variable:

$$H = -P_s(x, P_x, y, P_y, t, -U; s) \tag{2.52}$$

$$H = -qA_z - \sqrt{\left(\frac{U - q\varphi}{c}\right)^2 - m^2c^2 - (P_x - qA_x)^2 - (P_y - qA_y)^2} \tag{2.53}$$

One can introduce a few practical simplifications. Many elements of a particle accelerator only exhibit static transverse magnetic fields. This allows to choose scalar potential gauges such that $\varphi = 0$, $A_x = 0$ and $A_y = 0$. The transverse canonical momenta P_x and P_y will then be equal to the transverse particle momenta p_x and p_y. Equation 2.53 will also be normalized to the design momentum p_0:

$$\frac{H}{p_0} = -\frac{qA_z}{p_0} - \sqrt{\left(\frac{U}{p_0c}\right)^2 - \left(\frac{mc}{p_0}\right)^2 - \left(\frac{p_x}{p_0}\right)^2 - \left(\frac{p_y}{p_0}\right)^2} \tag{2.54}$$

The so-called paraxial approximation is valid if $p_x, p_y \ll p_0$, which means that the angle with the design trajectory in z-direction is small. Thus

$$\frac{p_x}{p_0} \approx \frac{dx}{ds} = x' \tag{2.55}$$

$$\frac{p_y}{p_0} \approx \frac{dy}{ds} = y' \tag{2.56}$$

Another canonical coordinate transform $(t, -U/p_0) \rightarrow (z \equiv s - v_0t, \delta \equiv (p - p_0)/p_0)$ leads to the standard canonical coordinates $H(x, x', y, y', z, \delta; s)$. The quantity z is the deviation from the design path length given by v_0t and δ is the relative momentum

deviation from the design momentum p_0.

$$H = -\frac{qA_z}{p_0} + \sqrt{1 + 2\delta + \delta^2 - x'^2 - y'^2} + 1 + \delta \tag{2.57}$$

In many applications the Hamiltonian above is limited to perturbative influences, thus just keeping lowest order terms.

$$H = -\frac{qA_z}{p_0} + \frac{1}{2}\left(x'^2 + y'^2\right) + \delta + ... \tag{2.58}$$

Briefly a few key properties are described. The phase space spanned by these coordinates is used to describe the state of a particle or particle distribution in the system. A particle beam consists of an ensemble of particles distributed in the phase space. Now a particle phase space density is defined in this space following an arbitrary function $f(x, y, z, x', y', \delta; s)$ that amounts to the number of particles $N(t)$ in the space:

$$N(t) = \int f(x, y, z, x', y', \delta; s) dx dy dz dx' dy' d\delta \tag{2.59}$$

Now the six-dimensional phase space current $\mathbf{J}_6$ should be continuous in any region:

$$\mathbf{J}_6 \equiv (f\dot{x}, f\dot{y}, f\dot{z}, f\dot{x'}, f\dot{y'}, f\dot{\delta}) = (f\mathbf{v}, f\mathbf{F}) \tag{2.60}$$

$$\frac{\partial f}{\partial t} + \nabla_6 \cdot \mathbf{J}_6 = 0 \tag{2.61}$$

Liouville's Theorem states that $\frac{df}{dt} = 0$. This essentially means that the phase space density acts like an incompressible fluid. It is assumed that all forces are conservative and only depend on position. When the phase space is chosen using canonical momenta it is valid in all frames w.r.t special relativity. Since no linearity of the potentials is assumed the theorem is valid also for space charge or intra-beam scattering.

Hamiltonian dynamics opens up the employment of another practical tool. Instead of deriving equations of motion from the Hamiltonian it is possible through Hamilton's equations to derive maps M from one location s_0 to another s_1. The six coordinates are described as a six dimensional phase space column vector $\mathbf{X}$.

$$H = H(x, x', y, y', z, \delta; s) \tag{2.62}$$

$$\mathbf{X} = (x, x', y, y', z, \delta)^T \tag{2.63}$$

The ^{T} notation stands for the transposition of a vector or matrix. Hamilton's equations 2.47 and 2.48 for this coordinate system with s as the time-like coordinate are:

$$\frac{dx_i}{ds} = \frac{\partial H}{\partial P_i} \tag{2.64}$$

$$\frac{dP_i}{ds} = -\frac{\partial H}{\partial x_i} \tag{2.65}$$

with the index i corresponding to the canonical pairs (x, x'), (y, y') and (z, δ). The notation from equation 2.63 renders Hamilton's equation as:

$$\frac{dX_i}{ds} = \sum_j S_{ij} \frac{\partial H}{\partial X_j} \tag{2.66}$$

where the matrix S is

$$S = \begin{pmatrix} 0 & 1 & 0 & 0 & 0 & 0 \\ -1 & 0 & 0 & 0 & 0 & 0 \\ 0 & 0 & 0 & 1 & 0 & 0 \\ 0 & 0 & -1 & 0 & 0 & 0 \\ 0 & 0 & 0 & 0 & 0 & 1 \\ 0 & 0 & 0 & 0 & -1 & 0 \end{pmatrix}. \tag{2.67}$$

The elements of M are defined by

$$M_{ij} \equiv \frac{\partial X_i(s_1)}{\partial X_j(s_0)}. \tag{2.68}$$

If the relation $M^T S M = S$ holds the map M is called symplectic. A symplectic map transforms the phase space coordinates in a way that is compatible with Hamiltonian dynamics and Liouville's theorem, thus conserving the phase space density as described in equation 2.61. Generally the maps can be non-linear and dependent on the coordinates. For the common beam transport elements like dipoles, quadrupoles, etc. particle transport maps can be derived using the Hamiltonian above (equation 2.57). Usually the equation is expanded in a limited order around some design momentum. If only the first order is used this leads to matrices and so-called linear transport.

Matrices for different beam line elements can be used to describe a sequence of magnetic elements and drifts, a so-called magnetic lattice. The matrices are multiplied and then applied to the initial coordinates and thus can be transformed into coordinates after the magnetic lattice. If a particle beam is transported from one place to another some kind of focusing is needed. Quadrupole magnets are used to implement charged particle beam transport. Practically, these are for a charged particle beam what lenses are for optical beams, with the drawback that they focus only in one plane and defocus in the other plane. The equations of motion for the transverse planes of the phase space for a constant quadrupole field are:

$$\frac{d^2x}{ds^2} + kx = 0 \tag{2.69}$$

$$\frac{d^2y}{ds^2} - ky = 0 \tag{2.70}$$

$$k \equiv \frac{\partial B_y}{\partial x}\frac{1}{p/q} \tag{2.71}$$

These equations describe an harmonic oscillator and by integration the matrices for the transverse planes can be derived, which is left to the literature at this point. The transport system will change the equations of motion above by making the spring constant dependent on the path length $k \to K(s)$. For a K of any periodicity this would be Hill's equation. This is a very suitable approach for a circular machine or an actually periodic structure like a so-called FODO (Focusing-drift-Defocusing-drift) lattice. This work is concerned with linear accelerators that are generally not periodic. But a non-periodic lattice can be seen as a part of a periodic lattice where the periodic boundary condition is replaced by initial conditions. The approach is still very valuable and can give insights on the beam transportation abilities and stability of a magnetic lattice. So a quasi-periodic ansatz for the equation 2.69 is:

$$x(s) = C_1 w(s)\cos\Phi(s) + C_2 w(s)\sin\Phi(s) \tag{2.72}$$

$$x'(s) = C_1\left(w'(s)\cos\Phi(s) - \frac{\sin\Phi(s)}{w(s)}\right) + C_2\left(w'(s)\sin\Phi(s) + \frac{\cos\Phi(s)}{w(s)}\right) \tag{2.73}$$

The quantity $\Phi(s)$ is the so-called betatron phase and $w(s)$ is the path length dependent amplitude scaling of the oscillation (or excursion, if non periodic) of a particle around the design orbit. Calculating the free parameters C_1 and C_2 in terms of the initial conditions (x_0, x_0') and (w_0, ϕ_0) gives:

$$C_1 = \left(w_0'\sin\phi_0 + \frac{\cos\phi_0}{w_0}\right)x_0 - (w_0\sin\phi_0)x_0' \tag{2.74}$$

$$C_2 = -\left(w_0'\cos\phi_0 - \frac{\sin\phi_0}{w_0}\right)x_0 + (w_0\cos\phi_0)x_0' \tag{2.75}$$

To get a consistent description with the solution found for a periodic lattice one rescales $w(s) = \sqrt{\beta(s)}$ and defines a betatron phase advance $\Delta\Phi \equiv \Phi(s) - \phi_0$. Writing this into a matrix form consistent with $X = (x, x')^T$ yields:

$$M(s) = \begin{pmatrix} \sqrt{\frac{\beta(s)}{\beta_0}}[\cos\Delta\Phi + \alpha_0 \sin\Delta\Phi] & \sqrt{\beta_0\beta(s)}\sin\Delta\Phi \\ -\frac{[\alpha(s)-\alpha_0]\cos\Delta\Phi+[1+\alpha_0\alpha(s)]\sin\Delta\Phi}{\sqrt{\beta_0\beta(s)}} & \sqrt{\frac{\beta_0}{\beta(s)}}[\cos\Delta\Phi - \alpha(s)\sin\Delta\Phi] \end{pmatrix} \tag{2.76}$$

where the Courant-Snyder parameters are:

$$\beta(s) \equiv w(s)^2 \tag{2.77}$$

$$\alpha(s) \equiv -\frac{1}{2}\beta'(s) \tag{2.78}$$

$$\gamma(s) \equiv \frac{1+\alpha(s)^2}{\beta(s)}, \tag{2.79}$$

which are all related via $K\beta = \gamma + \alpha'$. And

$$\Phi(s) = \int \frac{ds}{\beta(s)} \tag{2.80}$$

gives the phase advance. The Courant-Snyder parameters are describing the properties of the lattice independent of the initial parameters of the particles. With given initial Courant-Snyder parameters the down stream parameters at position s can be calculated from the transport matrix M. For an ensemble of particles these parameters can be connected with an ellipse in a plane of the phase space that is defined by characteristic quantities of the particle beam distribution. If one defines the ellipse using the RMS values (standard deviations) of the particle distribution one can define the RMS emittance ϵ.

$$\epsilon = \gamma(s)x(s)^2 + 2\alpha(s)x(s)x'(s) + \beta(s)x'(s)^2 \tag{2.81}$$

It can be shown that the area of an ellipse in phase space is conserved under linear transport and that even for non-normal distributions the RMS emittance ϵ is conserved [53]. Figure 2.1 visualizes the ellipse in phase space and gives an explanation on the connection of the parameters with the properties of the ensemble of particles at a certain point s.

If the design momentum p_0 of the particles changes, the axes for x' and y' change due to the scaling in equation 2.54. This means that ϵ will change. To recover an invariant of motion also for beam lines with changing design momentum like most accelerators exhibit, the emittance is normalized to the product of the Lorentz factor γ and the relativistic velocity β: $\epsilon_n \equiv \beta\gamma\epsilon$.

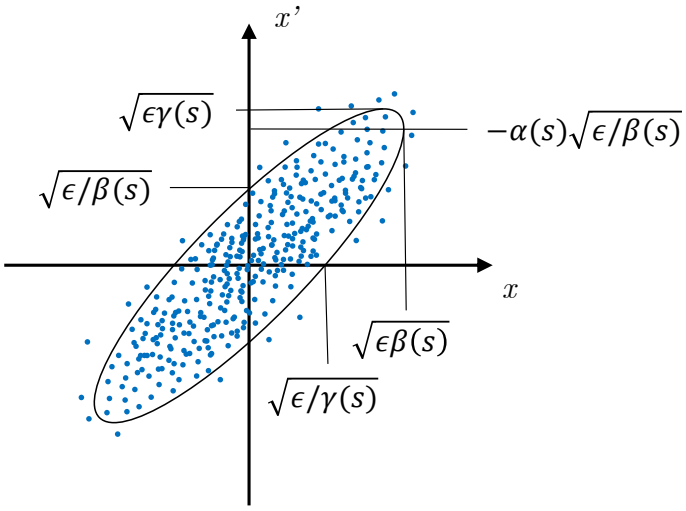

Figure 2.1: Shown is a snap shot of the transverse phase space at a certain position s. At the axes the relation between the characteristic points of the ellipse and the Courant-Snyder parameters are noted. The ellipse is chosen so that it connects the RMS values (standard deviation) of a particle distribution with the RMS emittance in the following relations: $\sigma_x = \sqrt{\epsilon\beta(s)}$ and $\sigma_{x'} = \sqrt{\epsilon\gamma(s)}$.

2.2 Laser-driven Acceleration Overview

One major distinguishing factor for DLAs is the propagation direction of the electromagnetic waves powering the devices. The driving laser either co-propagates with the particle beam or it is perpendicular to it. The devices applied in the two different regimes differ in their appearances and particle energy gain limiting factors.

In the co-propagating schemes the DLA forms a waveguide using various structures in which the electromagnetic power is coupled in. Usually a hollow core region is present in which the particle beam travels. The device can be a dielectric lined waveguide [25], a photonic band gap structure with a defect [54], surface modes of slab wave guides [55], optical fibers [56], etc. Figure 2.2 illustrates just a few of the possibilities to form such waveguides. The parameters of the device are designed so that the excited waveguide mode exhibits the desired shape and phase velocity.

The general advantage of co-propagating schemes is usually a higher efficiency compared to the perpendicular schemes due to a possible depletion of the laser pulse during the interaction with the particle beam. Limiting factors in achievable particle energy can be the coupling of the external laser source to the desired waveguide mode, the achievable phase velocity or group velocity or the losses in propagation of the accelerating mode. Often the coupling to the modes suitable for particle acceleration is a

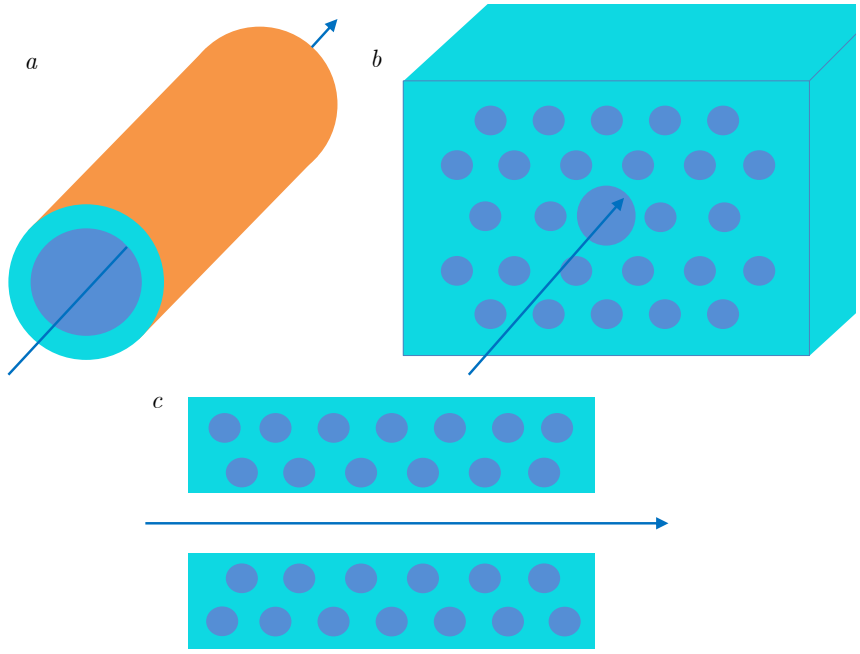

Figure 2.2: Different dielectric waveguide concepts are illustrated. The arrows indicate the propagation direction of the particles and the laser. Image *a* shows a dielectric lined metallic waveguide as used in [25]. Image *b* shows a transverse two-dimensional photonic bandgap structure with a defect in the middle. Suitable waveguide modes can be excited in the defect. This concept can also be implemented as a fiber [56]. Image *c* illustrates a longitudinal two-dimensional bandgap concept. A more sophisticated version was studied in [57].

significant design effort [58, 59, 57] that can lead to complex structures that are harder to manufacture. The group velocity combined with a finite pulse length can limit the interaction length in a single stage, thus limiting the achievable energy gain. The phase velocity can limit the interaction length due to slippage if it is not close enough to the velocity of the particles. Losses within the device usually limit the achievable average gradient of one stage.

The concept using a perpendicular drive laser employs periodic structures in the direction of the traveling particle beam and uses the evanescent fields close to these structures to accelerate or manipulate particle beams. One of the simpler designs is an optical phase grating as shown in figure 2.3. But the variety of designs is very broad [60, 61, 62]. The achievable energy gains in these structures are often limited by the available peak laser power and the inherent damage threshold of the grating materials. The diffracted fields above the grating can be described by a sum of spatial harmonics along the direction of the grating periodicity. The periodicity of the grating structures is matched to the

particle velocity so that the phase velocity of one of the spatial harmonics coincides with it. Then, to first order, the accelerating fields resemble those of standing wave RF-structures. A closer look into the field configuration is given in the following section 2.3.

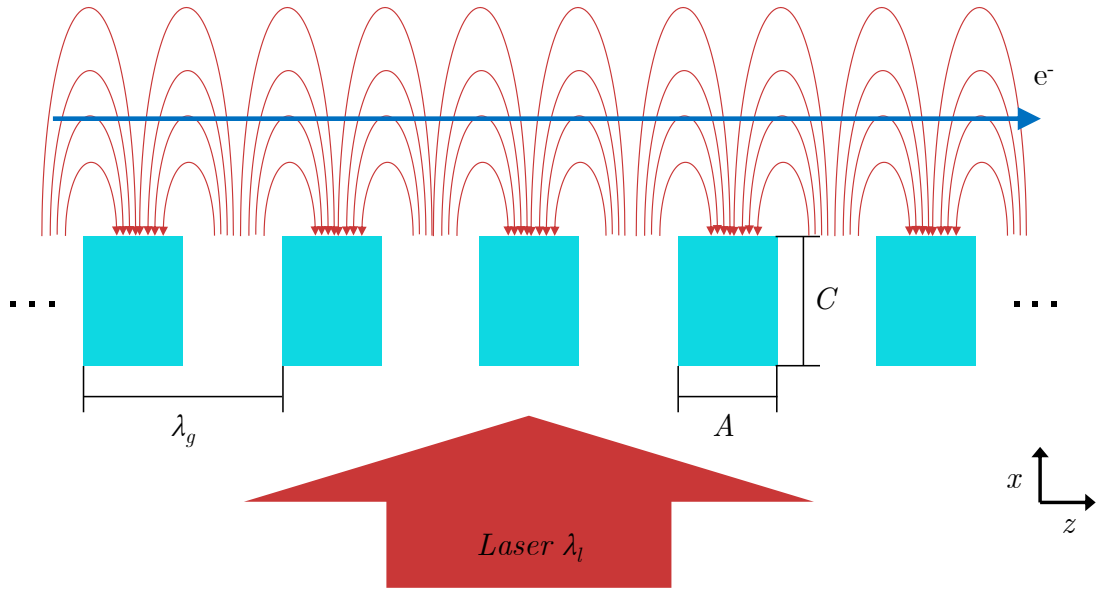

Figure 2.3: A single dielectric phase grating is illuminted by a laser. The period of the grating is λ_g. A represents the width of the grating teeth and C the height of the teeth or groove depth. The laser beam with the laser wavelength λ_l and frequency f is propagating in x-direction. The red arrows illustrate the first spatial harmonic of the diffraction fields excited on the grating. The actual field distribution would be the sum of all the spatial harmonics along the grating periodicity.

The power delivery to the perpendicularly driven devices is either in free space or using waveguides. Handling free space laser propagation and manipulation for the laser wavelengths of interest is a well researched field and is readily available for proof-of-principle experiments. For an integrated device an on-chip power delivery via waveguides and coupling of an external laser via fibers is investigated within the ACHIP collaboration [63, 64].

In this work we explore the dielectric phase gratings and their potential for particle

beam acceleration, manipulation and characterization.

2.3 Dielectric Gratings as Electron Accelerators

2.3.1 Electro-magnetic Fields in Dielectric Gratings

This section is partially based on a conference contribution by R. Joel England [65].

The compact theoretical description of the electromagnetic fields excited in dielectric gratings strongly draws from a number of assumptions. At first we assume periodicity along the z-axis in which also the particle beam travels. This assumption is usually valid due to the small grating period (µm) compared to the total length of the device (mm). Together with that we assume that fringe fields at the edges of the device in the z-direction have no significant influence on the particles. This assumption is reasonable since the approximately Gaussian laser beams used to illuminate the structures have smaller beam diameters than the dimensions of the device. The laser beam diameter is assumed to be the 4σ distance for a normal intensity distribution. Thus, the field amplitudes at the edges are small compared to the ones in the middle of the structure.

Another assumption is that the grating grooves in the direction of the y-axis are much longer than the periodicity of the grating, basically reducing the derivation of the electromagnetic fields to a two dimensional problem in the z-x-plane. This assumption is usually met by the structures used for relativistic particles by deliberately designing them that way and by considering particle beam sizes smaller than the laser spot size in the y-direction. Figure 2.4 visualizes the assumptions. Figure 2.3 corresponds to the top view of the same device so that both illustrate the used coordinate system.

This type of dielectric grating is used as a dispersive element in optical setups [66]. In this application the periodicity of the grating close to the wavelength of the incoming light leads to diffraction patterns in the far-field. The angle of the diffraction orders is dependent on the wavelength, thus enabling the application as dispersive optical element. The corresponding diffraction effect in the near-field is the so-called Talbot-effect [67] producing fractal images of the grating if the grating period is larger than the incident light wavelength. If the grating period becomes shorter than the wavelength (around two times) the diffraction effect vanishes and the grating interacts with the light as an effective material [68]. In the intermediate regime a mixture of both effects can be observed.

As an electron acceleration device we are interested in a grating periodicity close to the incident laser wavelength and to the fields close to the grating surface to circumvent the Lawson-Woodward Theorem [69]. It states that a linear acceleration of charged particles by a laser pulse in free space is not possible. We will describe the near-field of the grating as an infinite sum of surface wave spatial harmonics from a Fourier series along the z-direction, which all have the same time periodicity of the incoming laser field.

Due to our assumptions we can reduce the derivation to a two-dimensional problem in the x-z-plane. The starting grounds are the source free Maxwell's equations from section

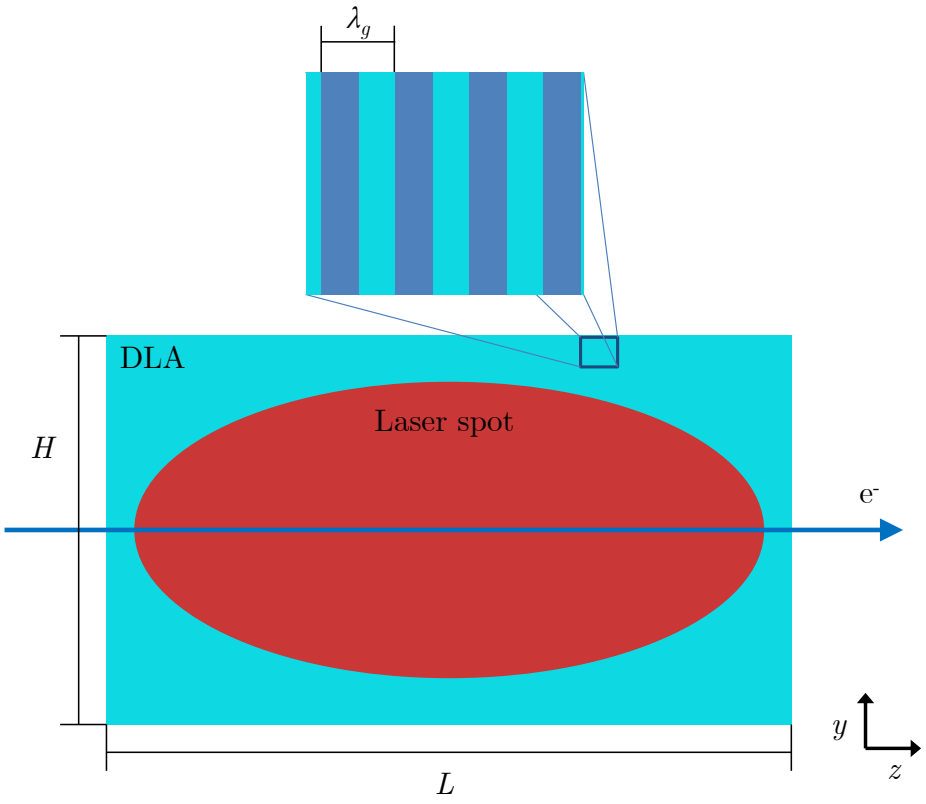

Figure 2.4: The schematic shows the baseline assumptions for the derivation of the electromagnetic fields of the laser illuminated dielectric gratings. The blue arrow represents the electron beam e^-. Its transverse beam size in the y-direction is significantly smaller than the laser beam diameter in that direction. The laser beam propagates perpendicular in the x-direction onto the grating. The length L and the height H of the DLA device are significantly larger than the period of the grating λ_g. The length L is also larger than the laser beam diameter in the z-direction.

2.1.4 and the Helmholtz wave equation 2.37. We are noting the assumed harmonic time dependence as $\omega = 2\pi f$ and f as the frequency defined by the laser wavelength λ_l, which results in:

$$\nabla \cdot \mathbf{D} = 0 \tag{2.82}$$

$$\nabla \cdot \mathbf{B} = 0 \tag{2.83}$$

$$\nabla \times \mathbf{E} = i\frac{\omega}{c^2}\mathbf{B} \tag{2.84}$$

$$\nabla \times \mathbf{H} = -i\frac{\omega}{c^2}\mathbf{D}. \tag{2.85}$$

The quantity i stands for the imaginary unit. The actual values of the field components in x,y,z and t are then given by the real parts of the complex components noted here.

We will look at the excitation of a dielectric grating structure ($\mu = 1$) with a free space wave as described in equations 2.35 and 2.36. We split the derivation into the two polarization directions by noting equation 2.37 w.r.t. the p-polarization and the s-polarization. P-polarization means the electric field is oriented in the x-z-plane, whereas the s-polarization has the electric field pointed in the y-direction as depicted in figure 2.5.

Noting the electric field components of equation 2.37 for the s-polarization and calculating the magnetic flux density via equation 2.3 gives:

$$\frac{\partial^2 E_y}{\partial x^2} + \frac{\partial^2 E_y}{\partial z^2} = -\left(\frac{\omega}{c}\right)^2 D_y \tag{2.86}$$

$$i\frac{\omega}{c}\mathbf{B} = \nabla \times \mathbf{E} = \frac{\partial E_y}{\partial z}\hat{\mathbf{x}} - \frac{\partial E_y}{\partial x}\hat{\mathbf{z}} \tag{2.87}$$

And the two components for the p-polarization give:

$$\frac{\partial^2 E_x}{\partial z^2} - \frac{\partial^2 E_z}{\partial x \partial z} = -\left(\frac{\omega}{c}\right)^2 D_x \tag{2.88}$$

$$\frac{\partial^2 E_z}{\partial x^2} - \frac{\partial^2 E_x}{\partial x \partial z} = -\left(\frac{\omega}{c}\right)^2 D_z \tag{2.89}$$

$$i\frac{\omega}{c}\mathbf{B} = \nabla \times \mathbf{E} = \left[\frac{\partial E_z}{\partial x} - \frac{\partial E_x}{\partial z}\right]\hat{\mathbf{y}} \tag{2.90}$$

The displacement current $\mathbf{D} = \epsilon(x, z)\mathbf{E}$ is dependent on the dielectric function ϵ which is a scalar for an isotropic material. We can write ϵ piecewise in x:

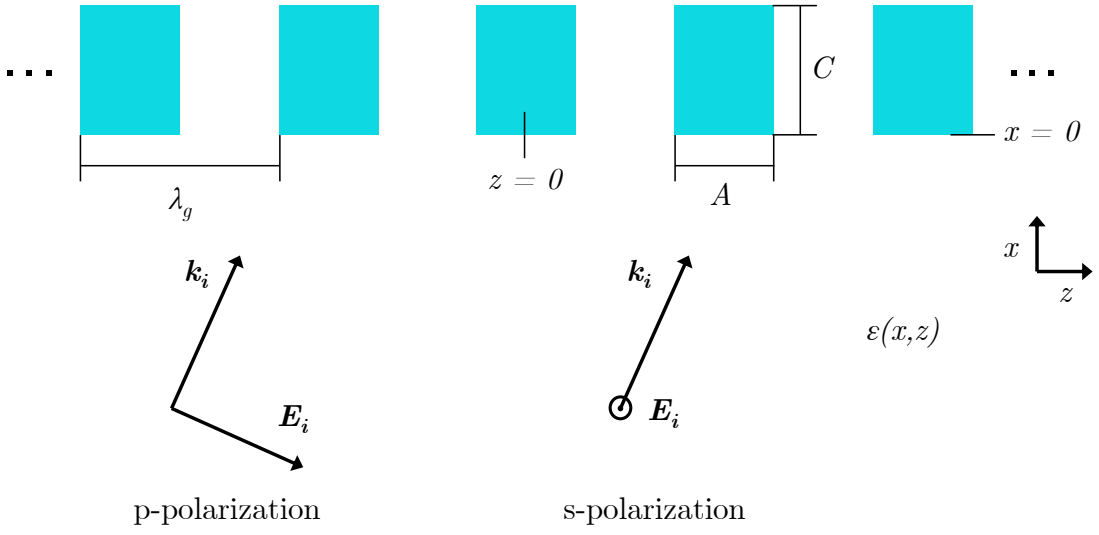

Figure 2.5: For the p-polarization the electric field lies in the x-z-plane. In the s-polarization configuration it is oriented in the y-direction. For an isotropic dielectric material ϵ is a scalar dependent on the (x, z)-position and uniform in the y-direction.

$$\epsilon(x,z) = \begin{cases} \epsilon_0\epsilon_r & ; x < 0 \\ F(z)(\epsilon_0\epsilon_r - 1) + 1 & ; 0 \leq x \leq C \\ \epsilon_0 & ; x > C \end{cases} \tag{2.91}$$

$$F(z) \equiv \sum_l H(z - l\lambda_g + A/2)H(l\lambda_g + A/2 - z); l = (0, \pm 1, \pm 2, ...) \tag{2.92}$$

with H being the Heaviside step function. These periodic steps will translate into the electric field via equation 2.4 and into the magnetic field via equation 2.9. The periodicity of the dielectric function in z can be used as a Floquet condition [70] with the unit vector $\mathbf{u} = \lambda_g\hat{\mathbf{z}}$ and the position vector $\mathbf{r}$ to construct periodic solutions of the form:

$$\begin{gathered}\mathbf{E}(\mathbf{r}+\mathbf{u})=\mathbf{E}(\mathbf{r})e^{i\Psi};\mathbf{B}(\mathbf{r}+\mathbf{u})=\mathbf{B}(\mathbf{r})e^{i\Psi};\\ k_z\lambda_g=\Psi.\end{gathered} \tag{2.93}$$

With an incident plane wave excitation with $\hat{\mathbf{n}}$ as the normal vector in propagation direction

$$\mathbf{E}_i=\mathbf{E}_{i,0}e^{i\mathbf{k}_i\cdot\mathbf{r}-i\omega t};\mathbf{k}_i=\frac{\omega}{c}\sqrt{\mu_i\epsilon_i}\hat{\mathbf{n}} \tag{2.94}$$

the exemplary solution comprised of the Floquet spatial harmonics yields:

$$\mathbf{E}(\mathbf{r})=\mathbf{E}(\mathbf{r}_\perp)e^{-i\omega t}\sum_{n=-\infty}^{\infty}a_n e^{ik_n z}. \tag{2.95}$$

The corresponding harmonic wave numbers are $k_n=k_0+nk_g$ with $k_0=\Psi/\lambda_g$ and $k_g=2\pi/\lambda_g$. Since $\Psi=\mathbf{k}\cdot\mathbf{u}=\lambda_g\frac{\omega}{c}\sqrt{\mu_i\epsilon_i}\hat{\mathbf{n}}\cdot\hat{\mathbf{z}}$ the fundamental from the projection onto the grating periodicity in z gives $k_0=\frac{\omega}{c}\sqrt{\mu_i\epsilon_i}\cos\theta$ with θ as the incident angle of the plane wave with respect to the z-direction.

To interact with a charged particle at relativistic velocity β_p close to the grating surface the phase velocity of a spatial harmonic has to match the velocity, otherwise the exerted forces on the charged particle will average out to first order. The phase velocity β_n of the n-th spatial harmonic is:

$$\beta_n=\frac{\omega}{ck_n}=\frac{\omega/c}{k_0+nk_g}. \tag{2.96}$$

For normal incidence of the excitation to the grating plane ($\theta=\pi/2$) the synchronicity condition is:

$$\lambda_g=\beta n\lambda_l. \tag{2.97}$$

With the dielectric function from equation 2.91 and a solution in the form of a sum of the spatial harmonics like equation 2.95 the s-polarization electric field solution in the vacuum region ($x>C$ in figure 2.5) next to the grating is (also refer to [71])

$$E_y(x,z)=E_0\sum_n a_n^s e^{-i\Lambda_n x}e^{ik_n z} \tag{2.98}$$

and for the p-polarization

$$E_x(x,z) = -E_0 \sum_n \frac{k_n}{\Lambda_n} a_n^p e^{-i\Lambda_n x} e^{ik_n z} \tag{2.99}$$

$$E_z(x,z) = E_0 \sum_n a_n^p e^{-i\Lambda_n x} e^{ik_n z} \tag{2.100}$$

with $\Lambda_n = \sqrt{(\omega/c)^2 - k_n^2}$. From the relation for Λ_n one can see that for k_g larger or equal to the wavenumber of the normally incident laser (ω/c) the term k_n^2 will always be larger than $(\omega/c)^2$ with the exception of the zero order which is the transmitted fraction. This means that all spatial harmonics are evanescent fields with an exponential decay away from the grating, decaying faster with growing x the higher the spatial order is. Since our synchronous charged particle will not be faster than the speed of light a matching grating will have a larger or equal wavenumber than the incident laser wavelength (compare equation 2.97).

The coefficients $a_n^{s,p}$ can be calculated using the method described in [71] or can be obtained via a numerical electromagnetic field solver.

Any rotation of the polarization direction can be described using a superposition of the two polarizations. An additional grating can be added and a superposition gives the non-zero solutions for a single-sided illumination of a double grating in the vacuum region ($C < x < C + G$ and $\mathbf{E}_i' = \mathbf{0}$ in figure 2.6) between the gratings:

$$\begin{aligned} E_y &= E_0 \sum_n [a_n^s e^{i\Lambda_n x} + b_n^s e^{-i\Lambda_n x}] e^{ik_n z} \\ B_x &= \frac{c^2}{\omega} E_0 \sum_n k_n [a_n^s e^{i\Lambda_n x} + b_n^s e^{-i\Lambda_n x}] e^{ik_n z} \\ B_z &= -\frac{c^2}{\omega} E_0 \sum_n \Lambda_n [a_n^s e^{i\Lambda_n x} - b_n^s e^{-i\Lambda_n x}] e^{ik_n z} \end{aligned} \tag{2.101}$$

and for the p-polarization

$$E_x = -E_0 \sum_n \frac{k_n}{\Lambda_n} [a_n^p e^{i\Lambda_n x} - b_n^p e^{-i\Lambda_n x}] e^{ik_n z} \tag{2.102}$$

$$E_z = E_0 \sum_n [a_n^p e^{i\Lambda_n x} + b_n^p e^{-i\Lambda_n x}] e^{ik_n z} \tag{2.103}$$

$$B_y = \frac{\omega}{c^2} E_0 \sum_n \frac{1}{\Lambda_n} [a_n^p e^{i\Lambda_n x} - b_n^p e^{-i\Lambda_n x}] e^{ik_n z}. \tag{2.104}$$

The p-polarization configuration with normal excitation incidence on the grating plane will be used for DLA designs in chapter 3 and to develop a single electron bunch net

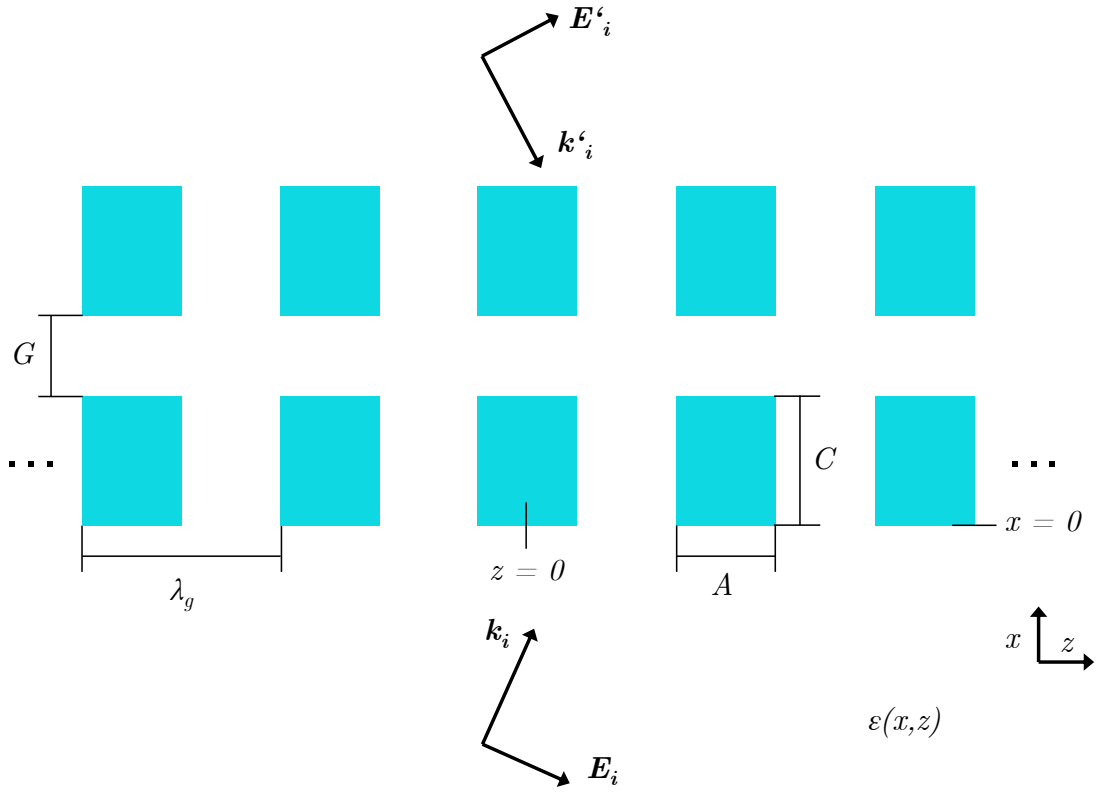

Figure 2.6: The schematic of a double grating with exemplary p-polarization. This is the configuration used as a charged particle accelerator. The structure can be illuminated from both sides, to produce symmetric fields. For high matched relativistic velocities β_p even the single sided illumination (where $\mathbf{E}_i' = \mathbf{0}$) yields almost uniform accelerating fields across the gap G. The two configurations presented for the incident plane waves E_i and E_i' are in phase or π out of phase.

energy gain experiment in chapter 5.

Also important are the dual-sided illumination configurations. The solutions for two other discrete configurations are given in the following, where a phase difference between $\mathbf{E}_i$ and $\mathbf{E}_i'$ in figure 2.6 is assumed to be either zero or π. The upper line in the equations gives the in-phase case the lower line the π out-of-phase case. The solutions for s-polarization in the vacuum region ($C < x < C + G$ in figure 2.6) are:

$$
\begin{aligned}
E_y &= E_0 \sum_n (a_n^s \pm b_n^s) \begin{Bmatrix} \cosh(i\Lambda_n x) \\ \sinh(i\Lambda_n x) \end{Bmatrix} e^{ik_n z} \\
B_x &= \frac{c^2}{\omega} E_0 \sum_n k_n (a_n^s \pm b_n^s) \begin{Bmatrix} \cosh(i\Lambda_n x) \\ \sinh(i\Lambda_n x) \end{Bmatrix} e^{ik_n z} \\
B_z &= -\frac{c^2}{\omega} E_0 \sum_n \Lambda_n (a_n^s \pm b_n^s) \begin{Bmatrix} \sinh(i\Lambda_n x) \\ \cosh(i\Lambda_n x) \end{Bmatrix} e^{ik_n z}
\end{aligned}
\tag{2.105}
$$

and for the p-polarization they are:

$$
\begin{aligned}
E_x &= -E_0 \sum_n \frac{k_n}{\Lambda_n} (a_n^p \pm b_n^p) \begin{Bmatrix} \sinh(i\Lambda_n x) \\ \cosh(i\Lambda_n x) \end{Bmatrix} e^{ik_n z} \\
E_z &= E_0 \sum_n (a_n^p \pm b_n^p) \begin{Bmatrix} \cosh(i\Lambda_n x) \\ \sinh(i\Lambda_n x) \end{Bmatrix} e^{ik_n z} \\
B_y &= \frac{\omega}{c^2} E_0 \sum_n \frac{1}{\Lambda_n} (a_n^p \pm b_n^p) \begin{Bmatrix} \sinh(i\Lambda_n x) \\ \cosh(i\Lambda_n x) \end{Bmatrix} e^{ik_n z}.
\end{aligned}
\tag{2.106}
$$

Important to notice is that the p-polarization configuration with $\mathbf{E}_i$ and $\mathbf{E}_i'$ in phase is the ideal candidate for an accelerator structure, since the accelerating fields are symmetric in x around the gap center and are virtually uniform for $G \ll \Lambda_n$. It is used in most of the investigations in chapter 3. Another notable configuration is the p-polarization with the drive lasers π out of phase. It is investigated w.r.t. charged particle beam deflection in chapter 4.

2.3.2 Particle Dynamics in Grating-type DLA

We will take a look at the accelerating p-polarization configuration with a double-sided in-phase illumination from equations 2.106. For the gap size $G \ll \Lambda_n$ and in the middle of the gap the cosh-term can be dropped and the sinh-terms become linear in x. The coefficients a_n^p and b_n^p can be added to give a_n. Also the time dependence of E_0 is pulled out explicitly and an initial phase offset ϕ_0 is introduced:

$$E_x = -E_0 e^{-i(\omega t+\phi_0)} \sum_n \frac{k_n}{\Lambda_n} a_n x e^{ik_n z} \tag{2.107}$$

$$E_z = E_0 e^{-i(\omega t+\phi_0)} \sum_n a_n e^{ik_n z} \tag{2.108}$$

$$B_y = \frac{\omega}{c^2} E_0 e^{-i(\omega t+\phi_0)} \sum_n \frac{1}{\Lambda_n} a_n x e^{ik_n z} \tag{2.109}$$

Now the fields at the position of a charged particle moving with relativistic velocity β_p at the center of the gap can be retrieved by introducing $z = c\beta_p t$ and using the relation from equation 2.96. E_z can be written as:

$$E_z(t) = E_0 \sum_n a_n e^{i((\beta_p/\beta_n - 1)\omega t+\phi_0)} \tag{2.110}$$

At first we have a look at the longitudinal dynamics. Taking the real part and moving the zero phase and zero z-position to where the field changes sign and writing this out explicitly for the fundamental and first order spatial harmonic yields:

$$\begin{aligned} E_z(t) = E_0[a_0 \sin(\omega t + \phi_0) + a_1 \sin((\beta_p/\beta_1 - 1)\omega t + \phi_0) + \\ + a_{-1} \sin((\beta_p/\beta_{-1} - 1)\omega t + \phi_0)] \end{aligned} \tag{2.111}$$

Since $z = 0$ was chosen to make the periodicity symmetric $a_1 = a_{-1}$ and for normal excitation incidence $\beta_{-1} = -\beta_1$ (see equation 2.96). The fundamental term does not depend on the velocity of the particle since there is no longitudinal periodicity. We can write the Lorentz factor from the field above describing the gained energy of the particle in relation to the particle rest mass:

$$\begin{aligned} \frac{d\gamma}{dt} = \frac{eE_0}{2m_e c^2}[a_0 \sin(\omega t + \phi_0) + \\ + a_1(\sin((\beta_p/\beta_1 - 1)\omega t + \phi_0) + \sin(-(\beta_p/\beta_1 + 1)\omega t + \phi_0))] \end{aligned} \tag{2.112}$$

The form of the equation for the first spatial harmonic is similar to the result for a standing wave RF-cavity as found e.g. in [20]. β_p is dependent on γ and thus on time t. It is common to define:

$$\alpha = \frac{eE_0}{2m_e c^2 k} \tag{2.113}$$

with k being the wavenumber of the accelerating field.

The dimensionless quantity α can be understood as how fast a particle gets relativistic

w.r.t the wavelength of the driving field. If $\alpha \geq 1$ the particle reaches relativistic speed within one wavelength. The conventional RF-guns have a typical α of $1.5 - 2.0$. The laser accelerators discussed in this work exhibit large accelerating fields in the GV/m regime but also have very small wavelengths in the µm regime, so typical α will be around 10^{-4}. This has critical effects on the dynamics of the particles in the fields. In order to accelerate a charged particle from rest in a field matched to the velocity of light α has to be significantly larger. From equation 2.112 it is apparent that if the relativistic particle velocity β_p is not close to the phase velocity of the first spatial harmonic the equation keeps oscillating, thus showing no average energy gain. This is also true for higher spatial harmonics.

For low energy particles (low γ) the phase velocity of an interacting spatial harmonic has to be matched to a design acceleration gradient and consequently to a design β_p. This can be achieved by chirping the grating in longitudinal direction thus increasing the phase velocity of the interacting spatial harmonic. Even at relatively high γ the phase slippage plays an important role for extended interaction lengths as will be discussed in chapter 3.

The transverse dynamics for this configuration can be described by inserting equations 2.107 and 2.109 into the Lorentz force from equation 2.22 yielding:

$$F_\perp = -eE_0 e^{-i\omega t}\hat{\mathbf{x}} \sum_n (1 - \beta_p \beta_n) \frac{k_n}{\Lambda_n} a_n x e^{ik_n z} \tag{2.114}$$

For this configuration only focusing/defocusing forces in x-direction are present. It can be seen that transverse forces from a speed-of-light spatial harmonic vanish if the particle approaches speed of light. A ponderomotive RF focusing effect is expected from the form of equation 2.114 comparable to a standing wave RF cavity [72] and usually apparent higher order spatial harmonic content.

2.4 Limitations of Materials for Dielectric Structure-based Laser Acceleration

The main limiting factor for the accelerating fields in dielectric structures is laser induced damage. For the discussion of laser damage to a material it is practical to define a measure of exposure independent of spot size and pulse length. The fluence F is widely used in the literature. It is defined as energy per area.

Generally, one wants to run a particle accelerator device without the occurrence of damage. Material damage from short laser pulses might be linked to impurities and defects in the material under investigation. For practicality, application of the appropriate statistical methods and ease of comparison of data from different experiments the damage threshold fluence F_{th} is defined. It is equal to the fluence at which 50 % of the irradiated samples exhibit damage.

The acceleration gradient G in a DLA is proportional to the square root of the damage fluence F_{th} and inversely proportional to the pulse length τ_L.

$$G \propto \frac{\sqrt{F_{th}}}{\tau_L} \tag{2.115}$$

DLAs are candidates for high acceleration gradients due to their high damage thresholds at optical and near-infrared frequencies compared to metallic structures [73]. The dominant damage mechanisms are dependent on the pulse length and the wavelength irradiated on the dielectric material. Only short laser pulses below 100 ps are discussed in this section, since these enable high acceleration gradients.

Table 2.1: Listed are the different damage regimes for short-pulse laser damage dependent on the laser pulse length τ_L.

Pulse Length τ_L	**Damage Type**	**Mechanism**
$> 50\,\text{ps}$	Diffusion-dominated	Heating of conduction-band electrons, transfer to lattice melting, boiling, fracturing
$50\,\text{ps} < \tau_L > 10\,\text{ps}$	transition regime	Keldysch formalism
$< 10\,\text{ps}$	Ablation-dominated	(multi-)photon ionization, collisional ionization, plasma formation

Three different regimes are observed: Pulses with lengths above 50 ps mainly induce melting, boiling and fracturing due to expansion. Conduction-band electrons are heated and transfer their energy to the lattice structure of the material. Pulses with lengths below 10 ps mainly exhibit ablation damage with low penetration depth. The mechanisms are photon and multi-photon ionization and subsequent collisional ionization. When a critical free carrier density is reached a plasma is formed. The generated plasma is highly absorbent. In this regime the occurrence of damage is very sensitive to defects in the material which may enhance the free carrier production. In between 50 ps and 10 ps there is a mixed regime which is described using the Keldysch parameter[74]. In this regime a transition between the different dominant damage mechanisms is observed. The regimes are listed in table 2.1 [75]. For even shorter pulses in the fs regime the multi-photon ionization becomes the dominant effect and the initial number of free carries is less important. This means defects and impurities in the material also become less important. Damage starts to occur dependent on the material at intensities of $10^9\,\text{W/cm}^2$ [76].

Small changes in wavelength can have a big influence on the damage threshold fluence in the short pulse regime, due to the non-linear nature of the multi photon processes and the interaction with the created plasma. When the plasma densities n_e created via the different ionization processes exhibit a plasma frequency ω_p close to the frequency of the laser radiation the energy absorption is especially efficient reducing the damage threshold fluence. The plasma density is dependent on the ionization rate, which can be modeled using the Keldysch parameter. The figure 2.7 taken from [73] shows the measured damage threshold fluence together with a model based on multi-photon ionization rate and the subsequent power absorption dependent on the plasma frequency with the

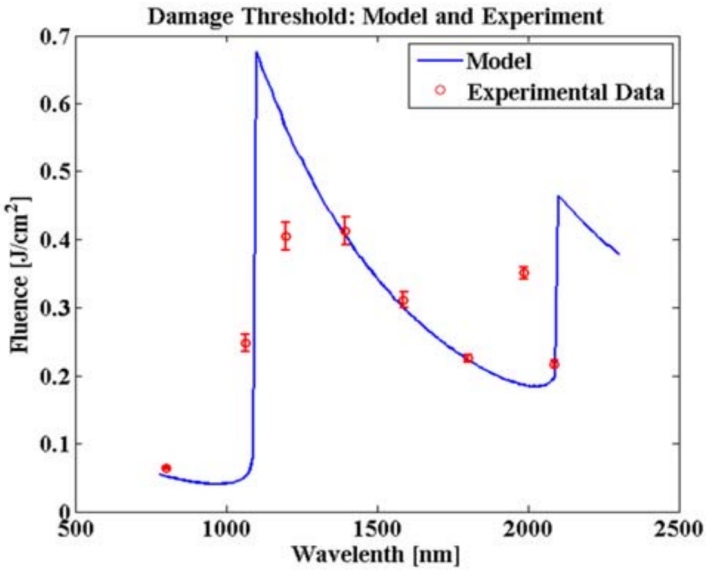

Figure 2.7: Dependence of the damage fluence vs. incident laser wavelength for silicon illuminated by pico-second laser pulses from an optical parametric amplifier. A strong non-linear dependence is apparent. The model depicted in the solid line is derived from the ionization rate via the Keldysch-theory. The minimal damage threshold appears at 1000 nm where the plasma created by ionization has the same plasma frequency as the incoming laser field. Figure taken from [73] by K. Soong.

effective electron mass m^*.

$$\omega_p = \sqrt{\frac{4\pi n_e e^2}{m^*}} \tag{2.116}$$

In [75] another model for the dependence of the damage fluence on the laser pulse length τ_L was developed. For the regime below 1000 ps it shows very good agreement with measurements. It is based on a kinetic equation and a subsequently derived rate equation, which takes into account all the above mentioned processes. Numerical simulations using the kinetic equation yield very good agreement with the analytic rate equation. The critical free carrier density is set to be just below the threshold where the plasma would be totally reflecting and thus is most absorbing. The figure 2.8 taken from [75] shows the damage threshold fluence for fused silica from the model together with measurement data. The graph for multi-photon ionization only is also shown.

The equations must be modified to the material used by setting the band-gap energy and phonon scattering rates into the material lattice. The wavelength of the laser pulse has to be incorporated using the solid atom density and the photo ionization cross sections for the dominant orders depending on the band gap. Higher-order cross sections can

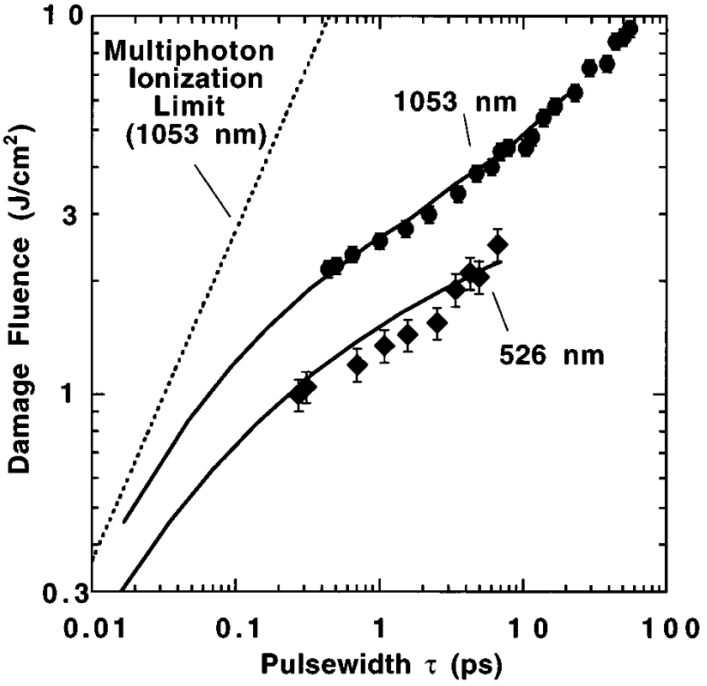

Figure 2.8: Dependence of the damage fluence on pulse width for two different wavelengths on fused silica. For shorter pulse lengths i.e. higher intensities the damage threshold approaches the line where the critical plasma density is reached by multi-photon ionization only. The solid line shows the model the dots and diamonds the experimental data. Figure taken from [75] by B. C. Stuart.

be estimated using the Keldysch formalism. Tunneling becomes important for very high intensities. For a detailed description refer to [75]. Unfortunately the phonon scattering rates and critical plasma densities are only known for a limited number of materials making experimental determination necessary. Also the influence of the microstructure geometry on the damage threshold fluence is still under investigation.

Different materials will exhibit different damage threshold fluence depending on the wavelength. A selection of different materials is shown in figure 2.9 taken from [73].

In the experimental part in chapter 6 of this work short laser pulses (3 ps) were used to induce damage in silicon. The wavelength used will be 2050 nm from the hybrid Ho:YLF amplifier described in chapter 1.

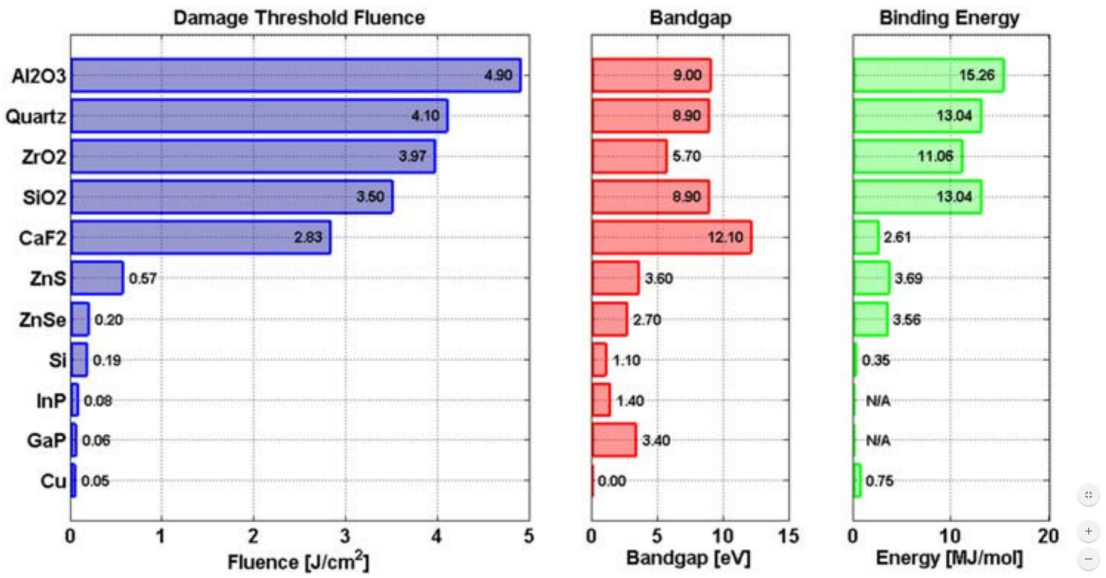

Figure 2.9: Damage threshold fluence, bandgap and binding energy of different materials for a 1 ps laser pulse at 800 nm wavelength and at a repitition rate of 600 Hz by a Ti:Sapphire laser. Sapphire (Al_2O_3) would be the material showing the highest threshold fluence, but is generally one of the materials less suitable for micro manufacturing. Figure taken from [73] by K. Soong.

3 Numerical Simulation of Particle Dynamics in Dielectric Gratings

In this chapter the properties of the gratings w.r.t. to spatial harmonic content and particle dynamics in the gap region are investigated. From geometry parameter studies grating designs were chosen for manufacturing by the Solgaard group at Stanford University and the Laser Physics group at FAU Erlangen, which are foreseen to be tested at the ARES linac. For the design and simulations working points were chosen to fit the predicted performance of ARES. The particle dynamics studies were used to develop a method for efficient simulation of extended interaction lengths for DLAs. Without large computation resources a full particle-in-cell (PIC) simulation is only possible for interaction lengths in the order of several wavelengths. Due to the large computation resources needed the simulation of hundreds of drive laser wavelengths requires large scale high-performance computation clusters [77]. Interaction lengths longer than hundreds of drive laser periods are usually prohibitively computation resource demanding, thus a fast tracking code was developed. In the first section designs for DLAs and their coupling behavior are presented. The second section presents a simulation method based on per-period DLA interaction. A PIC simulation covering a limited interaction length is compared to the per-cell method developed. An example of a GeV-DLA with a meter-long interaction length is presented to showcase the capabilities of the per-cell simulation method.

3.1 Design of Dielectric Gratings for Relativistic Electron Acceleration

For the simulation of the gratings the assumptions of chapter 2 were used. The frequency solver of CST MWS [78] was used to perform parameter scans on different grating designs. The simulation domain was reduced to a single period and bound by magnetic and electric boundaries respectively to enforce the correct polarization behavior. The relevant geometry parameters scanned are shown schematically in figure 3.1.

With the available laser system of 2050 nm wavelength the matched phase velocity of the first spatial harmonic was chosen to be at the speed of light. Thus the periodicity of the grating λ_g from the synchronicity condition in equation 2.97 is equal to the laser wavelength λ_l. Via an incidence angle θ of the drive laser the phase velocity of the first spatial harmonic can be reduced. For relativistic electrons with a velocity close to the speed of light the incidence angle θ is very close to 90°.

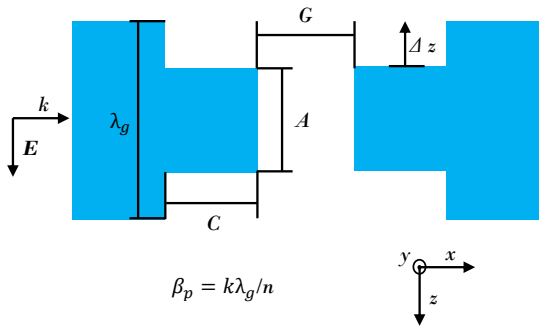

Figure 3.1: A single period of the dielectric grating. The structure is assumed to be uniform in the y-direction and periodic in z-direction. Parameters A and C are the width and height of the grating teeth. λ_g is the period of the grating and Δz the offset of the opposing teeth, if the two opposing gratings are moved against each other in z-direction. The laser field incident in x-direction has an electric field $\boldsymbol{E}$ polarized in z-direction with the wavenumber k. β_p is the relativistic speed of a particle that is matched to the phase velocity of the n-th spatial harmonic in the gap region in accordance with equation 2.97.

Materials with high expected damage thresholds are more suitable, see figure 2.9. If the structure design exhibits a substrate that needs to be passed by the laser, a lower refractive index is preferable, due to the fresnel reflection at the incident facet. Silicon and fused silica are the materials with the most advanced manufacturing capabilities available. These are the two materials chosen. In accordance with manufacturing capabilities rather simple grating designs were used. For fused silica a rectangular shape was chosen. For Silicon elliptic pillars standing free on a substrate were chosen. In this design the substrate is not passed by the drive laser but is only suitable for free-space coupling. The manufacturing processes are discussed in chapter 5.

Figure 3.2 shows the mean value of the magnitude of the first three spatial harmonics and the fundamental harmonic averaged over the gap G and normalized to the input magnitude. The width A and the height C of the grating teeth are scanned (see figure 2.6). The periodicity $\lambda_g = 2.05\,\mu\text{m}$ and the gap G of $2.3\,\mu\text{m}$ were kept constant. The design goals are a maximum magnitude of the first spatial harmonic and a small dependence of that magnitude on a variation of the parameters A and C to limit the influence of manufacturing imperfections. The magnitudes of the coefficients of the fundamental spatial harmonic a_0 and the first spatial harmonic a_1 behave inversely. When the incoming laser is reflected and the fundamental spatial harmonic propagating through the gap is small the evanescent fields are more pronounced. When we look at the grating as an effective material the structure can be seen as an etalon. The width A sets the filling factor of the material and thus influences the effective dielectric constant seen by

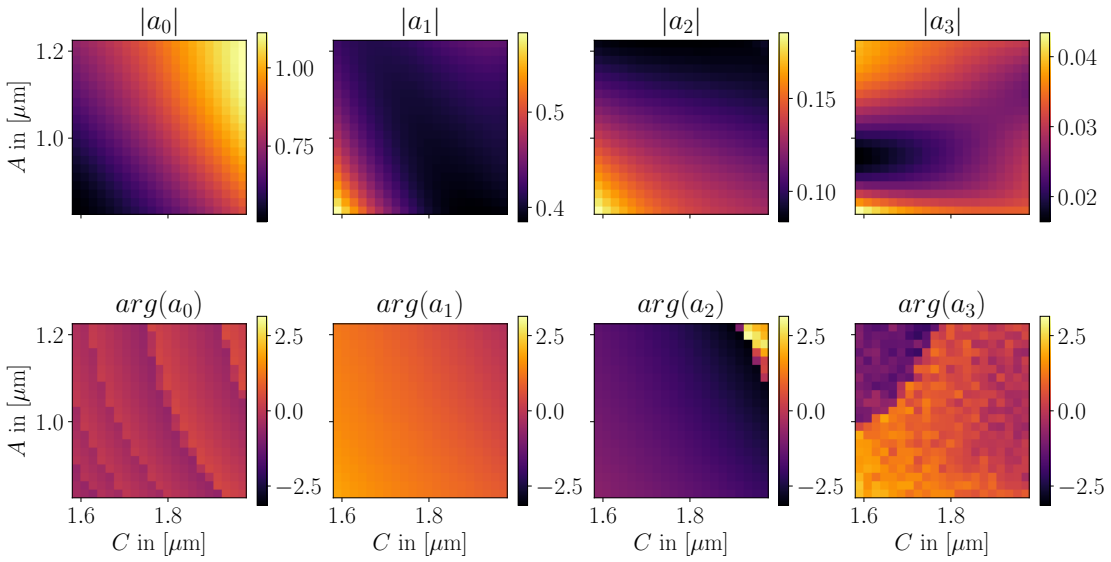

Figure 3.2: The field solver results for a fused silica double grating with single-sided illumination. The laser wavelength λ_l and the grating length λ_g are 2.05 µm. The top row shows the magnitude of the respective spatial harmonic normalized to the incoming laser amplitude. a_0 is the fundamental spatial harmonic. The magnitude and phase of the first spatial harmonic a_1 is relatively constant in the region around the chosen design values $A = 1.78$ µm and $C = 1.025$ µm. This means that the coupling behavior into this spatial harmonic does not change when A and C are changing within the manufacturing uncertainties of around 10 nm. The absolute values of the magnitude decline with the order n of the spatial harmonic. a_1 behaves inversely to a_0. When the fundamental harmonic is strongly reflected the evanescent field is more pronounced. For the fundamental harmonic the structure behaves like an etalon, where A sets the effective dielectric constant and C the propagation length.

the fundamental harmonic. The height C sets a propagation length through the material. By changing these parameters the transmission or reflection through the grating is influenced comparable to an etalon.

Another important design parameter is the gap size G. The transmission of the fundamental harmonic through the structure is dependent on the resonant properties of the entire structure, again comparable to an etalon. Changing the gap G changes the propagation length. Figure 3.3 shows the mean magnitude of the first spatial harmonic averaged over the gap G normalized to the input power for teeth height $A = 1.78$ µm

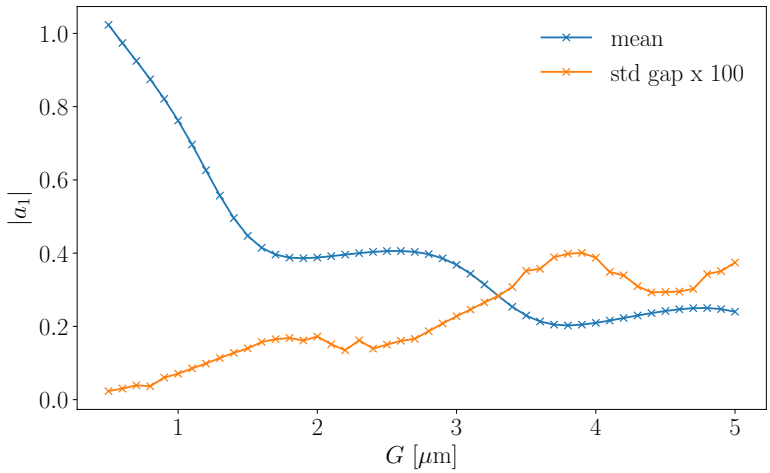

Figure 3.3: Mean magnitude normalized to the incoming field magnitude of the first spatial harmonic and the standard deviation of this magnitude over the gap G as a measure of the uniformity from the field solver. For the design gap of $G = 2.3\,\mu\text{m}$ again a region is chosen that has small dependence on gap size deviations in the manufacturing process. The value is rather large to achieve sufficient transmission of electrons. The acceleration gradients achievable are still reasonable compared to smaller gap sizes. Apparent is the exponential decay of the magnitude with larger gap G and the superimposed etalon behavior.

and width $C = 1.025\,\mu\text{m}$. An overall exponential decay with increasing gap size G is apparent, but it is superimposed by an etalon effect from the collective properties of the dielectric layers. Again a region was chosen where a change in the gap width G has no strong influence on the coupling into the spatial harmonic. It is also notable that with gap sizes G larger than the laser wavelength λ_l significant coupling into the first spatial harmonic is possible.

Figure 3.4 shows the dependence of the magnitude and phase of the first three spatial harmonics in dependence of the position along the gap G for the design parameters from table 3.1. It is observable that the magnitude and phase of the speed-of-light first spatial harmonic is very flat even for the single-sided illumination. This leads to a transversely independent acceleration gradient inside the DLA.

The periodicity of the structure plays an important role by setting the phase velocity of the matched spatial harmonic. Since the phase velocity can also be tuned by changing the incident angle of the incoming drive laser a speed of light structure is chosen. Figure 3.5 shows the dependence of the mean acceleration averaged over the gap G against the matched β_p normalized to the magnitude of the input drive laser. Also the standard deviation of the accelerating fields over the gap is given as a measure of uniformity over

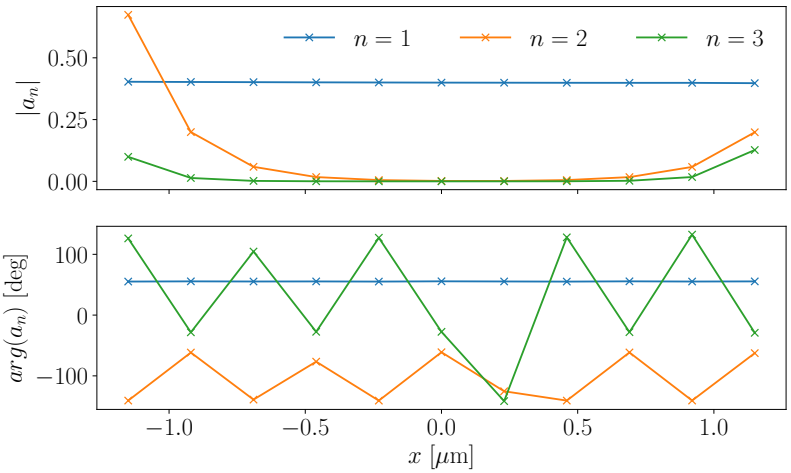

Figure 3.4: Magnitude and phase of the spatial harmonics from the field solver over the gap G for the design parameters A, C and G. The phases at small magnitudes of a_n are meaningless, since the phase calculation is unstable if real and imaginary part are close to zero. It is apparent that although single-sided illumination is used a strong uniformity of the first spatial harmonic over the gap is observable in amplitude and phase.

the gap G. Close to the speed of light phase velocity the standard deviation is very close to zero as expected from the speed of light fields.

Finally the offset of the two gratings in z-direction was scanned. The fabrication process lined out in chapter 5 involves the bonding of two gratings on the wafer level. The bonding process is has an uncertainty in the order of the grating period, thus the offset is scanned over the whole period range. Figure 3.6 shows the coupling for different offsets. The minimal coupling of 0.25 is the one assumed in the following performance predictions.

The parameter scans show that the gratings are very robust against the manufacturing uncertainties expected around 10 nm as long as a parameter set is chosen that lies in a region where the dependence of the coupling into the first spatial harmonic on the parameters is flat. The parameters for the fused silica samples are given w.r.t figure 2.6. A design according to figure 3.7 using silicon as the grating material was devised by the same method. The chosen parameters for both designs are summarized in table 3.1.

3.2 Per-period Interaction Tracking

This section is based on [79] and [80] published by the author.

Due to the short wavelengths used in DLAs full particle-in-cell simulations become highly computation resource demanding. To be able to do design work on longer interac-

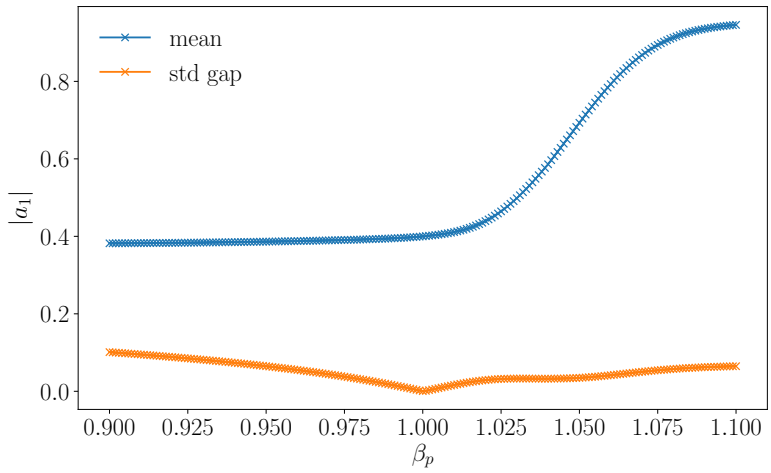

Figure 3.5: Again the mean magnitude of the first spatial harmonic normalized on the incoming field magnitude is plotted over the matched β_p. This corresponds to a change in periodicity of the grating. Again it is apparent that the coupling into the harmonic does not change significantly with small changes in periodicity around the design $\beta_p = 1$. A mismatched periodicity would lead to a phase slippage of a speed of light particle interacting with the grating fields.

tion lengths to get to particle energies in the GeV regime a different simulation approach is necessary. Different approaches based on the modeling of the particle dynamics for one DLA wavelength were proposed [81, 82]. Here another method is presented based on transfer maps capturing the dynamics of single particles in one grating period without any resonant particle approximations.

In this section we limit the study on a transversely dual illuminated double grating structure with rectangular shape according to figure 2.6 as discussed in the previous chapter 2. The configuration with in-phase drive lasers in p-polarization is used, which exhibits the most suitable properties for pure acceleration. In the y-direction only a magnetic field is present yielding no transverse forces in that direction. A speed of light phase velocity of the first spatial harmonic is chosen.

3.2.1 Numerical Methods

The results of a single grating period simulation with CST particle studio [78] were used to perform single particle tracking parameter sweeps at different particle energies, transverse positions over the gap G and entry angles. The transverse positions, angles and energies after one grating period dependent on the electron to laser phase were retrieved from the simulation. From this data a multivariate polynomial model was derived [83].

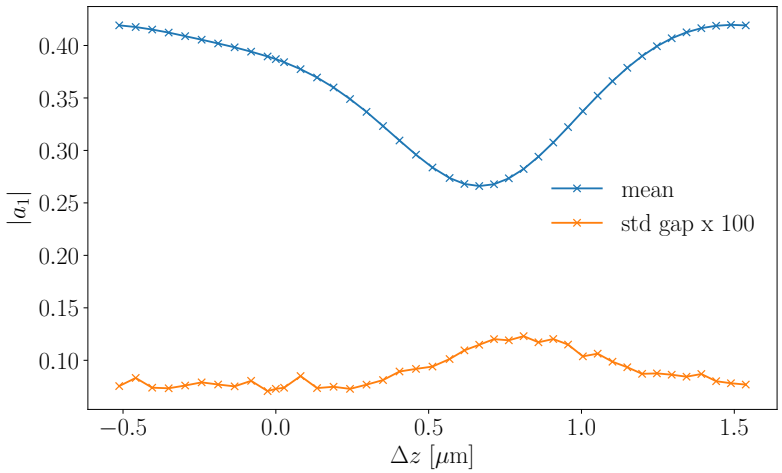

Figure 3.6: Mean magnitude of the first spatial harmonic normalized on the incoming field magnitude is plotted against the offset of the two gratings in z-direction as expected from the manufacturing process. In the worst case the coupling to the first spatial harmonic is 0.25 at $\Delta z = \lambda_l/3$. This is the coupling that is assumed in the following predictions of the performance.

The position and phase were varied by a multi-particle tracking run, energy and angle were scanned over multiple runs. The figure 3.8 shows exemplary data. A number of polynomial fitting runs in which random data points were omitted were performed and the distance between model prediction and these omitted data points were computed. This score can be used to represent the fitting accuracy. This method was used to determine the minimum polynomial order to fit the presented data sufficiently correct and to check against over fitting. A fifth order polynomial was chosen.

With this model transfer maps can be used to track a particle from one period to the next. The electron to laser phase slippage is calculated analytically from the particle energy, assuming the energy gain per period is small compared to the particle energy and that the angles of the particles to the accelerators longitudinal axis are small. The

Table 3.1: Parameters for the DLA

Parameter	**Fused silica**	**Silicon**
C	1780 nm	720 nm
A	1025 nm	1025 nm
G	1000 nm or 2300 nm	2050 nm
λ_g	2050 nm	2050 nm
L	1 mm	1 mm

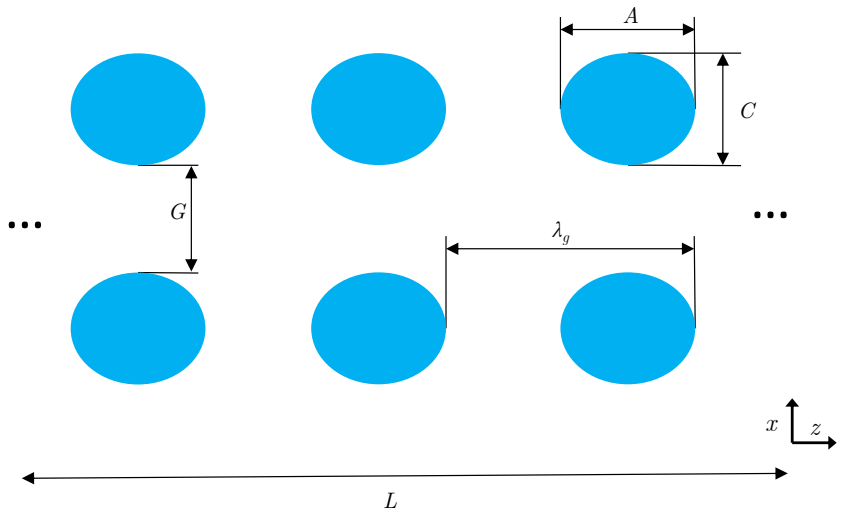

Figure 3.7: Design of the DLA manufactured from silicon in a top down etching process. A picture of a fabricated device can be seen in 5.11. Here the assumption of long pillars in the free direction is usually not fulfilled due to the limited etching depth. This leads to non-uniform acceleration gradients in the y-direction.

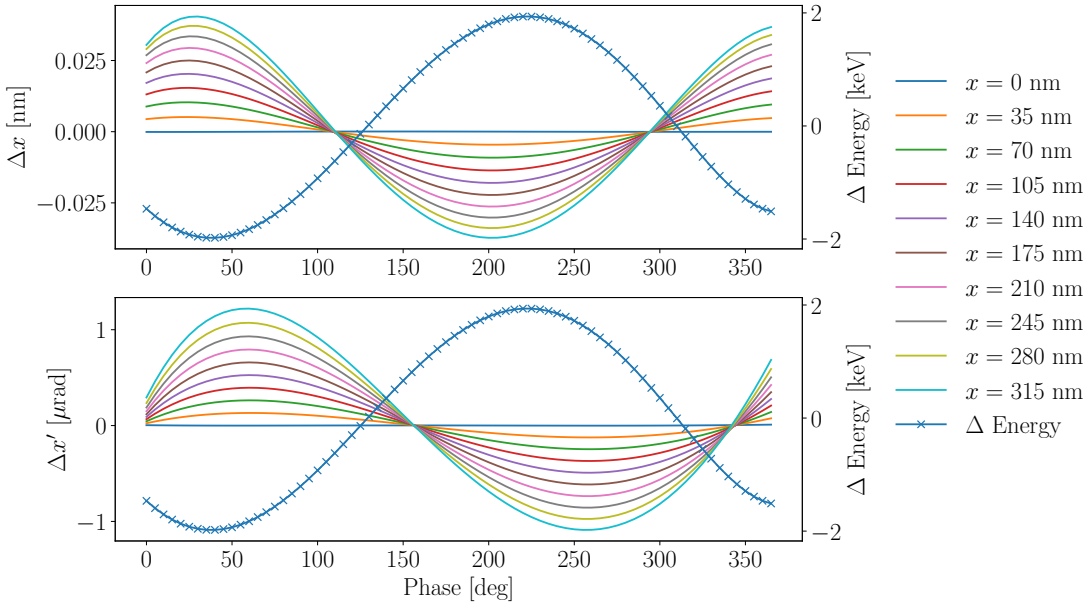

Figure 3.8: Electron to laser phase scan from the polynomial model for one grating period. The plots show the position offset and kick for different transverse starting positions for x'_0 =0 rad and E_0 =100 MeV. The second axis shows the energy gain dependent on this phase. In the range from 200° to 300° an initial positive position offset has a negative angle offset, negative position offset and energy gain.

simplecticity of the mapping is generally lost, since the order of the fitted base polynomial is limited. Due to the good fitting accuracy and the limited number of periods that are simulated for linear accelerators this influence can be neglected. Space charge and other collective effects are also neglected for now due to the relativistic particle energies and low charges aimed at in DLA experiments. Work on wakefields and beam loading in dielectric gratings can be found i.e. in [84]. An overview of the procedure is given in figure 3.9.

To check the model a comparison with a 3D tracking simulation for a few grating periods was carried out in CST [78]. Mid range numbers of periods were also checked against a linear interpolation representation of the parameter sweep data, again as a consistency check for over fitting the model to the data. These comparisons show good agreement with the polynomial model.

The proposed method shortcuts the calculation of the fields of every grating period. Due to the periodicity of the structure the field calculation can be carried out for a single grating period. A parameter sweep can be done with a tracking code with the precalculated electromagnetic fields. Linearization of the parameter data and fitting to a fifth order polynomial via linear regression is fast. The linear interpolation scheme has a higher computation cost and was only used to verify the polynomial fitting in addition

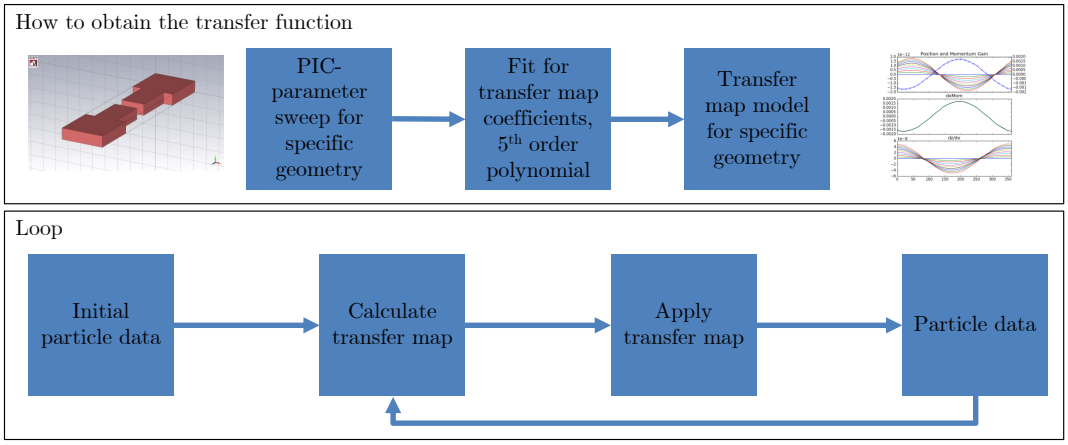

Figure 3.9: Overview of the simulation procedure for the per-period-interaction code. Via parameter sweeps the state data of single particles are generated and then fitted to a 5th order polynomial model. From the particle initial data the transfer maps can be calculated and applied, thus the particle is tracked from period to period of the grating.

to the standard cross correlation schemes. A drawback of the method is that changes in the structure design make a new particle tracking parameter sweep and fitting run necessary.

The calculation of the particle data with the polynomial model in 5th order takes only fractions of the resources of a full scale particle-in-cell code, Where the whole structure with all its periods has to be modeled in the simulation domain. Due to the size of the necessary simulation domain even for hundreds of drive laser periods a calculation using a closed model in a PIC code is only practical in combination with a high performance computing cluster. But a simulation period by period transferring the particle parameters is feasible even on a workstation.

3.2.2 Comparison with full PIC Simulation

The ARES linac design is well suited to produce ultra-short high-quality electron bunches to be injected into DLAs. Table 3.2 shows a typical working point achievable in simulation.

A drive laser with a wavelength $\lambda_l = 2000\,\mathrm{nm}$ is assumed, which was the initial

Table 3.2: ASTRA simulated working point at the DLA center within the experimental area for minimal bunch length using velocity bunching, courtesy F.Mayet

Parameter @ IP	**Value**
Charge	0.5 pC
Bunch Length FWHM	2.1 fs (0.3 * λ_0)
E [MeV]	99.1 MeV
ΔE/E	0.12 %
σ_{xy}	7.8 µm
$\epsilon_{n,xy}$	105 nm rad

specification within the ACHIP collaboration. Using this wavelength which corresponds to a period of 6.67 fs a net gain in particle energy is possible since the bunch only covers a limited phase range of around one third of the accelerating field. A drive laser pulse of 120 fs length is assumed. The temporal and spatial shape of the laser pulse are Gaussian. Table 3.3 shows the collected laser parameters. The maximum electric field amplitude in the channel for a pulse energy of 14 µJ is around 4 GV/m. These parameters are still well below the anticipated damage threshold of fused silica [85]. To have the maximum possible energy gain the interaction length is elongated by introducing a 45° pulse front tilt to the DLA drive pulse. The resulting interaction length is 100 µm. The DLA for the simulation has ca. 50 periods.

Table 3.3: Gaussian laser pulse parameters

Parameter @ IP	**Value**
Wavelength	2 µm
σ_t	120 fs
Energy	14 µJ
σ_x	50 µm
σ_y	10 µm

The particle-in-cell code from CST Studio Suite 2017 was used for this simulation. A grating type pillar structure with 50 periods of fused silica illuminated from both sides was simulated (see figure 2.6 and table 3.4). Spatially a Gaussian intensity profile of the laser is assumed. The electron beam is assumed to be collimated horizontally to the gap size of the DLA and to a full width of 10 µm in vertical direction allowing only small transmission of around 25 fC. The beam size does not change significantly along the structure.

At the phase of the highest achievable energy gain the bunch from the ARES simulation was injected. The same particle distribution was propagated using the in-house code.

In figure 3.10 the energy spectra of the bunch after the DLA are shown. The first histogram shows the spectrum without laser illumination. In the second histogram the

Table 3.4: Parameters for the DLA vs. PIC comparison

Parameter	GeV DLA Silicon
C	1740 nm
A	1000 nm
G	740 nm
λ_g	2000 nm
λ_l	2000 nm
L	100 µm

spectra from the PIC simulation and the per-period-code with laser illumination are plotted, which are in very good agreement. The transverse phase space is virtually the same in all three scenarios, due to the short interaction and propagation length. An interaction with the structure due to wakefields and beam loading are not visible in the spectrum, which is to be expected due to the symmetry of the beam and the low charge. The spectrum with the laser field shows a mean net gain in particle energy of 43.2 keV. This corresponds to an effective acceleration gradient of 432 MeV/m.

It was shown that under the assumed conditions net acceleration in a DLA structure is possible at the ARES linac in simulation. Furthermore it was shown that the in-house code can be used to model the electron-DLA-interaction under the assumed conditions.

3.2.3 Example: The GeV-DLA

An extended DLA interaction was simulated using the in-house code. The analysis contains several aspects testing the possibilities of long interaction DLAs. One is transmission through a long DLA starting already at relativistic speeds by leveraging the high brightness beams from RF injectors. Another aspect are the injection requirements to achieve zero particle loss. Additionally the capabilities of the developed method for long DLA simulations were tested.

The parameters of the fused silica grating are given in table 3.4 and in figure 2.6 except for the length $L = 1.1$ m. The design was chosen to have no additional external focusing. A ponderomotive, RF-focusing like effect caused by the higher order spatial harmonics is expected [72]. The electron-to-laser phase was reset using idealized field-free drift spaces between the modules, which incorporated an additional alternating phase focusing effect [86]. This method is a candidate for stable, bunched beam DLA designs [87]. Another approach on stable electron beam transport in DLAs using the increasing or decreasing drive laser amplitude in short laser pulses is investigated in [88].

Figure 3.8 shows energy gain, transverse offsets and changes in angle from one DLA period. For a resonant particle the energy gain and angle changes should have a 90 deg phase shift (Panofsky-Wenzel theorem). But the energy gain curve is shifted with respect to the transverse forces due to the phase slippage that occurs although the initial particle energy is at 100 MeV. This is due to the low α parameter of these structures. The

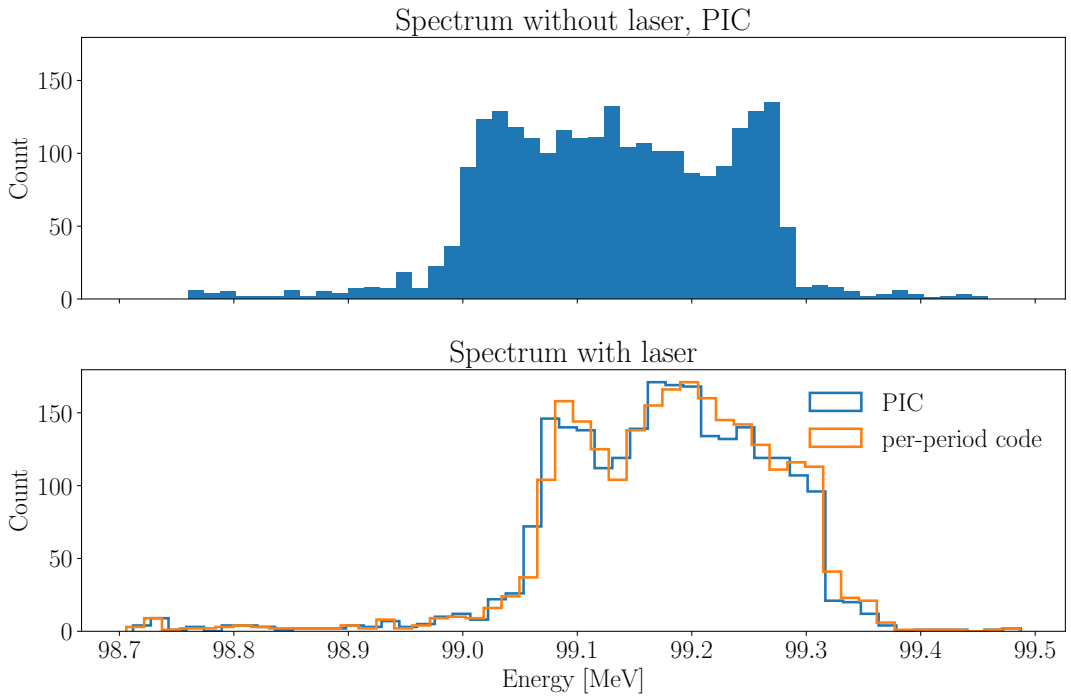

Figure 3.10: Histograms of the particle energy distribution after the DLA. The top histogram is without the laser field. The bottom plot shows the histograms from the PIC simulation and the per-period-code with laser illumination. The spectra show good agreement.

resonant transverse focusing forces are superimposed with a higher order RF-focusing effect. Still it is apparent that a phase range with transverse stability will exhibit longitudinal instability as expected from the dominance of the first spatial harmonic that is approximately matched to the particle velocity. A particle bunch in a transversely focusing phase range will be longitudinally defocused. Even at the relatively high initial particle energy velocity effects play a role, due to the short drive laser wavelength (thus low α) and can only be neglected for particle energies of approximately 500 MeV and higher.

Since the field assert a force charged particles only in the x-z-plain, after a number of periods the grating is rotated orthogonally around the longitudinal axis to achieve focusing in both transverse directions as shown schematically in figure 3.11.

Even as the particles become more relativistic the phase slippage has to be considered, since the simulated device is hundred thousands of periods long. Field free drift sections were introduced to correct the electron to laser phase. This is necessary to keep the particles in a focusing and accelerating phase as described in figure 3.8. A starting energy of E_0 =100 MeV was chosen to limit the phase slippage to reasonable values and

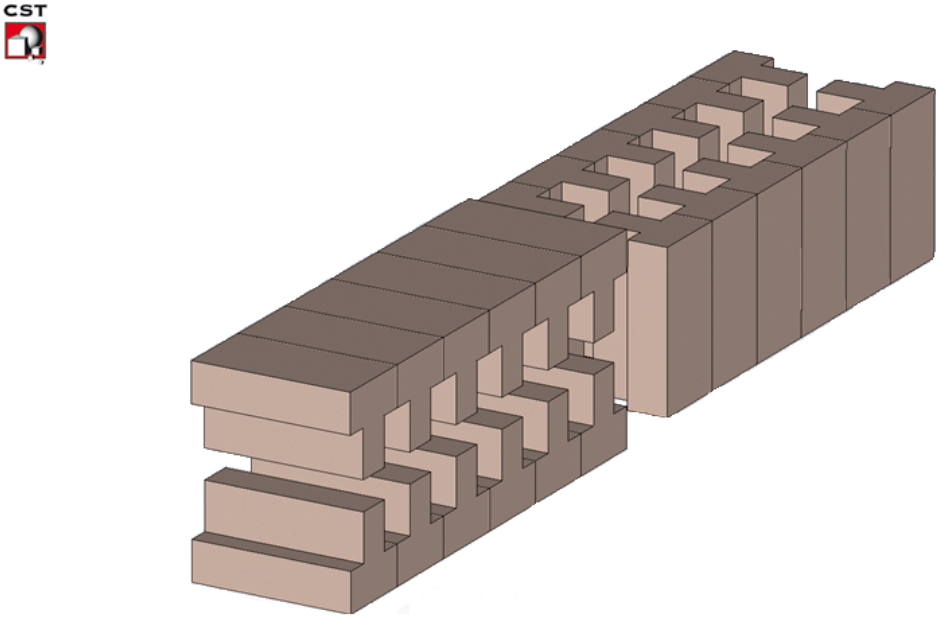

Figure 3.11: Schematic of the rotated grating stages. In the simulation one stage consists of 100 periods.

to leverage the high-brightness low-emittance beams that can be obtained from S-band photoinjectors like ARES [24]. An uncorrelated relative energy spread of $\frac{\Delta E}{E}$ =3.46 % is assumed, which is conservative w.r.t. the achievable parameter range of modern conventional accelerators [89]. The beam emittances before and after the DLA were derived from the simulation by equidistant filling of the phase space and flagging lost particles. The target energy will be E_f =1 GeV.

The laser wavelength is chosen to be 2 µm and so is the grating period to accelerate in the first spatial harmonic. The illumination over the DLA stages is assumed to be distributed evenly in longitudinal and transverse direction. A laser spot size was considered with a pulse front tilt resulting in 5 µm x 25 µm spot size. Here other technical issues are not further addressed, i.e. the details of the laser pulse distribution to the gratings. Considerations towards that topic using integrated waveguides for power distribution and in-coupling to the chip from optical fibers can be found i.e. in [64].

Laser pulse energy requirements for the stages are estimated from the field amplitudes of the electromagnetic simulation. For all the acceleration stages a few tens of mJ would be sufficient, neglecting beam loading due to low charge. The laser power distribution will have significant losses in the range of 90 % or higher, which would make a laser source in the hundreds of mJ to single digit joule range necessary.

The laser field amplitude at the grating of 2 GV/m is assumed with an efficiency into the first spatial harmonic of $\eta = 0.5$. After 550 000 periods the design particle reaches an energy of 1.041 GeV. This corresponds to an effective acceleration gradient

of G_{acc} =946 MeV/m and a length of the setup of 1.1 m.

Sweeping over the available parameter space for the initial particle angles, positions, energies and phases yields a maximum available transverse and longitudinal phase space. From there a viable normally distributed electron bunch was estimated. The phase space projections and emittance initial electron bunch are shown in figure 3.12 generated with ASTRA [90]. The central electron to laser phase was chosen to be $\phi_0 = 180°$. For this configuration there is significant charge loss due to the collimation of the beam by the accelerator (see figure 3.13) which results in a smaller final emittance.

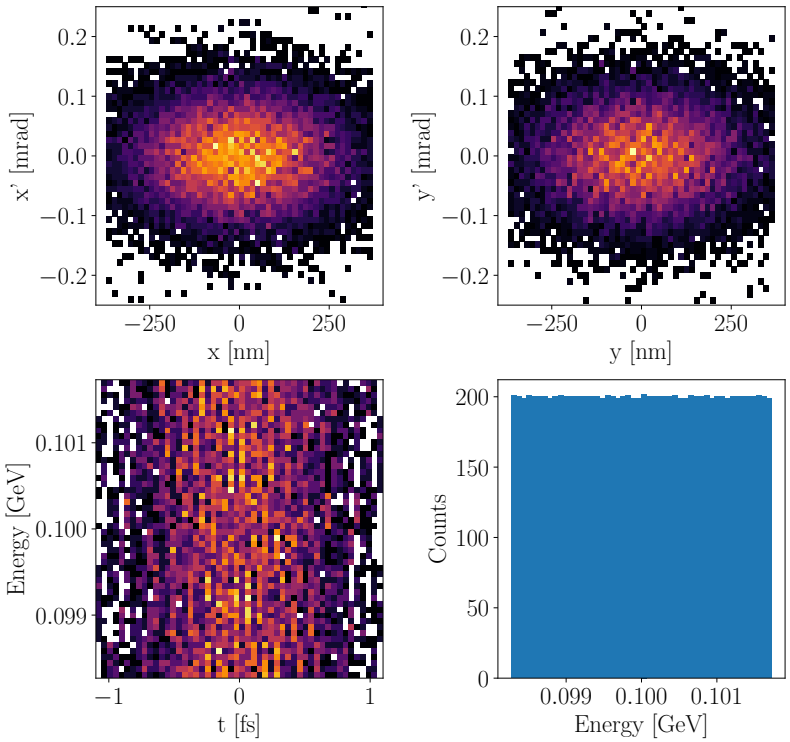

Figure 3.12: Phase spaces and spectrum of the initial electron bunch before the DLA. The normalized transverse emittance at 100 MeV is $\epsilon_{trN} = 10\,\text{nm rad}$. The uniform energy spread is $\frac{\Delta E}{E} = 3.46\,\%$. The bunch charge is $Q = 0.8\,\text{fC}$ and the rms bunch length is $\sigma_t = 0.5\,\text{fs}$. The transverse rms beam size is $\sigma_{x,y} = 162\,\text{nm}$.

In figure 3.14 the fraction of the initial bunch that passed the whole accelerator is shown with its parameters. Since collective effects are neglected, this could be an actual viable bunch. These would be the to-be-delivered parameters from a 100 MeV source, if

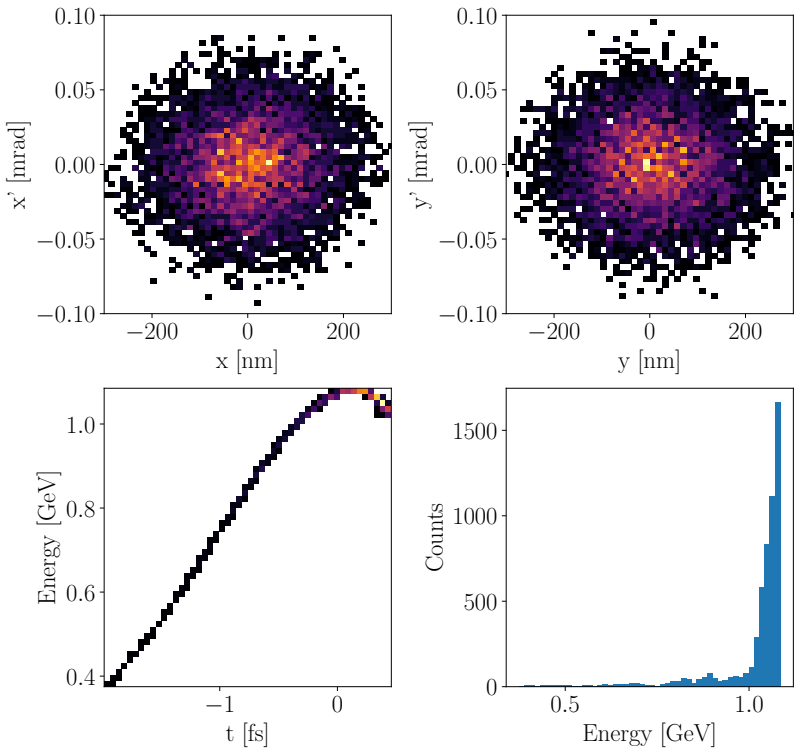

Figure 3.13: Phase spaces and spectrum of the final passing fraction of the electron bunch after the DLA. The normalized transverse emittance at 1.012 GeV is $\epsilon_{trN} = 3.5\,\text{nm rad}$. The rms energy spread is $\sigma_{\Delta E} = 119\,\text{MeV}$. The final bunch charge is $Q = 0.45\,\text{fC}$ and the rms bunch length is $\sigma_t = 0.47\,\text{fs}$. The transverse rms beam size is $\sigma_{x,y} = 104\,\text{nm}$.

no charge loss is desired. Noticeable is the emittance blow up from $\epsilon_{trN} = 0.08\,\text{nm rad}$ to $3.5\,\text{nm rad}$. One reason is the phase dependent focusing strength. Different longitudinal positions in the bunch correspond to different focusing strengths so that depending on that position the betatron oscillations will have different periods. This leads to a fanning out in transverse phase space. A more detailed view on this effect is presented in [91]. This effect decreases with decreasing electron bunch length. Another reason are the non-optimized drift sections introduced for electron to laser phase correction. These should ideally be placed so that the Courant-Snyder parameters match from section to section. Finally a non-linear component in the transverse and longitudinal forces is expected, due to filling the entire aperture with electron beam.

It was shown that the presented method can be used to simulate grating-based DLAs

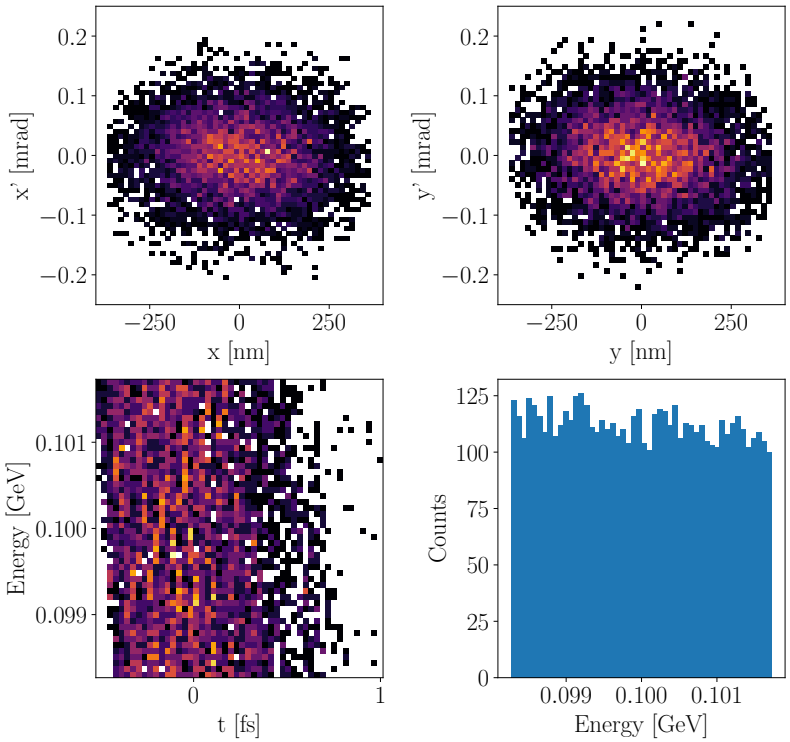

Figure 3.14: Phase spaces and spectrum of the passing fraction of the initial electron bunch before the DLA. The normalized transverse emittance at 100 MeV is $\epsilon_{trN} = 0.08\,\mu\text{m}\,\text{mrad}$. The uniform energy spread is $\frac{\Delta E}{E} = 3.46\,\%$. The bunch charge is $Q = 0.45\,\text{fC}$ and the rms bunch length is $\sigma_t = 0.29\,\text{fs}$. The transverse rms beam size is $\sigma_{x,y} = 146\,\text{nm}$. These parameters would correspond to the output of an electron injector when no particle loss is expected.

with large numbers of periods efficiently. The presented example DLA design can be a starting point for the development of a more sophisticated, realistic model. The posed requirements on a pre-accelerator to achieve the beam parameters for zero particle loss are challenging. Although these values can probably be improved by altering the drift sections to match the beam and improving the alternating phase focusing of the model. Compact sources like RF guns are able to produce collimated electron beams with emittances below 1 nm rad [92].

4 Novel Concepts for Dielectric Gratings as Particle Beam Diagnostics

In this chapter the beam manipulation and diagnostic capabilities of dielectric gratings are explored in accordance with the second ACHIP goal. The first section is concerned with illumination polarization configurations that show transverse deflecting behavior on a charged particle beam. This kind of structure can either be used as a beam manipulation device to correct the trajectory in a longer interaction DLA or as a streaking device. High transverse fields and short wavelengths can be used to streak short electron bunches and in combination with a downstream screen can be used as a method to characterize the longitudinal current profile. The second section introduces a new design for a bunch length measurement device for ultra-short electron bunches based on dielectric gratings.

4.1 Deflecting Structures

This section is based on [93] by the author.

Deflecting structures can be useful particle beam diagnostics for short electron bunches or they can be used to manipulate a beam trajectory within a DLA. In this section three candidates for the deflection of particles are investigated via particle tracking simulations.

Again a fused silica double grating alike figure 2.6 is investigated with parameters according to table 4.1. It is straight forward to investigate grating based schemes for manufacturing compatibility with an integrated grating based accelerator design. The periodicity of the grating is matched via equation 2.97 to a particle energy of 5 MeV for the first spatial harmonic. For the different deflecting schemes the polarization and phase between the two excitations are varied.

Table 4.1: Parameters for the DLA

Parameter	**Fused silica**
C	1740 nm
A	1000 nm
G	740 nm
λ_g	1994 nm
λ_l	2000 nm

The first investigated scheme is a pure s-polarization with both drive lasers in phase (see figures 2.5 and 2.6). The deflection now should occur in the y-direction and is not limited by the grating aperture. From equations 2.105 we can derive an equation for the transverse forces alike equation 2.114 (see also [65]):

$$F_{\perp,1} = -eE_0 e^{-i\omega t}\hat{\mathbf{y}} \sum_n (1 - \beta_p/\beta_n) a_n e^{ik_n z}. \tag{4.1}$$

This corresponds to a pure deflection mode without any transverse dependency (for β_n close to one and $G \ll \Lambda_n$) or longitudinal forces. Unfortunately from the term $(1 - \beta_p/\beta_n)$ it is obvious that the transverse forces vanish with $\beta_p \to 1$. Only small transverse forces are expected for more relativistic particles.

For the second scheme a pure p-polarization is considered with the drive lasers set off by 180° canceling out the accelerating fields and amplifying the transverse components. In this configuration the deflection forces appear in the direction limited by the double grating aperture, thus limiting the achievable β-function. The transverse forces and longitudinal electric field can be derived from equations 2.106:

$$F_{\perp,2} = eE_0 e^{-i\omega t}\hat{\mathbf{x}} \sum_n \frac{k_n}{\Lambda_n}(1 - \beta_p\beta_n) a_n e^{ik_n z}, \tag{4.2}$$

$$E_{z,2} = E_0 e^{-i\omega t} \sum_n a_n x e^{ik_n z}. \tag{4.3}$$

This configuration including the term $(1 - \beta_p\beta_n)$ has the same problem of a vanishing deflecting force, but counteracted by Λ_n approaching zero for $\beta_n \to 1$. Another drawback is the of-axis longitudinal electric field component that will add to the energy spread in addition to the expected contribution predicted by the Panofsky-Wenzel theorem, when used as a streaking device.

The third scheme is from [94] and is based on a rotation of the whole acceleration structure and an in-phase p-polarization excitation so that the force has an additional strong transverse component w.r.t the beam axis. The polarization of the electric field of the laser is still perpendicular to the direction of the grating groves but the beam direction is rotated according to the primed coordinate system in figure 4.1. In this configuration the periodicity of the grating is adjusted with a modified matching condition:

$$\lambda_g = \beta n \lambda_l \cos\alpha \tag{4.4}$$

Here the parameter α is the rotation angle of the two coordinate systems. There will be a transversely uniform force component in the longitudinal direction that will induce additional energy spread if used as a streaking device. This will be a longitudinal chirp instead of a transverse chirp expected from Panofsky-Wenzel theorem. The spatial harmonic w.r.t to the non-primed coordinate system is not at speed of light phase velocity thus exhibiting strong transverse forces in the non-deflecting direction.

Table 4.2: non-vanishing forces of the deflecting schemes

Component/Scheme	**1**	**2**	**3**
F_x	-	deflecting	focusing
F_y	deflecting	-	deflecting
F_z	-	linear in x	acceleration
polarization	s	p	p, rotated

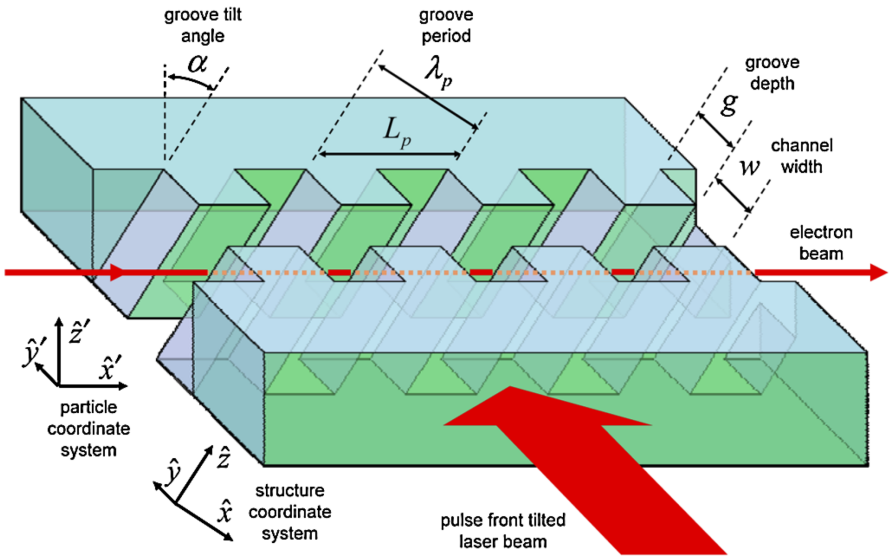

Figure 4.1: The figure shows the scheme 3. The whole structure is rotated so that the electron beam travels through the gap at an angle relative to the grating grooves. The polarization stays in p-polarization with respect to the grating grooves. The matching condition is altered w.r.t. equation 4.4. Figure taken from [94] by T. Plettner.

To get numerical values for the deflecting strength CST PIC [78] simulations were set up with the parameters from table 4.3 for one grating period with a point source test beam and excited by plane waves. The deflection or streaking voltage is laser-to-electron phase dependent and the maximum is shown in table 4.4 for an on axis start particle. It is important to notice that these values are only appropriate for 5 MeV. For scheme 1 and 2 the forces will decrease with increasing particle energy and thus increasing matched β_p. The dimensions of the grating used in the simulation are shown in table 4.1 and figure 2.6.

Additionally the magnitude of the transverse force from the acceleration structure is investigated for comparison. It is important to note that the force is also position dependent and particles at the center of the gap are not kicked. This is comparable to a focusing or defocusing of an electron beam. Here the offset for the test beam is 150 nm

from the gap center.

Table 4.3: Simulation Parameters

Parameter	**Value**
Wavelength	2 µm
Laser Amplitude	$2\,\mathrm{GV\,m^{-1}}$
Particle Energy	5 MeV

Table 4.4: Simulation results

Scheme	**1**	**2**	**3**
Per-cell streaking voltage [V]	20	100	170
Defl. plane	unlimited	limited	unlimited

Scheme 1 has only limited deflection forces. The electric field and the effect of the magnetic field are canceling each other. In scheme 2 the beam size and with that the beta-function in the device is limited by the aperture of the structure which limits the longitudinal resolution in a streaking application (see equation 4.5). For beam manipulation the scheme may still be feasible. Schemes 1 and 2 may only be feasible candidates for deflection or streaking devices for low particle velocities β_p.

Scheme 3 has the strongest deflection forces but inherently has longitudinal forces in the same order of magnitude, which would add to the energy spread of the streaked particles. Both schemes have transverse forces an order of magnitude stronger than the focusing/defocusing forces of the acceleration structure. In figure 4.2 the relations of the forces for the different schemes are shown.

Due to the dependence of the deflecting force on the laser-to-electron phase and the short laser wavelength only ultra-short bunches can be manipulated using these devices. For use as a streaking device the maximum bunch length is limited to below one quarter of the driving wavelength. With the equation from [95] for the longitudinal TDS resolution for electrons at optimal phase advance to the detector screen

$$\sigma_z = \frac{\sqrt{\epsilon_y} c^2 |p|}{\sqrt{\beta_y} 2\pi f_0 e V_0} \tag{4.5}$$

one can see that a large beta function at the TDS (β_y) is beneficial for the longitudinal resolution. The limited beta function due to the smaller apertures of DLAs can be compensated by the high frequency (f_0) of the incoming fields. The high intensities achievable lead to a high streaking voltage V_0. The remaining quantities are the transverse emittance ϵ_y, the elementary charge e and the particle momentum p.

Scheme 3 is a candidate that can be readily tested using the experimental capacities at ARES as lined out in chapter 5.

The schemes investigated within this section all have significant drawbacks that can be

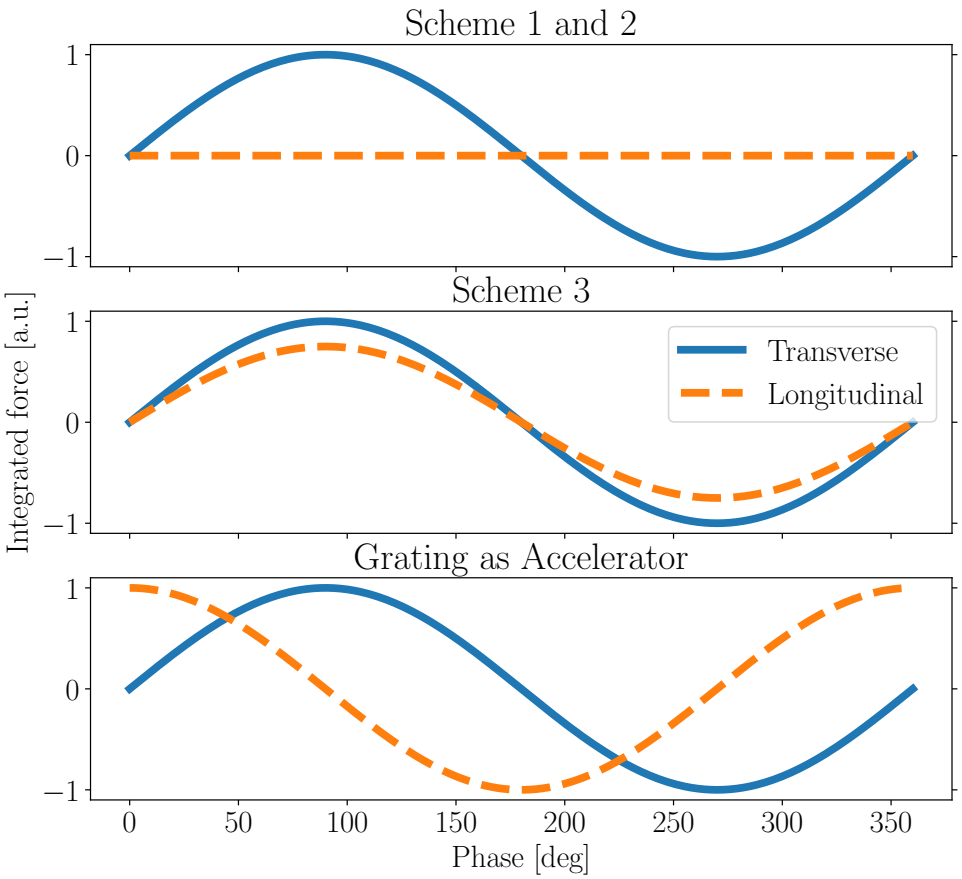

Figure 4.2: The top graph shows the dependency of the transverse and longitudinal kicks for scheme 1 and 2 at the center of the gap C. There are no significant longitudinal kicks apart from the off axis contributions. The middle graph shows the relation for scheme 3 where significant longitudinal and transverse kicks are in phase. The third graph shows the relation for the grating used as an accelerator. There the transverse forces are of focusing/defocusing nature.

overcome by the configuration devised in [65, 96]. In this work the device is presented as a laser driven undulator. A superposition of p- and s-polarization is used that yields a pure speed of light phase velocity deflecting mode without additional transversely uniform longitudinal electric fields (still the off-axis longitudinal field components remain). The deflection takes place in the direction of the grating aperture limiting the use as a streaking device. This scheme could also be readily tested at the experimental chamber

at ARES.

4.2 Bunch Length Diagnostic for Ultra-short Particle Bunches

Smith-Purcell Radiation (SPR) [97] from metallic gratings has been studied since the 1950s. The description of the fields from the metallic gratings is very similar to the dielectric gratings. A metallic grating passed by an electron with relativistic speed β_p will radiate at a certain wavelength λ_e depending on emission angle θ:

$$\lambda_e = \frac{\lambda_g}{n_d}(\cos\theta - 1/\beta_p). \tag{4.6}$$

The equation can be derived from equations 2.93 and 2.96 by inverting the time dependence and taking the space charge forces from a charged particle as the driving field. Parameter n_d is the diffraction order, since for each spatial harmonic a different emission wavelength suffices the matching condition for a given phase or particle velocity β_p. The angle θ is again given with respect to the particle beam axis.

When generalized to a particle bunch the emitted radiation has a non-coherent part and a coherent part. The amount of non-coherent light produced is linearly dependent on the number of particles in the passing bunch. The intensity of the coherent part depends on the frequency content of the longitudinal current profile of the passing particle bunch that matches the period of the gratings spatial harmonics. The coherent part exhibits a quadratic dependence on the number of particles in this current. The bandwidth of the emitted radiation can be limited by a detector with an aperture like a slit on a certain distance and angle above the grating.

In simulation with CST PIC [78] a longitudinally Gaussian particle bunch with a variable bunch length σ_z passes a fused silica single-sided grating. Figure 4.3 shows the radiation at the wavelength of the grating at $\theta = \pi/2$ and the magnitude of the spectral content of the longitudinal current profile at the first spatial harmonic vs. the bunch length of the passing electron bunch. It is apparent that the two magnitudes are approximately proportional. All the bunches are short enough to have significant spectral content at the grating periodicity and have constant charge.

The rest of the spectrum in the other emission angles should exhibit the same dependence and also the higher diffraction orders. To leverage this behavior for a bunch length measurement a piecewise longitudinally chirped grating is employed. The different period gratings should be decoupled from each other so that the radiation from one grating is not measured by the detector from the neighboring grating. This is possible using dielectric gratings since they produce SPR on both sides as long as the material used is transparent at that wavelength. The detected radiated power should increase significantly when the bunch passes grating periods which match the bunches longitudinal harmonic content, i.e. when the bunch is shorter than the grating period. Dielectric gratings made from silicon can be lithographically produced down to the nm regime corresponding to hundreds of atto-seconds resolution. The electromagnetic properties

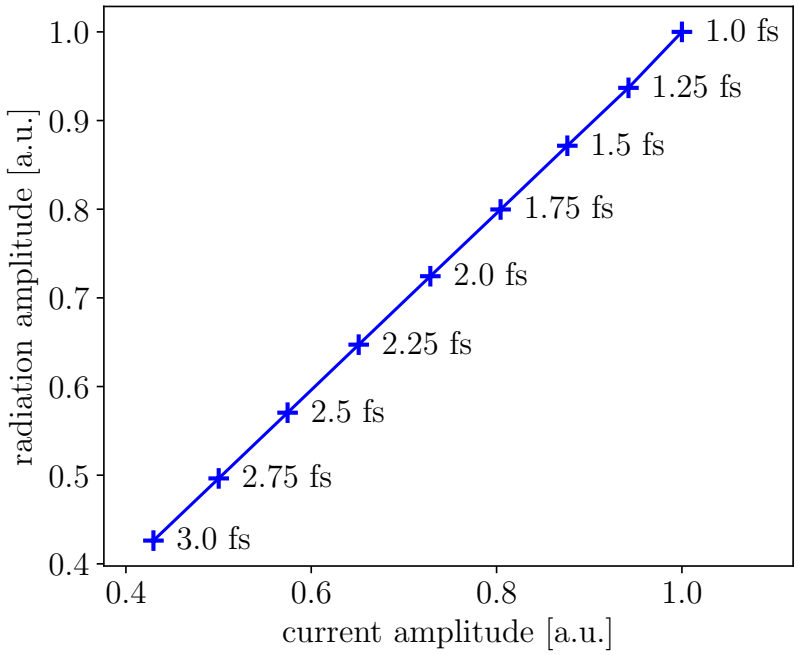

Figure 4.3: Amplitude of the frequency components with 2 µm wavelength of the current profile of a Gaussian electron bunch vs. the amplitude of the radiation at angle $\theta = \pi/2$ from a fused silica grating with 2 µm periodicity passed by this electron bunch from a PIC simulation. Each point for a different electron bunch length from 1.0 fs to 3.0 fs. The radiation amplitude is proportional to the current amplitude of the frequency component of the bunch current corresponding to the grating periodicity.

of dielectrics at these short wavelengths change drastically so the materials have to be chosen carefully.

In combination with a charge measurement the in-coherent part of the spectrum can be estimated and subtracted from the measured spectrum. The remaining portion then corresponds to the spectrum of the longitudinal charge profile.

The method described so far only gives the magnitude of the current spectrum and thus only allows for the measurement of a minimal bunch length by way of a form factor and an assumed bunch shape. For a full reconstruction of the current profile the phases are necessary. If the photon yield is high enough the signal from each grating element can be auto-correlated. And comparable to Frequency Resolved Optical Gating (FROG) [98] it should be possible to recover the relative phases of the frequency components. This would yield the (almost) complete spectral information at the sampled frequencies. Thus, allowing for a reconstruction of the bunch shape that is limited by the number of

discreetly sampled frequencies.

For a bunch with high charge like in an FEL the method can be single bunch compatible. It is generally parasitic due to the low expected photon yield. A charge calibration might be possible with a DC particle beam cutting the necessity of an additional charge measurement. A transversely symmetric setup is preferable removing the dependence on beam position on the total photon yield and even allowing the extraction of the beam position from the relative signal power in different directions. The resulting sensors would be very compact consisting of the dielectric gratings attached to suitable semiconductor detectors dependent on the operating wavelengths and separated by a non-transparent material as shown in figure 4.4. The device can be in the centimeter to millimeter scale depending on the operating wavelengths and lengths of the individual grating elements to provide sufficient photon yield.

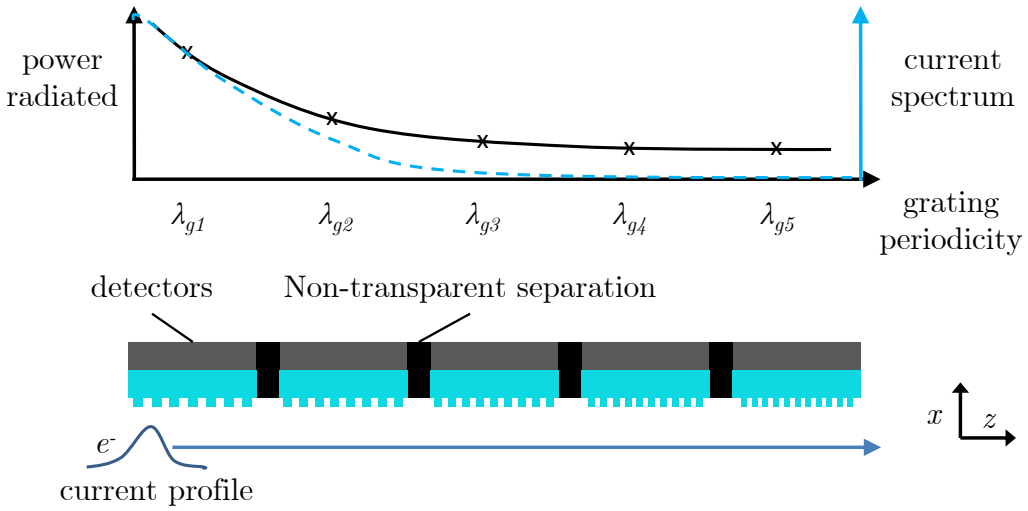

Figure 4.4: A schematic of the device design consisting of multiple dielectric gratings with different periodicity λ_{gn}. The semiconductor detectors are attached to the backside of the grating and separated by a non-transparent barrier. The Gaussian current profile of the electron bunch is assumed to have spectral content at λ_{g1} and λ_{g2} but not at the shorter periodicity gratings, where only the incoherent power level occurs. A coherent response is expected from a grating with periodicity longer than the bunch length.

The plausibility of such a device has been shown as a dielectric grating based beam position monitor [46]. It leverages the change in the spectrum of radiation from a transversely chirped grating by changing the beam position in the grating plane. The sensitivity of optical spectrometers to detect changes in this spectrum makes nm-resolutions possible if high enough beam current is present to produce sufficient photon yields.

The ARES facility is very well suited for a proof of principle experiment. In the simplest case the DLA samples already manufactured can be used. The bunch length provided by the ARES linac can be varied and the beam injected into the samples. The produced radiation can be analyzed and the dependence on the bunch properties can be experimentally verified. The planned X-band transverse deflecting structure [99] can be used to cross check the method.

To validate the proposed concept a proof-of-principle experiment should be conducted at ARES. A prototype device using gratings with different periodicity should be developed and tested. This already includes a significant design effort towards the materials to be used and their wavelength dependent electromagnetic properties. The method presented shows a path to a simple, robust and compact device for the characterization of ultra-short particle bunches w.r.t beam position, bunch charge, bunch length and potentially the longitudinal current profile.

5 Design of a Single-bunch Experiment at ARES

This chapter is partially based on [26] by the author.

An important step for the ACHIP project is to show net acceleration of electrons in a dielectric grating structure. The previously conducted experiments for relativistic electrons were based on sinusoidally modulating the longitudinal phase space of a longer particle bunch in the ps regime. In this chapter the design of an experiment for single bunch net acceleration is presented using fs bunches from an RF linac. The facility at which the experiment is going to be conducted is ARES presented in chapter 1. In this chapter the concept of the experiment is explained. A prediction of the performance based on simulations with various tools is presented in the third section. The technical implementation of the experiment is outlined in the fourth section. The last section of the chapter contains the commissioning status of the facility and a preliminary plan for the conduction of the experiment.

5.1 Concept of the Experiment

The ARES linac is foreseen to provide short bunches and small beam sizes to probe the limits of electron bunch compression. It is also well suited to provide electron bunches to be injected into novel particle accelerators like DLAs and plasma acceleration as well as for tests of novel diagnostic schemes and particle accelerator components.

Electron bunches will be produced in the gun on a metallic cathode by photo-emission. The two traveling wave structures will be used to compress the bunch longitudinally. A dedicated focusing system and particle beam diagnostics will enable an injection into a DLA. Time synchronization to a master oscillator is implemented for the RF stations driving the gun and the traveling wave structures. The setup allows for control of the phases of the accelerating fields in the gun and the traveling wave structures relative to each other to achieve longitudinal electron bunch compression. The photo cathode laser is locked to the same master oscillator making the injection of the bunch into a designed phase of the accelerating fields of the gun possible. The DLA drive laser will also be synchronized to the master oscillator to achieve control over the relative arrival times of the electron beam and the laser pulse at the interaction point. An arrival time jitter of the electron bunches of 10 fs was estimated in [100].

Before the interaction point a matching section will be situated to match the electron beam to the small transverse DLA aperture. A general purpose vacuum chamber will

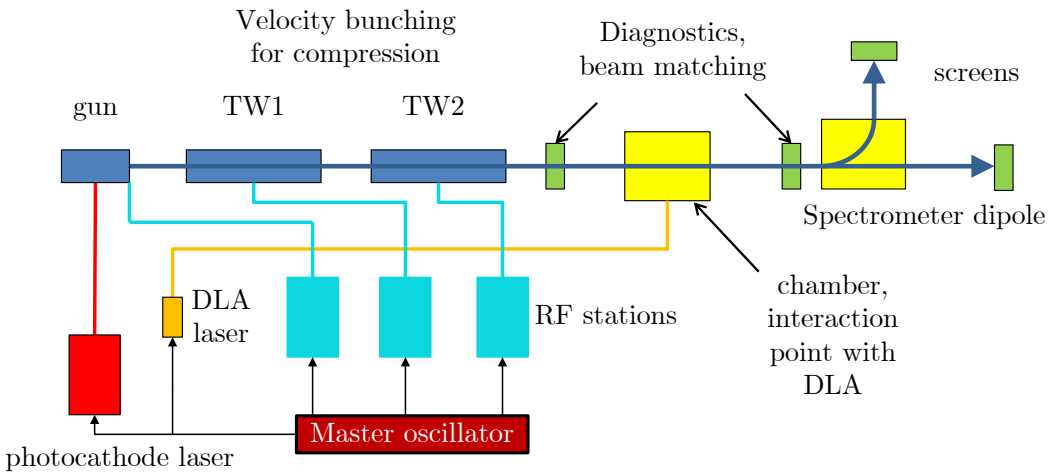

Figure 5.1: The schematic of the experimental setup shows the relevant parts of the accelerator necessary to conduct the experiment. The synchronization of all accelerator drive components to one master oscillator allows the velocity bunching and to overlap the ps DLA drive laser pulse with the fs electron bunch at the interaction point.

be installed after the traveling wave structures that can house various experiments and is equipped with different diagnostics for the electron beam and the laser. Another matching section will capture the beam after the experimental chamber that can be matched to a straight beam line with a screen. This path can be used to examine the transverse beam profile at the interaction point by imaging the beam onto the screen. To characterize the spectral properties of the electron beam a spectrometer dipole is used. Its dispersion makes it possible to map particle energies to transverse position on a screen downstream. A schematic illustration of the experimental setup can be seen in figure 5.1.

If an overlap of the DLA drive laser pulse and the electron bunch in the DLA is achieved, the energy spectrum of the electrons is altered in a characteristic way. A comparison to the energy spectrum with a blocked drive laser beam allows to draw conclusions about the field properties inside the DLA. To our best knowledge, DLA experiments in this fashion were only conducted with electron bunches orders of magnitude longer than the drive laser wavelength leading to a characteristic sinusoidal energy modulation in longitudinal direction. This experiment aims at the injection of a single-digit fs electron bunch into a DLA allowing to probe the single cycle properties of the accelerating fields and potentially showing first net energy gain of relativistic electrons in a grating-type dielectric laser accelerator.

5.2 Predicted Performance of the Experiment

The first task is to find a working point for the ARES linac using ASTRA simulations. The design goals for the working point are small emittance, low energy spread and high mean energy with the main goal of maximum longitudinal compression at the interaction point. The main goal of the bunch compression is necessary to be as close to a quarter of the period of the DLA drive laser as possible to be able to proof net acceleration of the particle bunch. The emittance requirement translates into a minimal achievable transverse focus at the interaction point to match the DLA aperture. And the energy spread of the beam should be below or close to the energy modulation depth the DLA interaction will induce. A high average energy of the particle beam minimizes the influence of space charge effects when the bunch is compressed and transversely focused at the same time at the interaction point.

The phase and amplitude in the gun were set so that the created particle beam experiences the highest integrated field. The initial bunch length set by the photo-cathode laser pulse length is chosen to be 100 fs to ensure uniform longitudinal field throughout the bunch length. The RMS laser spot size on the cathode is 50 µm. The cathode laser spot size and the initial bunch length influence the initial emittance. They should be as small as possible to minimize the initial emittance. The limitation is a charge dependent space charge effect increasing with smaller bunch length and spot size, thus increasing initial emittance. The lowest achievable values specified for pulse length and spot size give the lowest emittance for the 0.5 pC working point. The charge per bunch extracted from the cathode depends on the laser pulse energy.

In a systematic approach the phase and amplitude of the RF fields in the first traveling wave structure were scanned to maximize compression at the interaction point at $z = 16.972\,\mathrm{m}$, while keeping the injection phase and amplitude in the second traveling wave structure constant at maximum energy gain. To ensure small emittance the solenoid after the gun was scanned to achieve a matching to the transverse forces in the traveling wave accelerator structures.

A quadrupole triplet in the experimental area after the second traveling wave structure was simulated in ocelot [101] to focus the beam in horizontal x-direction as small as possible while keeping the vertical y-direction focus small enough to match the assumptions posed in chapter 2. The table 5.1 gives the resulting beam parameters at the interaction point.

With the transverse beam sizes achieved still only a fraction of the charge will be transmitted through the grating aperture. A significant part of the beam will pass through the dielectric. The stopping power for electrons at that energy in fused silica and silicon is low so a charging of the dielectric is only expected from ionization and knock-on electrons. The electrons that go through the substrate material will loose energy due to ionization and bremsstrahlung and will scatter. To estimate the charging, scattering and energy loss G4beamline [102] monte-carlo simulations were performed. Figure 5.2 shows the relevant data from the simulation. A 1 mm substrate is passed by a zero emittance electron beam with the expected particle energy at the interaction

Table 5.1: ARES Working Point at the interaction point for the DLA experiment from ASTRA/ocelot simulations

Charge	0.5 pC
Mean Energy	99.82 MeV
rms Energy spread	178 keV
norm. transverse Emittance x	45 nm
norm. transverse Emittance y	38 nm
rms beam size x	2.04 µm
rms beam size y	9.73 µm
bunch length FWHM	1.6 fs

point. The angle, position and momentum of the scattered electrons are recorded and used to model the behavior of electrons passing through the dielectric substrate in the start-to-end simulations. The electron and positron balance shows that the charging of the dielectric is negligible.

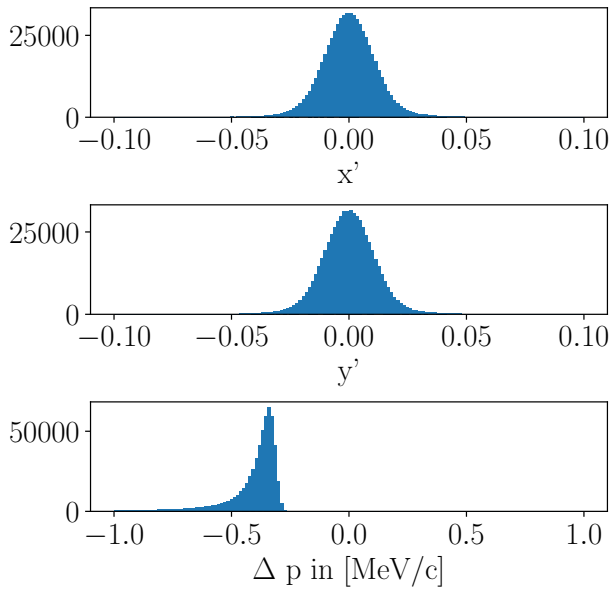

Figure 5.2: The first two plots show the scattering in x' and y' of a zero emittance point beam after passing one millimeter of bulk fused silica. The third plot shows the energy loss from the same interaction. The data are used to model scattering and energy loss of the fraction of the electron beam that is not passing the DLA channel.

A Ho:YLF amplifier system from Q-peak is planned to be the drive laser for the DLA experiments at ARES. It runs at 2050 nm wavelength and comprises a commercial Holmium fiber oscillator from Menlo systems seeding a chirped pulse amplification multi-pass amplifier stage with an etalon-enhanced bandwidth and a single pass amplifier stage [28]. The repetition rate of the system can be one or five kHz. A Kagome-fiber can be used to further compress the output of the amplifier to around 500 fs [29]. Table 1.2 shows the measured laser pulse parameters. More details on the laser system are included in chapter 1.

The DLAs are illuminated from only one side. Later on a pulse front tilt setup is planned to increase the absolute energy gains achievable as shown in [45]. Maximum acceleration gradients of about one GV/m are expected using the output from the laser system described above. The expected absolute energy gains are between hundreds of keV with the direct ps output from the Ho:YLF amplifier and 1 MeV with the pulse front tilted compressed pulse from the Kagome-fiber.

The properties of the bunch after the linac and at the interaction point are illustrated in figure 5.3.

Since the arrival time jitter will be significantly larger than the drive laser period the injection phases in the DLA will be randomly distributed over multiple shots. Particle tracking simulations using the method from [80] show very good agreement with analytical calculations for shorter interaction lengths. The calculated data in figure 5.4 shows that the energy spectrum of the electrons after the interaction with the DLA varies depending on the injection phase. For certain phases a net energy gain or loss can be observed when most particles in the bunch are injected on crest. A shot-to-shot analysis of the electron bunches is necessary to sort out which shots belong to which injection phase. Also, if the achievable bunch length at the interaction point is shorter than one drive laser period an average bunch length can be calculated from multiple spectra. For an assumed gaussian longitudinal bunch shape the minimal detectable bunch length is around 1.6 fs limited by the spectrometer resolution of around 5 keV. Bunches longer than one laser period of 6.8 fs will just have a double horn spectrum and no bunch length can be calculated. Later on with the TDS installed a bunch length measurement comparable to the method described in [103] can be implemented that is single-shot compatible.

A transverse jitter correlates to a scaling of the total charge transmitted through the DLA aperture. A peak transmission of 44 % of the charge is estimated. Due to the extent of the matching section almost all of the charge not passing the aperture will be lost during beam transport to the screens behind the spectrometer dipole. The non-interacting beam was matched to the screen at the straight section behind the dipole spectrometer to show that an image of the shadow of the DLA aperture is detectable and can be used for alignment. The beam line configuration and resulting front view of the beam are illustrated in figure 5.5.

To measure the spectrum the beam was matched with minimal β_x to the screen after the bend of the spectrometer dipole. The dispersion introduced by the dipole correlates the transverse position to the energy deviation enabling the capturing of the spectrum

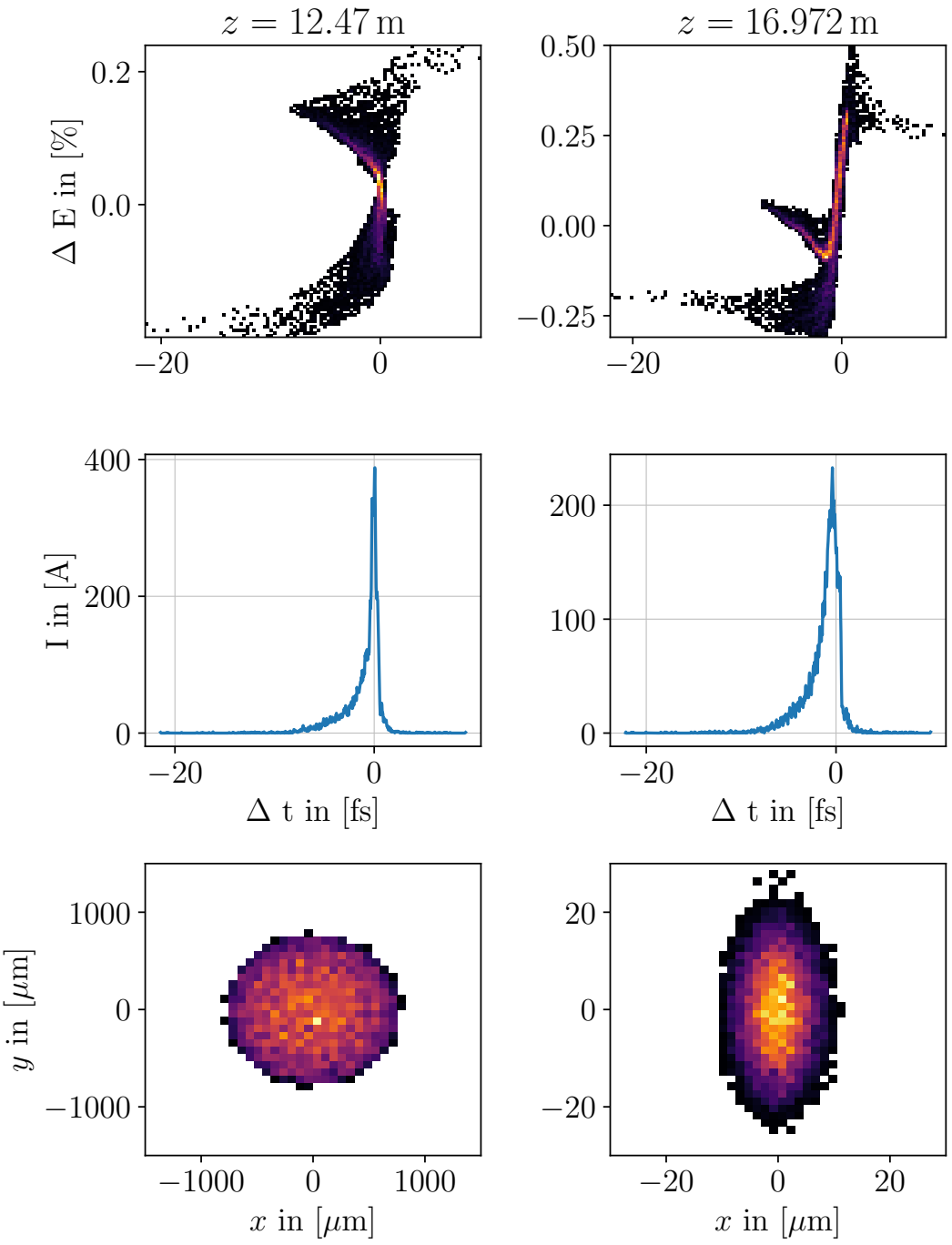

Figure 5.3: The longitudinal phase space, current profile and real space front view of the particle bunch after the linac at $z = 12.47\,\mathrm{m}$ (right) and at the interaction point at $z = 16.972\,\mathrm{m}$ (left).

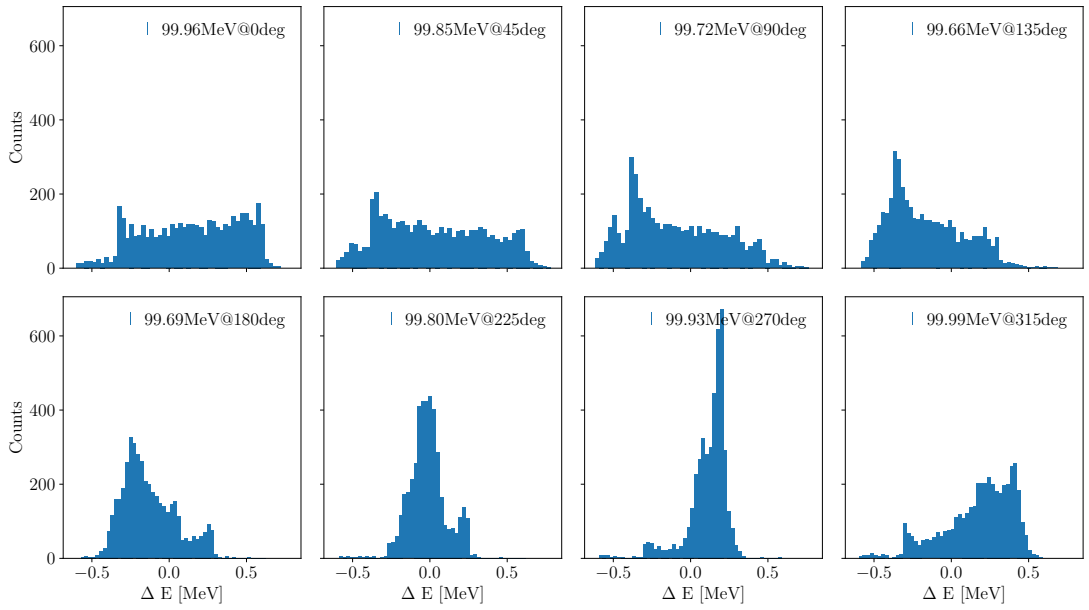

Figure 5.4: Different particle energy spectra after the DLA interaction depending on the random injection phase due to arrival time jitter. A conservative modulation depth of 300 keV is assumed. Electron to laser phases at 135° and 315° show net acceleration/deceleration. Phases at 45° and 225° show an increase/decrease in energy spread. This is due to a chirp of the electron bunch at the interaction point. The correlation in longitudinal phase space is either compensated or increased dependent on the longitudinal slope of the accelerating fields. A position jitter of the beam translates into a lower transmission. It is estimated that a maximum of 44 % of the charge pass through the aperture.

of the particle bunch. In the figure 5.6 the particle distributions on the screen after the bend of the dipole spectrometer are shown for an angle of 47° from the straight beam line.

5.3 Implementation of the Experiment

The experiments are foreseen to take place at the ARES linac. An experimental area named EA1 is situated behind the second traveling wave structure TW2. The DLA drive laser is installed in the photocathode laser lab and is transported in its own laser beam line to the experimental area. The cathode laser oscillator and the drive laser oscillator will be locked to the same master oscillator. A pulse picker will enable a matching to the repetition rate of the linac. The IR laser beam line is a double focal length imaging system with a beam pointing stabilizer to resume operation smoothly after start-up or

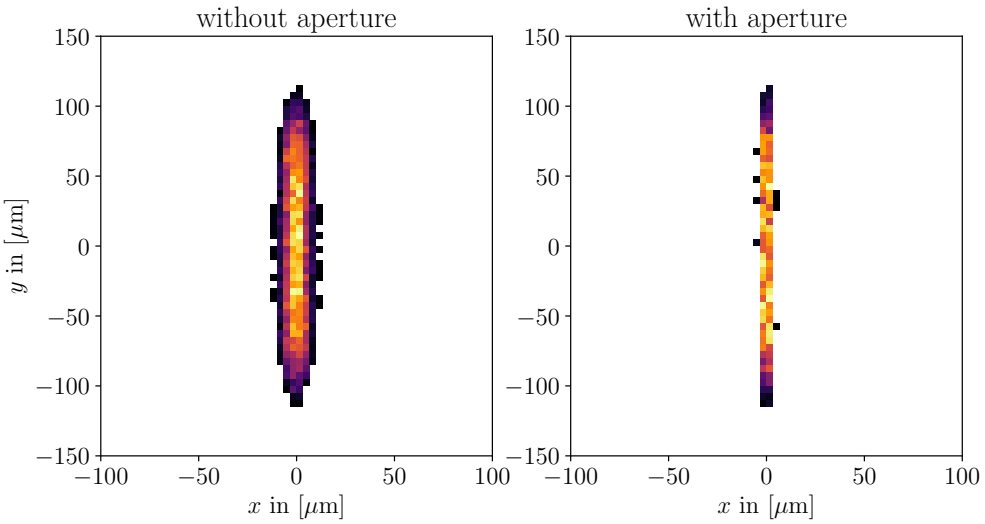

Figure 5.5: Front view of the electron beam imaged onto the straight screen behind the dipole spectrometer without and with an aperture from the DLA interaction. Since the scattered electrons are lost almost entirely during beam transport to the screen the aperture of the DLA can be well imaged.

interruptions. An overview of the setup can be seen in figure 5.7.

An optical table is placed next to the vacuum chamber holding the diagnostics for the beam pointing stabilization. A periscope is necessary since the laser beam has to be transported over the electron beam line and then returned back to particle beam height. The incident laser power on the DLA can be controlled via a motorized half wave plate and a thin film polarizer. The motorized telescope including a toroidal lens to create an asymmetric focus on the DLA and a fine delay stage to control the laser to electron overlap are also on the optical table. Cameras are foreseen to image the transported laser beam and to image the transmission through the DLA in order to align the diffraction pattern from the grating with the zero order transmission to make sure normal laser incidence on the DLA is achieved.

Electron beam diagnostics are included in the vacuum chamber mounted on a physics instruments hexapod for alignment. A high resolution fluorescent screen is used to measure the small electron beams transverse properties at the interaction point. Another method in collaboration with PSI [105] using very thin wire scanners [106] is also foreseen. A transition radiation measurement [107] with an optical spectrometer can be used to estimate longitudinal properties of the electron bunches. The optical spectrometer might be used for the detection of SPR from the passive grating DLA passed by the electron bunch as described in section 4.2 of this work.

The main dielectric accelerating structure is a fused silica double grating alike the one used in [42] with an aperture close to the wavelength. The exact parameters of the grating are visualized in figure 2.6 and table 3.1. The gratings were designed to balance

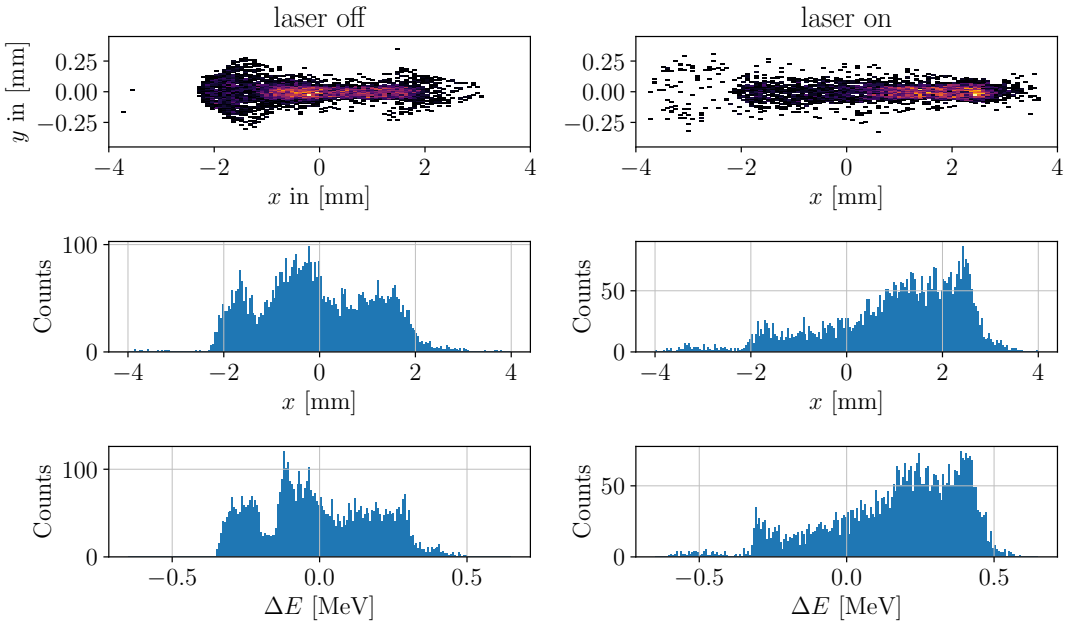

Figure 5.6: Front view of the beam at the screen after the bend of the spectrometer dipole. The left column shows the laser off case and the right one the laser on case for an injection that shows net energy gain. The binning of the histograms corresponds to the theoretically achievable resolution of 5 keV. Again due to the loss of the scattered electrons the spectrum corresponds only to the electrons which interacted with the DLA fields in the aperture.

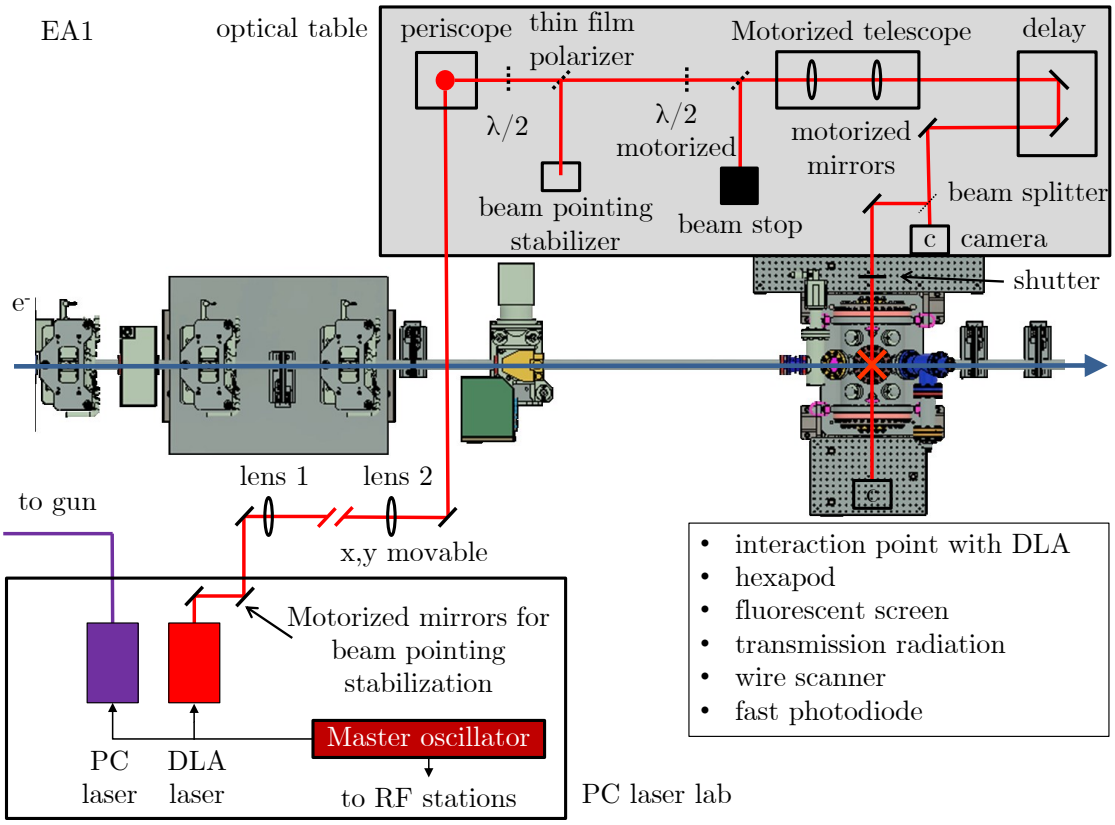

Figure 5.7: The relevant optical equipment and laser and electron beam diagnostics necessary to conduct the experiment. Most parts are already delivered and are in commissioning. Further details on the electron beam diagnostics can be found in [104] by Frank Mayet.

the transmission through the aperture with the achievable acceleration (see chapter 3).

The fused silica samples were produced by the Solgaard group of Stanford University within the ACHIP collaboration. Similar samples were produced for the experiments at SwissFEL, PSI [108]. Figure 5.8 shows a schematic of a single chip. The manufacturing recipe illustrated in 5.9 uses a fused silica wafer as base (a). In the first step a trench is patterned using photo-lithography. The trench is etched in using a plasma etching technique (b). The etch depth will set the gap C between the two gratings after bonding. After this step the grating is patterned into the trench using photo-lithography and is etched using hydrofluoric acid (c). In the illustration the sample is rotated by 90° (d). Additional trenches are patterned and etched next to the grating area. Gold and tin pads are deposited into these trenches (e) and then the wafers are cut into 1 mm x 3 mm chips. Two of the prepared grating chips are aligned and set together using eutectic bonding (f).

Another design in silicon was manufactured by the laser physics group at FAU Er-

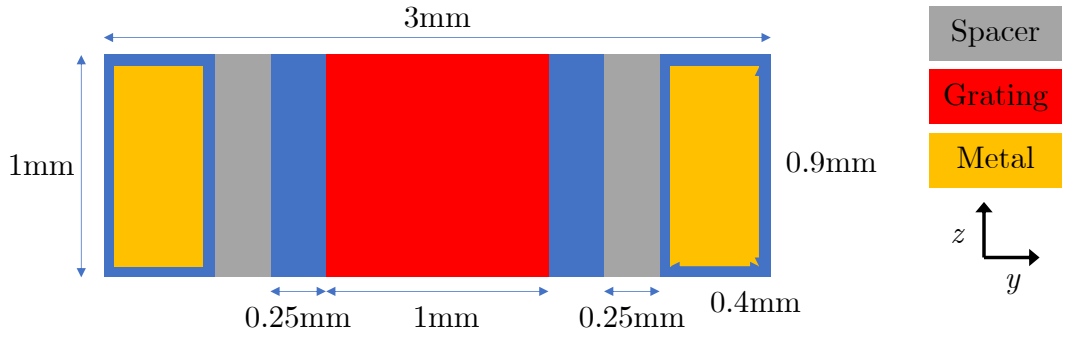

Figure 5.8: An overview of the DLA device produced by Solgaard group at Stanford. In the grating region is the actual optical grating with 2050 nm periodicity. The spacer regions define the gap between the two gratings and the metal regions are for eutectic bonding.

langen. The pillars are produced in a top down reactive ion etching process. Results of both manufacturing processes can be seen in figure 5.10 for the fused silica double gratings and in figure 5.11 for the silicon pillars.

5.4 Commissioning Status and Preliminary Plan for the Single-bunch Experiment

The ARES linac is still in its commissioning phase. The conditioning of the RF components of the gun and the traveling wave structures are happening currently. The electron beam line up to the spectrometer dipole and the vacuum chamber of EA1 will be installed in the coming weeks. The photo cathode laser system is synchronized to the master oscillator, but still needs some modifications to reach predicted performance. The Ho:YLF oscillator is under test to be locked to the master oscillator. The Ho:YLF amplifier system is still in commissioning after the equipment has been moved to the photocathode laser lab. The system is planned to be up and running by the end of 2019.

After all sub-systems are in operation the first tasks will be to characterize the gun performance. The next step is the testing of the traveling wave structures with electron beam. All the installations for the experimental setup are planned to be finished by the end of February 2020. The first DLA experiment are foreseen to be conducted mid 2020.

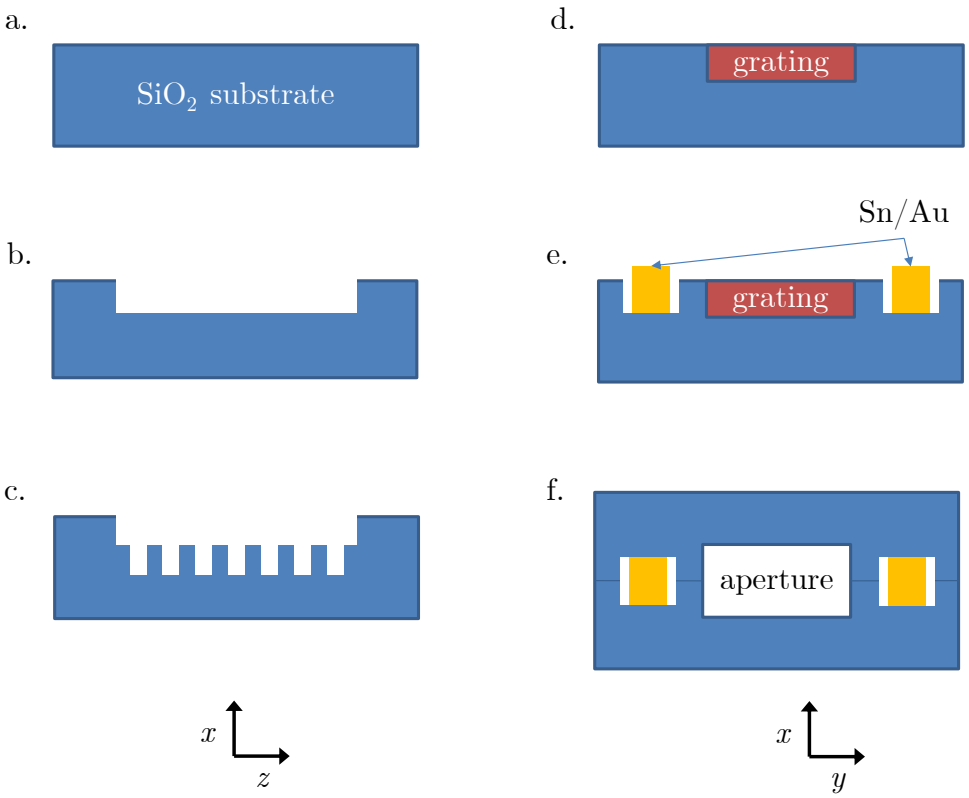

Figure 5.9: The base for the DLAs is a fused silica wafer (a). In the first step a trench is patterned using photo-lithography. The trench is manufactured using plasma etching (b). This etch depth will set the gap C between the two gratings after bonding. After this step the grating is patterned into the trench using photo-lithography and is etched using hydrofluoric acid (c). The sample in this illustration is rotated by 90° (d)Additional trenches are patterned and etched next to the grating area. Gold and tin pads are deposited into these trenches (e) and then the wafers are cut into 1 mm x 3 mm chips. Two of the prepared grating chips are aligned and set together using eutectic bonding (f). Process description from correspondence with Y. Miao, Stanford University.

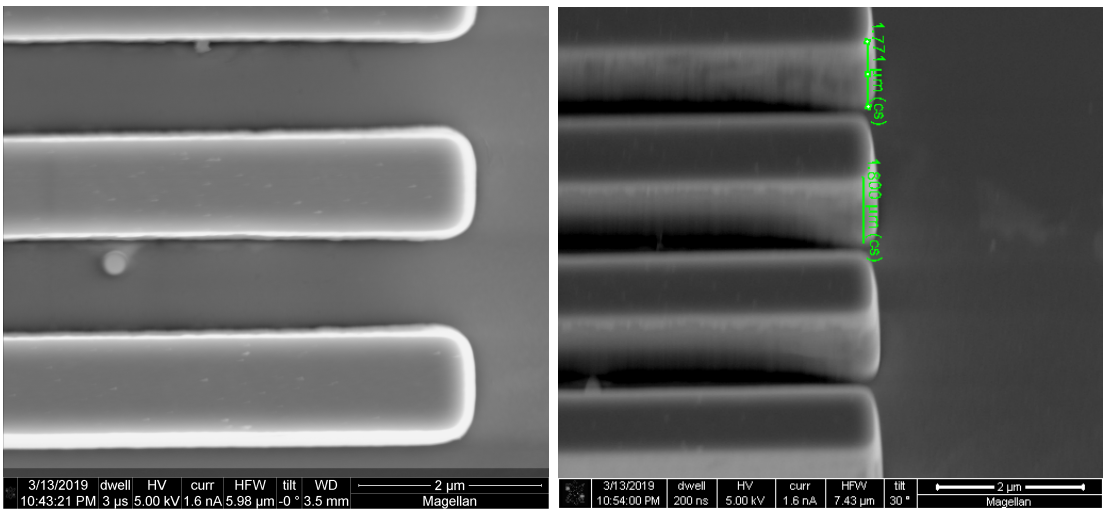

Figure 5.10: Scanning electron microscopy images of the fused silica structures produced by the Solgaard group at Stanford University. The left picture shows a detail of the grating in top view and the right picture shows a detail in perspective illustrating the depth. The chip has a grating length of 1 mm and the aperture is 1 µm or 2.3 µm, courtesy of Y. Miao, Stanford University.

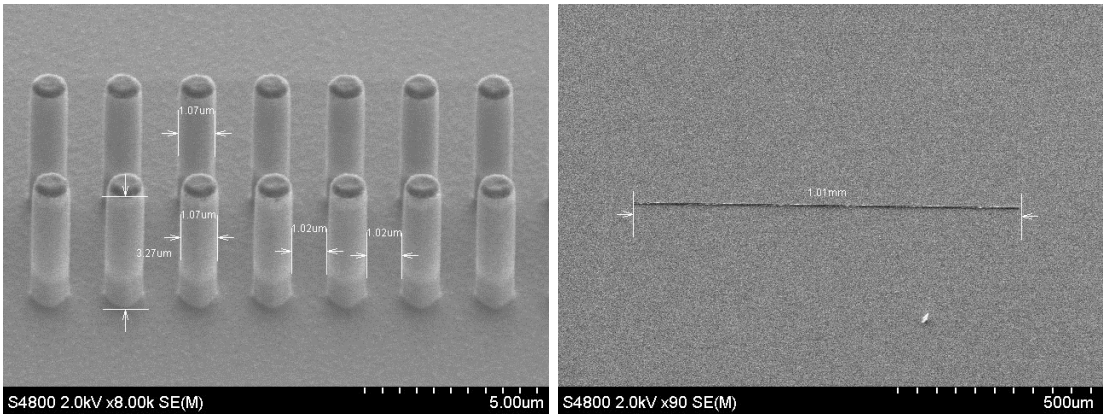

Figure 5.11: Scanning electron microscopy images of the silicon structures produced by the laser physics group at FAU Erlangen. The left picture shows a detail of the two pillar rows with approximate feature measurements. The limited height of the pillars of around 5 µm accounting for the projection in the image is apparent, violating the assumption of a uniform y-direction. The right picture shows an overview with the entire length of the structure of around 1 mm, courtesy of J. Illmer, FAU Erlangen.

5.5 Extension to Acceleration of a Microbunch Train

To mitigate the arrival time jitter a technique from seeded free electron lasers is planned to be employed. The drive laser is split into two arms. A permanent magnetic undulator is combined with one arm to imprint a longitudinal sinusoidal energy modulation onto a long electron bunch with a small energy spread. Downstream a permanent magnetic chicane is used to convert the energy modulation into a longitudinal charge density modulation. The second arm is used to drive the DLA. A schematic of the setup and the corresponding longitudinal phase space can be seen in Fig. 5.12. This setup reduces the timing jitter between the resulting micro-bunch train and the drive arm of the laser to the phase stability between the two laser arms. The setup is tens of cm long, thus the phase stability is expected to be below the period of the laser.

This scheme has a theoretical maximum bunching factor of 60 %. A significant amount of charge will still be spread out over the whole period of the drive laser. The larger part of the charge is in the set phase and thus can probe the fields in the device at a controlled phase. An expected spectrum of the particle energy before and after the DLA interaction is shown in figure 5.13. A more detailed discussion of the scheme can be found in [109].

The next step is to use a DLA to replace the undulator and achieve a sinusoidal energy modulation via DLA interaction with a longer electron bunch. The DLAs can also be used to optimize the microbunching because as proposed in section 4.2 the SPR from a second grating is coherently enhanced if it is passed by a microbunched beam. If a microbunching scheme via DLA is implemented one can take the scheme even further by introducing two bunching stages and potentially improve the charge capture rate to up to 96 % [110].

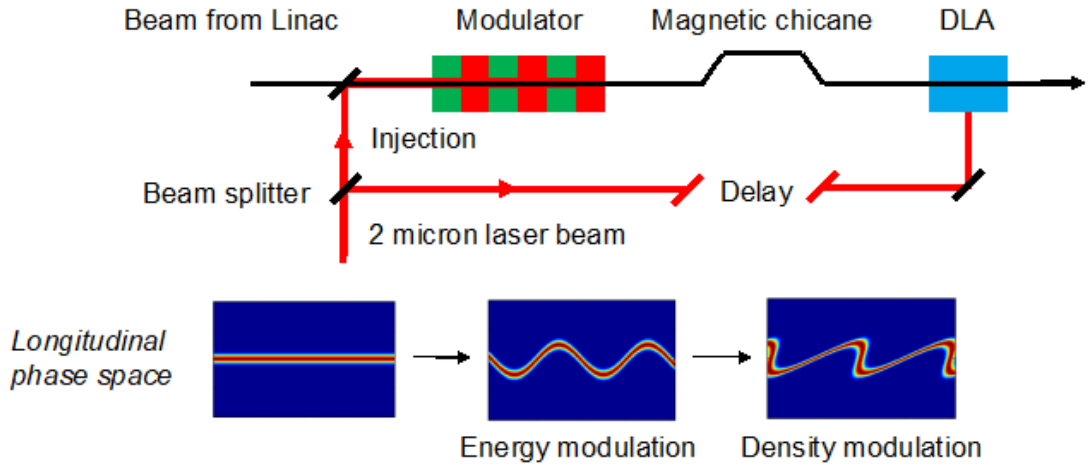

Figure 5.12: A schematic overview of the bunching scheme used to mitigate the arrival time jitter of the RF linac. A long low-energy-spread bunch is sinusoidally energy modulated in a permanent magnetic undulator combined with a laser. The energy modulation is converted to a longitudinal charge density modulation using a permanent magnetic chicane. The timing jitter is reduced to the phase stability between the two laser arms. Figure taken from [26] published by the author.

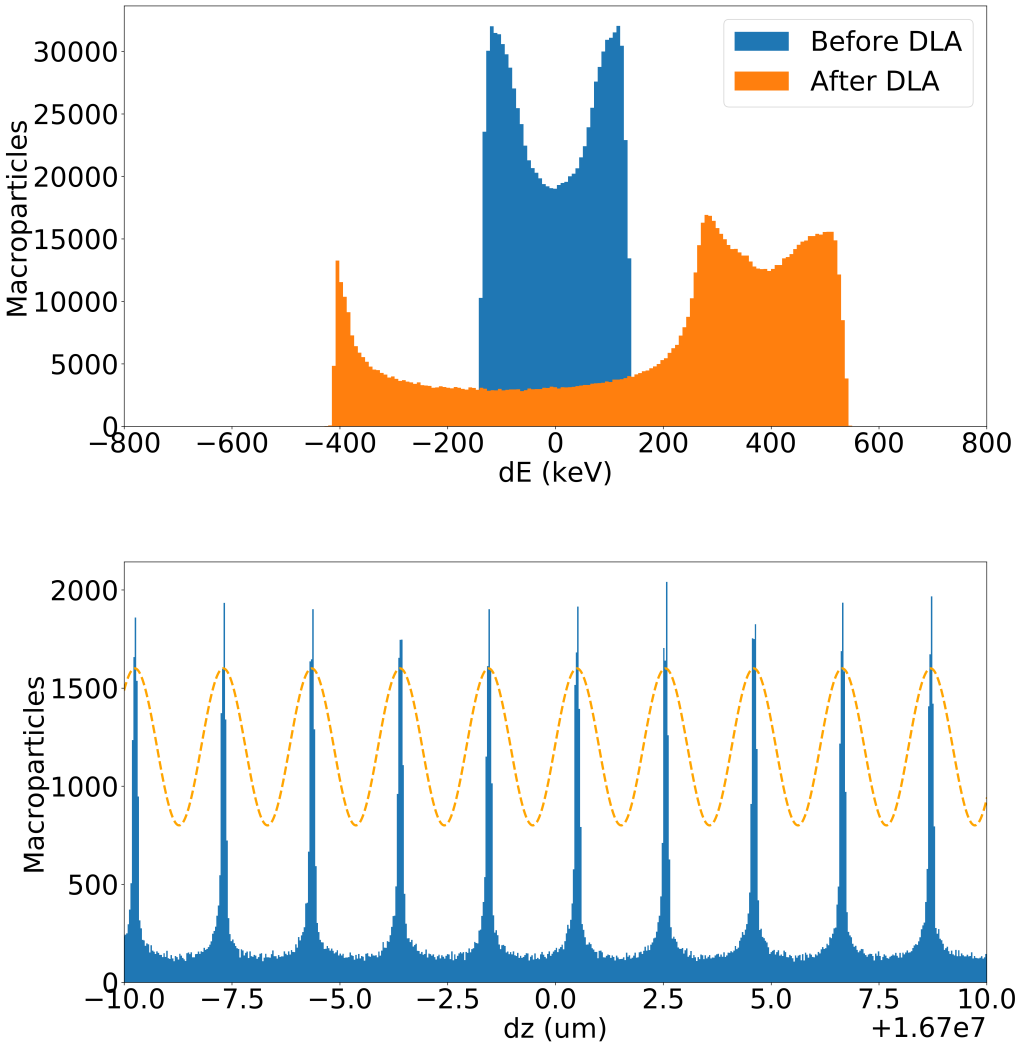

Figure 5.13: Since not all the charge is bunched into the buckets a part of the particles is decelerated or modulated in energy. The top figure shows the expected calculated energy spectra before and after the DLA interaction. The bottom figure shows the longitudinal charge density and the accelerating field overlapped. Figure taken from [26] published by the author.

6 Preparatory Short-pulse Laser-induced Damage Tests

Since the damage threshold of the materials used in DLA is one of the limiting factors for the achievable acceleration gradients the study of the material specific thresholds is an important preparatory task. Data have been published for several sets of parameters [111, 56, 73] and within the ACHIP collaboration a collection of yet unpublished data is available.

The characteristics of the laser amplifier system available at SINBAD differ from the already taken data. The achievable pulse lengths and the wavelength of the Ho:YLF amplifier differ from previous experiments. Thus, an experimental setup for threshold measurements is presented and the first round of data from the experiment and its analysis is shown.

6.1 Concept of the Experiment and Setup

The damage fluence as given in section 2.4 is the relevant quantity to measure in this experiment. To achieve this goal a row testing scheme is employed in which a number of samples is illuminated with a fixed pulse energy and afterwards the samples are analyzed w.r.t to the damage rate. The peak fluence incident on the samples that have a damage ratio of 50 % is identified as the damage threshold fluence. To be able to determine the peak fluence incident on the samples the laser beam properties have to be measured precisely.

Figure 6.1 shows a schematic of the setup designed and implemented within this work. Linear stages and a DAQ system are used to automate the data taking and characterization of the laser beam with LabVIEW to reduce manual read out errors. A half wave plate on a motorized rotational mount combined with a thin film polarizer is used to control the delivered pulse energy to the sample area. The split-of beam is used to monitor the pulse energy for drifts and to calibrate rotational mount position to transmitted pulse energy. A pyrocamera captures the beam after the sample area. The stages can support a knife edge or the samples enabling transmission measurements and knife edge scans. A shutter is used to control the exposure time and thus the number of pulses into the sample area. Two diodes can be connected to monitor the pulse-to-pulse change in transmission and to count the number of pulses. Both laser pulse lengths from the amplifier and Kagome-fiber can be delivered to the setup.

The properties of the laser beam using the 3 ps compressed amplifier output are shown

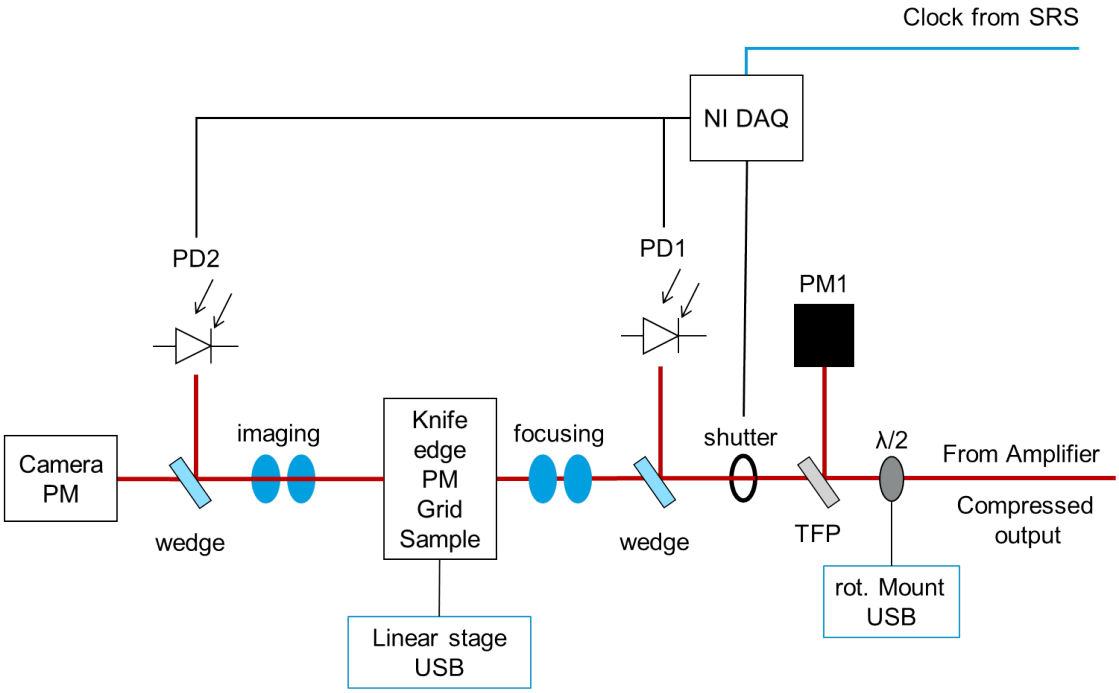

Figure 6.1: The shown setup can be used with the amplifier output or the compressed output from the Kagome-fiber. A motorized rotational mount with a half wave plate ($\lambda/2$) followed by a thin film polarizer (TFP) is used to control the power delivered to the sample area. A power meter (PM1) is used for calibration and to monitor the stability of the pulse energy. An iris shutter controls the exposure time or number of pulses to the sample. It is controlled by a data acquisition and control system (NI DAQ). The same DAQ takes the signals from two photo diodes before (PD1) and after the sample (PD2) triggered by the same delay generator (SRS) signal as the pockels cell of the Ho:YLF amplifier. From the diode signals the number of pulses per sample can be deducted. Also it is possible to detect the occurrence of damage if it is connected to a reduction in transmission to PD2. Focusing and imaging optics are used to set an appropriate focus on the sample in accordance with the expected damage fluence and available laser pulse energy. The sample area is equipped with a 3D motorized linear stage system. It can be used to do knife edge scans, it can hold a target for measuring the magnification of the imaging optics to the pyrocamera or it can hold samples under test. Since the damage fluence might be sensitive to surface and bulk defects it is necessary to do row testing. The setup was automatized to minimize read out and handling errors and make the row testing efficient.

in figure 6.2. A beam waist of 30 µm is achieved with a 100 mm CaF lens enabling a fluence of around 140 J/cm^2 with a pulse energy of 2 mJ. Using a 20 mm CaF lens the focal spot is imaged onto the pyrocam with a design magnification of around 49. This corresponds to a spot size on the camera chip of 5 mm. The pixel size of the pyrocam chip is 100 µm.

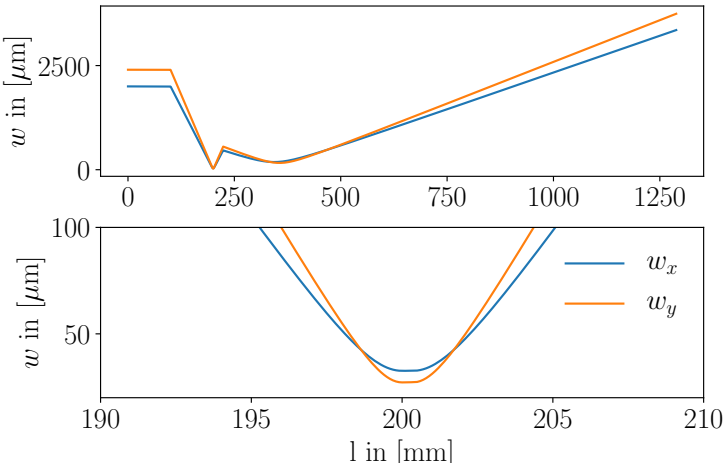

Figure 6.2: The optical path of the damage setup with a 100 mm focusing lens and a 20 mm imaging lens both made from CaF. The detail in the second plot shows the focal spot at which the sample is placed.

The knife edge scan data is fitted to the error function of a Gaussian distribution and scanned along the beam to give the beam size in dependence of the longitudinal position. This waist profile is fitted against the parabola relation:

$$w(z) = w_0^2(1 + (z - z0)^2(\frac{M^2\lambda_l}{\pi w_0^2})^2) \tag{6.1}$$

to give the beam waist w_0 and the quality factor M^2. Ten points are measured within the Rayleigh length Z_0 of around 4 mm of the focal spot and another ten measurements are taken outside of two times the Rayleigh length before and behind the focal spot. With the linear stages a set of measurements can be taken efficiently. Figure 6.3 illustrates the method.

6.2 The Experiment

The actual beam waists $w_x = 57.4 \pm 0.7 \mu m$ and $w_y = 54 \pm 3.4 \mu m$ and the M^2 measure of 1.75 ± 0.03 were measured using knife edge scans and least squares fitting to the parabola relation in equation 6.1. The large uncertainty on the beam waists is due to only a few

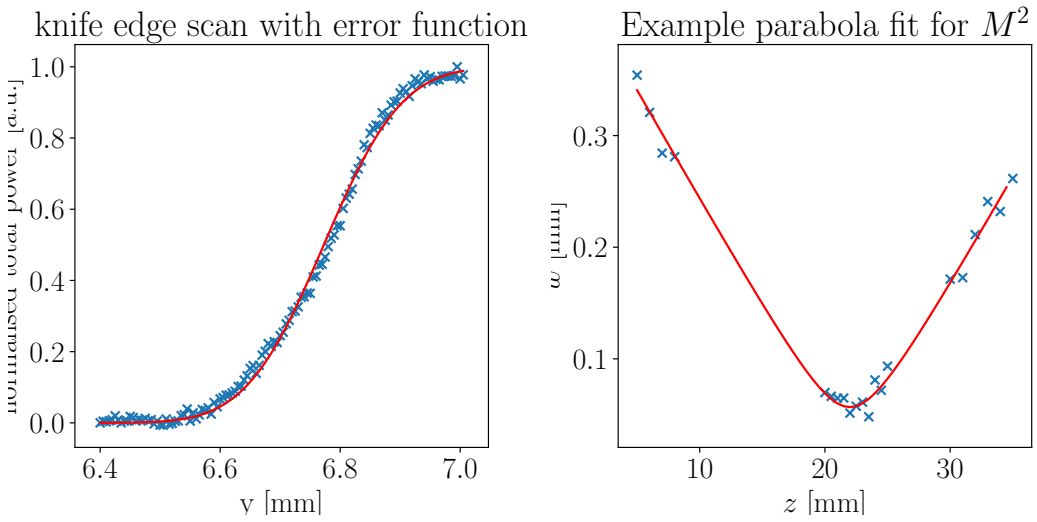

Figure 6.3: Example of a measured error function and parabola and the corresponding least squares fits.

data sets taken. The measurements show good agreement with calculations in reZonator [112] derived from camera measurements with the unfocused beam over the length of the measurement area taking the rather large M^2 measure into account. From these values and a drop in output power over the installation of the setup it was obvious that the laser amplifier was damaged. The damage turned out to be on one of the facet of the multi-pass amplifier Ho:YLF crystal. Due to the damaged facet only a preliminary test was conducted to validate the damage test setup.

Figure 6.4 shows the peak fluence on the sample placed in the focus as a function of the angle of the half wave plate. The uncertainties on the spot size measurement lead to significant uncertainties on this quantity. The maximum fluence was chosen w.r.t. the expected damage threshold of the samples used for the preliminary tests.

The samples used in this example study are 10 mmx10 mm cut outs of 525 µm polished silicon wafers in <100> orientation. This is one of the materials used by the laser physics group at FAU Erlangen to produce DLAs. The silicon samples covered in section 5.3 were manufactured from the same material. Silicon is a well studied material and also serves as a validation sample for our setup and methods. Sample holders to maximize the automation potential of the linear stages were produced using a 3D printer.

At 1 kHz and an exposure time of 500 ms the pulse energy was increased while scanning over the sample to find the region of interest for the pulse energy. Row tests were performed with a fixed pulse energy and a number of spots on the sample after the range was found to identify the damage ratio. A range of 6σ is set between each spot. An overview of a damaged sample is shown in figure 6.5 as well as a detail of several damaged spots.

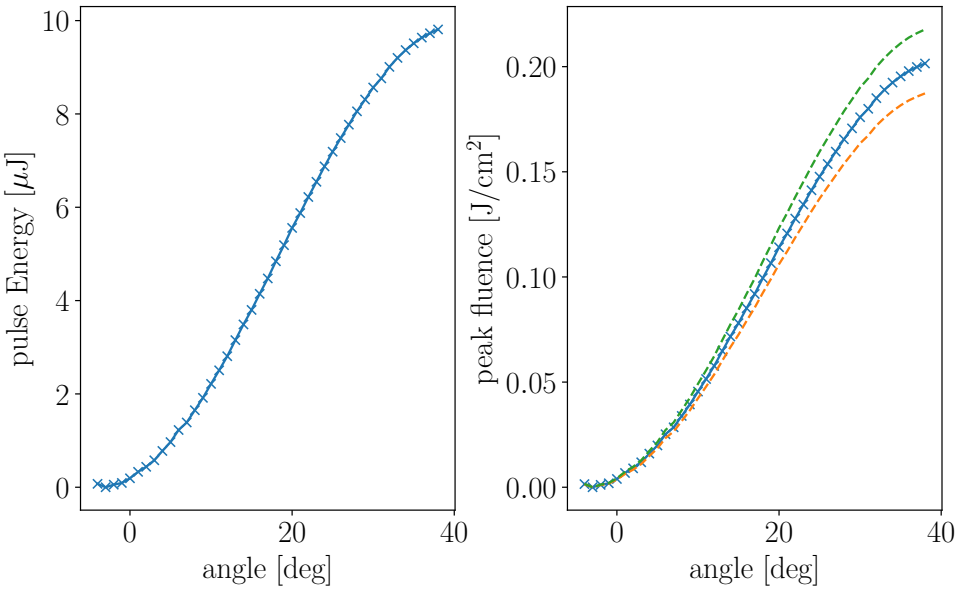

Figure 6.4: The left plot shows the measured pulse energy transmitted to the sample for 200 pulses over the angle of the rotational stage with the half wave plate. The error bars are too small to be visible. On the right side the incident peak fluence with an error range mainly from the uncertainty on the measurement of the focal spot size is plotted.

6.3 Results

Using the methods above the damage ratio of 76 % with 30 samples at a peak fluence of $(0.200 \pm 0.014)\,\mathrm{J/cm^2}$ according to figure 6.4 was determined. It was not possible to collect enough samples do determine the damage threshold of the test material. Unfortunately the laser system was not repaired immediately, but was moved to the ARES photocathode laser lab, where it is still in commissioning.

6.4 Discussion

The preliminary test has shown that the methods employed are suitable to conduct automated row testing of samples. It was possible to determine the damage ratio and subsequently draw a conclusion towards the peak fluence incident on the sample. The measurement of the laser beam waist has to be improved to narrow the uncertainty on the estimated peak fluence. One straight forward approach is to use the automated knife edge scan to take more data sets and see if the large deviation is due to the low number of data sets acquired. Another approach is to investigate if the beam size can

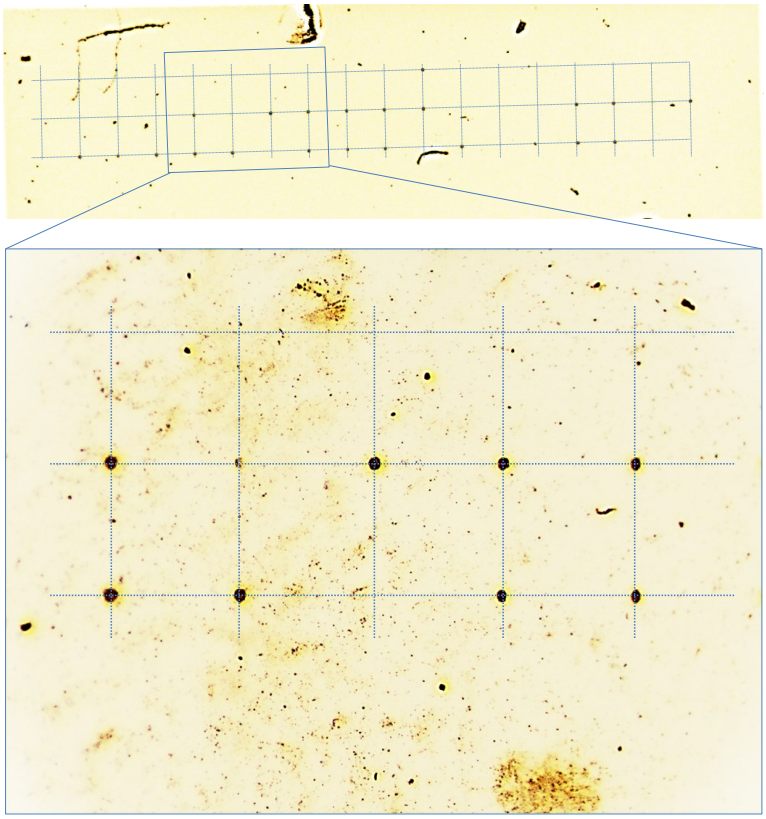

Figure 6.5: The top picture shows the contrast-enhanced color inverted image from an optical microscope of the area of the sample that was scanned to identify the region of interest for the incident power and then was illuminated at $(0.200 \pm 0.014)\,\mathrm{J/cm^2}$ on a number of spots. The sample was illuminated where the dotted lines cross. The bottom picture shows a detail using higher magnification.

be measured more precisely using the imaging to the camera. Additional equipment to build a telescope might be necessary due to the pixel size of the camera to achieve sufficient coverage of the chip. The setup also moved to the photo-cathode laser lab and will be recommissioned after the amplifier is up and running.

7 Conclusion

In the presented work various aspects of dielectric microstructures as electron accelerator components were investigated. Numerical methods were devised to efficiently simulate the interaction of electron beams with these structures. The performance of a transfer map based code was evaluated. The code speeds up calculation times by three orders of magnitude compared to PIC and is therefore well suited to simulate large interaction lengths of DLAs with hundred thousands of drive laser wavelengths with reasonable computation resource consumption. The simulation of such devices using particle-in-cell codes has been previously limited to hundreds of periods, thus the new approach opens up the possibility to design long interaction length DLAs. As an example a meter-long GeV-DLA was simulated for the first time. The injection parameters for an electron beam were derived specifying the challenging electron beam parameters necessary for injection into such a device.

Dielectric structures as electron beam manipulation and diagnostic devices were investigated. A longitudinally chirped dielectric grating device was proposed as a novel electron bunch length diagnostic. The studies show that this technology has the potential to deliver the means to measure the bunch length of sub-femto-second electron bunches by the characteristic Smith-Purcell-radiation. This is especially interesting for high particle energy facilities like free electron lasers, where only costly RF transverse deflecting structures are able to reach femto-second-resolutions and where high bunch charges would allow the employment of dielectric gratings as single shot, cheap and compact diagnostic devices. If the device is designed symmetrically then beam position information can be extracted from the measurement also. A calibration of the device with a DC particle beam potentially enables the extraction of the total charge information via the total radiated power. This can result in a very compact device in the order of centimeter length that would provide different useful information about the particle beam diagnosed and can be integrated with additional diagnostic capabilities. It is a non-destructive method that can be single-shot if the bunch charges are high enough. Potentially even a reconstruction of the longitudinal current profile is possible by using methods from Frequency Resolved Optical Gating to recover the relative phase information of the measured spectrum. A proof-of-principle experiment at ARES has been designed to validate the method. A prototype device should be developed, manufactured and tested in the near future.

An experiment to show first net energy gain of relativistic femtosecond electron bunches in a DLA was developed and designed in this PhD work. It leverages the excellent beam quality and short bunches that will be available from the state-of-the-art RF-photoinjector ARES. Parameter studies were performed to devise new grating DLA

designs. For the first time such designs were performed for the near infrared wavelength regime. The solutions are robust against manufacturing tolerances and balance charge transmission and achievable acceleration gradient. The structures were fabricated by our collaboration partners at FAU Erlangen and Stanford University. The expected performance of the experiment was studied via start-to-end simulations of the RF-injector and the diagnostic capabilities of the facility. The studies show that the experiment is predicted to show first ever net energy gain with GV/m peak acceleration gradients for relativistic electron beams. In addition the characteristic spectra of the electron bunches after the DLA interaction will allow for an estimate of the bunch length at the interaction point in a range of 1.6 fs to 6.8 fs. This might be the first method available to estimate the bunch length at ARES since the Polarix TDS will only be installed and commissioned end of the year 2020. By applying a pulse front tilt to the DLA drive laser it is potentially possible to show record absolute energy gains in a DLA of around 1 MeV in a millimeter long structure.

The arrival time jitter of the photoinjectors should be around ten femtoseconds and above. This is still longer than one wavelength of the drive laser system. The electron-to-drive-laser phase will be fluctuating randomly. Thus for the planned experiment a shot-to-shot analysis of the spectra is necessary. This drawback can be mitigated by using a longer electron bunch and splitting the drive laser to interact in a permanent magnetic undulator. This setup is called a laser modulator. In a permanent magnetic chicane the sinusoidal longitudinal phase space modulation from the laser modulator can be turned into a real space longitudinal charge density modulation, i.e. into a microbunch train. The other part of the drive laser pulse is used to drive the DLA. This should result in a much improved the synchronicity of the microbunch train with the accelerating fields in the DLA, thus reducing the arrival time jitter to the phase stability between the two drive laser arms. This concept can be extended to using another DLA to replace the laser modulator.

An automated experimental setup for testing the main limitation on acceleration gradients in DLA the damage threshold fluence was devised and implemented in the ARES laser lab. Automated row-testing to measure the damage threshold fluence can be conducted to verify the resilience of the DLA against short-pulse laser induced damage. First tests on plain a silicon sample to validate the experimental method and the setup were conducted and analyzed. The results show good agreement with the literature and the experience of our collaboration partners at FAU Erlangen and Stanford University.

Finally this work is one of the first steps into the new field of laser driven dielectric particle accelerators and the possibilities this technology can open up. It clearly points at the potential capabilities that dielectric microstructures exhibit as compact particle beam diagnostics and manipulation devices as well as being a candidate for GV/m acceleration gradients. DLAs together with compact RF particle sources might open up new applications for MeV electron beams in ultra-fast electron diffraction and microscopy or in radiation generation. That makes DLAs one of the technologies with the potential to significantly influence the future of particle accelerators towards new applications, more compact facilities and higher particle beam quality and ultra-short bunches.

Bibliography

[1] J. D. Cockcroft and E. T. S. Walton, "Experiments with High Velocity Positive Ions. (I) Further Developments in the Method of Obtaining High Velocity Positive Ions", *Proc. Roy. Soc. Lond.*, vol. A136, pp. 619–630, 1932. DOI:10.1098/rspa.1932.0107

[2] G. Ising, "Prinzip einer Methode zur Herstellung von Kanalstrahlen hoher Voltzahl", *Ark. Mat. Astron. Fys.*, vol. 18, no. 30, pp. 1–4, 1924.

[3] R. Wideroe, "Über ein neues Prinzip zur Herstellung hoher Spannungen", *Archiv für Elektrotechnik*, vol. 21, no. 4, pp. 387–406, 1928. DOI:10.1007/BF01656341

[4] E. O. Lawrence and M. S. Livingston, "The production of high speed light ions without the use of high voltages", *Phys. Rev.*, vol. 40, pp. 19–35, 1932. DOI:10.1103/PhysRev.40.19

[5] V. I. Veksler, "A new method of acceleration of relativistic particles", *J. Phys.*, vol. 9, pp. 153–158, 1945.

[6] N. Martensson and M. Eriksson, "The saga of max iv, the first multi-bend achromat synchrotron light source", *Nuclear Instruments and Methods in Physics Research Section A: Accelerators, Spectrometers, Detectors and Associated Equipment*, vol. 907, pp. 97 – 104, 2018. DOI:10.1016/j.nima.2018.03.018

[7] C. G. Schroer *et al.*, "PETRA IV: the ultralow-emittance source project at DESY", *Journal of Synchrotron Radiation*, vol. 25, no. 5, pp. 1277–1290, 2018. DOI:10.1107/S1600577518008858

[8] J. M. J. Madey, "Stimulated emission of bremsstrahlung in a periodic magnetic field", *Journal of Applied Physics*, vol. 42, no. 5, pp. 1906–1913, 1971. DOI:10.1063/1.1660466

[9] Z. Huang and K.-J. Kim, "Review of x-ray free-electron laser theory", *Phys. Rev. ST Accel. Beams*, vol. 10, p. 034801, 2007. DOI:10.1103/PhysRevSTAB.10.034801

[10] J. Rossbach, J. R. Schneider, and W. Wurth, "10 years of pioneering X-ray science at the Free-Electron Laser FLASH at DESY", *Physics reports*, vol. 808, pp. 1 – 74, 2019. DOI:10.1016/j.physrep.2019.02.002

[11] W. Decking and T. Limberg, "European XFEL Post-TDR Description", DESY, Tech. Rep. XFEL.EU TN-2013-004, 2013.

[12] D. A. Edwards, "The Conceptual Design Report for the TTF", https://flash.desy.de/tesla_technology_collaboration/tesla_documentation/.

[13] E. J. Minehara *et al.*, "Quasi-continuous wave operation of multi-megawatts electron beam in the JAERI superconducting RF linac FEL driver", in *Proceedings of the 1999 Particle Accelerator Conference (Cat. No.99CH36366)*, vol. 4, 1999, pp. 2459–2461 vol.4. DOI:10.1109/PAC.1999.792725

[14] P. Bambade *et al.*, "The International Linear Collider: A Global Project", *public*, 2019. DOI:10.3204/PUBDB-2019-01998

[15] O. S. Brüning *et al.*, *LHC Design Report*, ser. CERN Yellow Reports: Monographs. Geneva: CERN, 2004. DOI:10.5170/CERN-2004-003-V-1

[16] V. Baglin, G. Bregliozzi, J. M Jimenez, and G. Lanza, "Synchrotron Radiation in the LHC Vacuum System", 2011.

[17] M. Benedikt *et al.*, "Future Circular Collider", CERN, Geneva, Tech. Rep. CERN-ACC-2018-0057, 2018, published in Eur. Phys. J. ST.

[18] M. Riordan, "The demise of the superconducting super collider", *Physics in Perspective*, vol. 2, no. 4, pp. 411–425, 2000. DOI:10.1007/s000160050053

[19] R. Zennaro *et al.*, "High Power Tests of a Prototype X-Band Accelerating Structure for CLIC", in *Proceedings, 8th International Particle Accelerator Conference (IPAC 2017): Copenhagen, Denmark, May 14-19, 2017*, 2017, p. THPIK097. DOI:10.18429/JACoW-IPAC2017-THPIK097

[20] K. Flöttmann, "rf-induced beam dynamics in rf guns and accelerating cavities", *Phys. Rev. ST Accel. Beams*, vol. 18, p. 064801, 2015. DOI:10.1103/PhysRevSTAB.18.064801

[21] M. Dal Forno *et al.*, "rf breakdown tests of mm-wave metallic accelerating structures", *Phys. Rev. Accel. Beams*, vol. 19, p. 011301, 2016. DOI:10.1103/PhysRevAccelBeams.19.011301

[22] M. Kozák, T. Eckstein, N. Schönenberger, and P. Hommelhoff, "Inelastic ponderomotive scattering of electrons at a high-intensity optical travelling wave in vacuum", *Nature Physics*, vol. 14, p. 121, 2017. DOI:10.1038/nphys4282

[23] https://ard.desy.de/sinbad/, 19.11.2019 14:56.

[24] B. Marchetti *et al.*, "Status Update of the SINBAD-ARES Linac Under Construction at DESY", in *JACoW*, 8th International Particle Accelerator Conference, Copenhagen (Denmark), 14 May 2017 - 19 May 2017. Geneva: JACoW, 2017, p. 3. DOI:10.18429/JACoW-IPAC2017-TUPAB040

[25] N. Matlis *et al.*, "Acceleration of electrons in THz driven structures for AXSIS", *Nuclear instruments & methods in physics research / A*, vol. 909, pp. 27 – 32, 2018. DOI:10.1016/j.nima.2018.01.074

[26] W. Kuropka *et al.*, "Plans for dielectric laser accelerators at SINBAD", in *2018 IEEE Advanced Accelerator Concepts Workshop, ACC 2018 - Proceedings*, 2019. DOI:10.1109/AAC.2018.8659395

[27] D. Strickland and G. Mourou, "Compression of amplified chirped optical pulses", *Optics Communications*, vol. 56, no. 3, pp. 219 – 221, 1985. DOI:10.1016/0030-4018(85)90120-8

[28] K. Murari *et al.*, "Intracavity gain shaping in millijoule-level, high gain Ho:YLF regenerative amplifiers", *Opt. Lett.*, vol. 41, no. 6, pp. 1114–1117, 2016. DOI:10.1364/OL.41.001114

[29] K. Murari *et al.*, "Kagome-fiber-based pulse compression of mid-infrared picosecond pulses from a Ho:YLF amplifier", *Optica*, vol. 3, no. 8, pp. 816–822, 2016. DOI:10.1364/OPTICA.3.000816

[30] T. Tajima and J. M. Dawson, "Laser electron accelerator", *Phys. Rev. Lett.*, vol. 43, pp. 267–270, 1979. DOI:10.1103/PhysRevLett.43.267

[31] C. Joshi, W. B. Mori, T. Katsouleas, J. M. Dawson, J. M. Kindel, and D. W. Forslund, "Ultrahigh gradient particle acceleration by intense laser-driven plasma density waves", *Nature*, vol. 311, no. 5986, pp. 525–529, 1984.

[32] A. J. Gonsalves *et al.*, "Petawatt Laser Guiding and Electron Beam Acceleration to 8 GeV in a Laser-Heated Capillary Discharge Waveguide", *Phys. Rev. Lett.*, vol. 122, p. 084801, 2019. DOI:10.1103/PhysRevLett.122.084801

[33] N. Delbos *et al.*, "Lux – a laser–plasma driven undulator beamline", *Nuclear Instruments and Methods in Physics Research Section A: Accelerators, Spectrometers, Detectors and Associated Equipment*, vol. 909, pp. 318 – 322, 2018, 3rd European Advanced Accelerator Concepts workshop (EAAC2017). DOI:10.1016/j.nima.2018.01.082

[34] V. Libov *et al.*, "FLASHForward X-2: Towards beam quality preservation in a plasma booster", in *Nuclear instruments & methods in physics research / A*, vol. 909, 3rd European Advanced Accelerator Concepts Workshop, La Biodola, Isola d'Elba (Italy), 24 Sep 2017 - 30 Sep 2017. Amsterdam: Elsevier, 2018, pp. p. 80–83. DOI:10.1016/j.nima.2018.02.063

[35] B. Zeitler, "Phase Space Linearization and External Injection of Electron Bunches into Laser-Driven Plasma Wakefields at REGAE", Dissertation, Universität Hamburg, Hamburg, 2017, dissertation, Universität Hamburg, 2016. DOI:10.3204/PUBDB-2017-00801

[36] "Accelerator Technology Helmholtz Infrastructure", www.athena-helmholtz.de.

[37] J. P. Gordon, H. J. Zeiger, and C. H. Townes, "The Maser—New Type of Microwave Amplifier, Frequency Standard, and Spectrometer", *Phys. Rev.*, vol. 99, pp. 1264–1274, 1955. DOI:10.1103/PhysRev.99.1264

[38] K. Shimoda, "Proposal for an electron accelerator using an optical maser", *Appl. Opt.*, vol. 1, no. 1, pp. 33–35, 1962. DOI:10.1364/AO.1.000033

[39] E. Sistrunk *et al.*, "All Diode-Pumped, High-repetition-rate Advanced Petawatt Laser System (HAPLS)", in *Conference on Lasers and Electro-Optics*. Optical Society of America, 2017, p. STh1L.2. DOI:10.1364/CLEO_SI.2017.STh1L.2

[40] D. Cesar *et al.*, "High-field nonlinear optical response and phase control in a dielectric laser accelerator", *Communications Physics*, vol. 1, no. 1, p. 46, 2018. DOI:10.1038/s42005-018-0047-y

[41] J. Breuer and P. Hommelhoff, "Laser-Based Acceleration of Nonrelativistic Electrons at a Dielectric Structure", *Phys. Rev. Lett.*, vol. 111, p. 134803, 2013. DOI:10.1103/PhysRevLett.111.134803

[42] E. A. Peralta *et al.*, "Demonstration of electron acceleration in a laser-driven dielectric microstructure", *Nature*, vol. 503, no. 7474, pp. 91–94, 2013. DOI:10.1038/nature12664

[43] K. P. Wootton *et al.*, "Towards a Fully Integrated Accelerator on a Chip: Dielectric Laser Acceleration (DLA) From the Source to Relativistic Electrons", in *Proc. of International Particle Accelerator Conference (IPAC'17), Copenhagen, Denmark, 14-19 May, 2017*, ser. International Particle Accelerator Conference, no. 8. Geneva, Switzerland: JACoW, 2017, paper WEYB1, pp. 2520–2525. DOI:10.18429/JACoW-IPAC2017-WEYB1

[44] "Accelerator on a chip international program", achip.stanford.edu/, 18.12.2019 15:50.

[45] D. Cesar *et al.*, "Enhanced energy gain in a dielectric laser accelerator using a tilted pulse front laser", *Opt. Express*, vol. 26, no. 22, pp. 29 216–29 224, 2018. DOI:10.1364/OE.26.029216

[46] K. Soong *et al.*, "Electron beam position monitor for a dielectric microaccelerator", *Opt. Lett.*, vol. 39, no. 16, pp. 4747–4750, 2014. DOI:10.1364/OL.39.004747

[47] J. McNeur *et al.*, "Elements of a dielectric laser accelerator", *Optica*, vol. 5, no. 6, pp. 687–690, 2018. DOI:10.1364/OPTICA.5.000687

[48] R. J. England *et al.*, "Dielectric laser accelerators", *Rev. Mod. Phys.*, vol. 86, pp. 1337–1389, 2014. DOI:10.1103/RevModPhys.86.1337

[49] J. D. Jackson, *Classical electrodynamics; 3rd ed.* New York: Wiley, 1998.

[50] H. Wiedemann, *Particle accelerator physics; 4th ed.*, ser. Graduate texts in physics. Cham: Springer, 2015. DOI:10.1007/978-3-319-18317-6

[51] W. Kuropka, "Elektromagnetische Modellierung von Terahertz-Metaoberflächen und Goubau-Leitungen sowie Eruierung von Abstandsmessverfahren zur elektrooptischen Detektion evaneszenter Terahertz-Oberflächenwellen", Master's thesis, Technische Universität Kaiserslautern, 2015.

[52] T. Satogata, "USPAS Accelerator Physics course material", http://toddsatogata.net/2017-USPAS/, 2017.

[53] K. Floettmann, "Some basic features of the beam emittance", *Phys. Rev. ST Accel. Beams*, vol. 6, p. 034202, 2003. DOI:10.1103/PhysRevSTAB.6.034202

[54] C. McGuinness *et al.*, "Fabrication and Characterization of Woodpile Structures for Direct Laser Acceleration", *AIP Conference Proceedings*, vol. 1299, 2010. DOI:10.1063/1.3520360

[55] Z. Zhao *et al.*, "Design of a tapered slot waveguide dielectric laser accelerator for sub-relativistic electrons", *Opt. Express*, vol. 26, no. 18, pp. 22 801–22 815, 2018. DOI:10.1364/OE.26.022801

[56] C. M. S. Sears *et al.*, "Optical Wakefield from a Photonic Bandgap Fiber Accelerator", *Conf. Proc.*, vol. C070625, p. 3106, 2007, [,3106(2007)]. DOI:10.1109/PAC.2007.4440683

[57] B. Naranjo, M. Ho, P. Hoang, S. Putterman, A. Valloni, and J. B. Rosenzweig, "Photonic laser-driven accelerator for galaxie", *AIP Conference Proceedings*, vol. 1507, no. 1, pp. 488–492, 2012. DOI:10.1063/1.4773745

[58] R. J. England, C. K. Ng, R. J. Noble, J. E. Spencer, Z. Wu, and D. Xu, "Coupler Studies for PBG Fiber Accelerators", *Conf. Proc.*, vol. C110328, pp. 346–348, 2011.

[59] B. M. Cowan, "Three-dimensional dielectric photonic crystal structures for laser-driven acceleration", *Phys. Rev. ST Accel. Beams*, vol. 11, p. 011301, 2008. DOI:10.1103/PhysRevSTAB.11.011301

[60] J. McNeur, J. B. Rosenzweig, G. Travish, J. Zhou, and R. Yoder, "An Examination of Resonance, Acceleration, and Particle Dynamics in the Micro-Accelerator Platform", *AIP Conference Proceedings*, vol. 1299, pp. 427–432, 2010. DOI:10.1063/1.3520357

[61] A. Ceballos *et al.*, "Fabrication and Demonstration of a Silicon Buried Grating Accelerator", in *Proceedings, 6th International Particle Accelerator Conference (IPAC 2015): Richmond, Virginia, USA, May 3-8, 2015*, 2015. DOI:10.18429/JACoW-IPAC2015-WEPJE021

[62] J. Rosenzweig, A. Murokh, and C. Pellegrini, "A proposed dielectric-loaded resonant laser accelerator", *Phys. Rev. Lett.*, vol. 74, pp. 2467–2470, 1995. DOI:10.1103/PhysRevLett.74.2467

[63] N. V. Sapra, K. Y. Yang, D. J. F. Vercruysse, L. Su, and J. Vučković, "Waveguide-integrated dielectric laser particle accelerators through the inverse design of photonics", in *Conference on Lasers and Electro-Optics*. Optical Society of America, 2019, p. SM3J.2. DOI:10.1364/CLEO_SI.2019.SM3J.2

[64] T. W. Hughes *et al.*, "On-chip laser-power delivery system for dielectric laser accelerators", *Phys. Rev. Applied*, vol. 9, p. 054017, 2018. DOI:10.1103/PhysRevApplied.9.054017

[65] R. J. England, "Transverse dynamics in planar symmetric dielectric laser-driven accelerators", in *Advanced accelerator Concepts Workshop 2018*, 2018.

[66] M. C. Hutley, *Diffraction gratings*, ser. Techniques of physics. London: Academic Press, 1982, vol. 6.

[67] H. Talbot, "Lxxvi. facts relating to optical science. no. iv", *The London, Edinburgh, and Dublin Philosophical Magazine and Journal of Science*, vol. 9, no. 56, pp. 401–407, 1836. DOI:10.1080/14786443608649032

[68] J. Jahns and S. Helfert, *Introduction to micro- and nanooptics*, ser. Physics textbook. Weinheim: Wiley-VCH, 2012.

[69] J. D. Lawson, "Lasers and accelerators", *IEEE Transactions on Nuclear Science*, vol. 26, no. 3, pp. 4217–4219, 1979. DOI:10.1109/TNS.1979.4330749

[70] G. Floquet, "Sur les équations différentielles linéaires à coefficients périodiques", *Annales scientifiques de l'École Normale Supérieure*, vol. 2e série, 12, pp. 47–88, 1883. DOI:10.24033/asens.220

[71] L. Pilozzi, A. D'Andrea, and R. Del Sole, "Electromagnetic properties of a dielectric grating. I. Propagating, evanescent, and guided waves", *Phys. Rev. B*, vol. 54, pp. 10 751–10 762, 1996. DOI:10.1103/PhysRevB.54.10751

[72] J. Rosenzweig and L. Serafini, "Transverse particle motion in radio-frequency linear accelerators", *Phys. Rev. E*, vol. 49, pp. 1599–1602, 1994. DOI:10.1103/PhysRevE.49.1599

[73] K. Soong, R. Byer, E. R. Colby, R. England, and E. Peralta, "Laser damage threshold measurements of optical materials for direct laser accelerators", *AIP Conference Proceedings*, vol. 1507, 2012. DOI:10.1063/1.4773749

[74] L. Keldysh, "Ionization in the Field of a Strong Electromagnetic Wave", *JETP*, vol. 20, no. 5, p. 1307, 1965.

[75] B. C. Stuart, M. D. Feit, S. Herman, A. M. Rubenchik, B. W. Shore, and M. D. Perry, "Nanosecond-to-femtosecond laser-induced breakdown in dielectrics", *Phys. Rev. B*, vol. 53, pp. 1749–1761, 1996. DOI:10.1103/PhysRevB.53.1749

[76] R. W. Boyd, *Nonlinear optics; 3rd ed.* Amsterdam: Elsevier, 2008.

[77] K. P. Wootton *et al.*, "Demonstration of acceleration of relativistic electrons at a dielectric microstructure using femtosecond laser pulses", *Opt. Lett.*, vol. 41, no. 12, pp. 2696–2699, 2016. DOI:10.1364/OL.41.002696

[78] "CST", www.cst.com.

[79] W. Kuropka, R. Aßmann, U. Dorda, and F. Mayet, "Simulation of a Many Period Dielectric Grating-based Electron Accelerator", in *Proc. of International Particle Accelerator Conference (IPAC'17), Copenhagen, Denmark, 14-19 May, 2017*, ser. International Particle Accelerator Conference, no. 8. Geneva, Switzerland: JACoW, 2017, paper WEPVA005, pp. 3256–3259. DOI:10.18429/JACoW-IPAC2017-WEPVA005

[80] W. Kuropka, F. Mayet, R. Aßmann, and U. Dorda, "Full PIC simulation of a first ACHIP experiment @ SINBAD", *Nuclear Instruments and Methods in Physics Research Section A: Accelerators, Spectrometers, Detectors and Associated Equipment*, vol. 909, pp. 193 – 195, 2018, 3rd European Advanced Accelerator Concepts workshop (EAAC2017). DOI:10.1016/j.nima.2018.02.042

[81] F. Mayet, R. Aßmann, U. Dorda, and W. Kuropka, "A Fast Particle Tracking Tool for the Simulation of Dielectric Laser Accelerators", in *Proc. of International Particle Accelerator Conference (IPAC'17), Copenhagen, Denmark, 14-19 May, 2017*, ser. International Particle Accelerator Conference, no. 8. Geneva, Switzerland: JACoW, 2017, paper THPAB013, pp. 3716–3719. DOI:10.18429/JACoW-IPAC2017-THPAB013

[82] U. Niedermayer, T. Egenolf, and O. Boine-Frankenheim, "Beam dynamics analysis of dielectric laser acceleration using a fast 6D tracking scheme", *Phys. Rev. Accel. Beams*, vol. 20, p. 111302, 2017. DOI:10.1103/PhysRevAccelBeams.20.111302

[83] F. Pedregosa *et al.*, "Scikit-learn: Machine learning in Python", *Journal of Machine Learning Research*, vol. 12, pp. 2825–2830, 2011.

[84] T. Egenolf, U. Niedermayer, and O. Boine-Frankenheim, "Intensity Limits by Wakefields in Relativistic Dielectric Laser Acceleration Grating Structures", in *2018 IEEE Advanced Accelerator Concepts Workshop (AAC)*, 2018, pp. 1–5. DOI:10.1109/AAC.2018.8659426

[85] T. Q. Jia *et al.*, "Ultraviolet-infrared femtosecond laser-induced damage in fused silica and CaF_2 crystals", *Phys. Rev. B*, vol. 73, p. 054105, 2006. DOI:10.1103/PhysRevB.73.054105

[86] D. A. Swenson, "Alternating phase focused linacs", *Part. Accel.*, vol. 7, pp. 61–67, 1976.

[87] U. Niedermayer, T. Egenolf, O. Boine-Frankenheim, and P. Hommelhoff, "Alternating-phase focusing for dielectric-laser acceleration", *Phys. Rev. Lett.*, vol. 121, p. 214801, 2018. DOI:10.1103/PhysRevLett.121.214801

[88] F. Mayet, R. Aßmann, U. Dorda, and W. Kuropka, "Using short drive laser pulses to achieve net focusing forces in tailored dual grating dielectric structures", *Nuclear Instruments and Methods in Physics Research, Section A: Accelerators, Spectrometers, Detectors and Associated Equipment*, vol. A909, pp. 208–212, 2018. DOI:10.1016/j.nima.2018.01.095

[89] F. Mayet, R. Aßmann, U. Dorda, W. Kuropka, B. Marchetti, and J. Zhu, "Simulations and Plans for a Dielectric Laser Acceleration Experiment at SINBAD", in *Proc. of International Particle Accelerator Conference (IPAC'17), Copenhagen, Denmark, 14-19 May, 2017*, ser. International Particle Accelerator Conference, no. 8. Geneva, Switzerland: JACoW, 2017, paper WEPVA007, pp. 3264–3267. DOI:10.18429/JACoW-IPAC2017-WEPVA007

[90] K. Flöttmann, "ASTRA - A Space Charge Tracking Algorithm", www.desy.de/~mpyflo/, 1997.

[91] F. Mayet, R. Aßmann, U. Dorda, and W. Kuropka, "Simulation of phase-dependent transverse focusing in dielectric laser accelerator based lattices", *Journal of Physics: Conference Series*, vol. 1067, p. 042002, 2018. DOI:10.1088/1742-6596/1067/4/042002

[92] F. Ji, J. G. Navarro, P. Musumeci, D. B. Durham, A. M. Minor, and D. Filippetto, "Knife-edge based measurement of the 4D transverse phase space of electron beams with picometer-scale emittance", *Phys. Rev. Accel. Beams*, vol. 22, p. 082801, 2019. DOI:10.1103/PhysRevAccelBeams.22.082801

[93] W. Kuropka, R. Aßmann, U. Dorda, and F. Mayet, "Simulation of deflecting structures for dielectric laser driven accelerators", *Nuclear Instruments and Methods in Physics Research Section A: Accelerators, Spectrometers, Detectors and Associated Equipment*, vol. 909, pp. 196 – 198, 2018, 3rd European Advanced Accelerator Concepts workshop (EAAC2017). DOI:10.1016/j.nima.2018.02.032

[94] T. Plettner, R. L. Byer, C. McGuinness, and P. Hommelhoff, "Photonic-based laser driven electron beam deflection and focusing structures", *Phys. Rev. ST Accel. Beams*, vol. 12, p. 101302, 2009. DOI:10.1103/PhysRevSTAB.12.101302

[95] M. Röhrs, C. Gerth, H. Schlarb, B. Schmidt, and P. Schmüser, "Time-Resolved Electron Beam Phase Space Tomography at a Soft X-Ray Free-Electron Laser", *Physical review / Special topics / Accelerators and beams*, vol. 12, p. 13, 2009. DOI:10.1103/PhysRevSTAB.12.050704

[96] A. Ody, R. J. England, and Z. Huang, "Simulation of a dielectric deflecting structure for short-wavelength radiation", https://www.slac.stanford.edu/pubs/slacpubs/17250/slac-pub-17379.pdf.

[97] S. J. Smith and E. M. Purcell, "Visible Light from Localized Surface Charges Moving across a Grating", *Phys. Rev.*, vol. 92, pp. 1069–1069, 1953. DOI:10.1103/PhysRev.92.1069

[98] R. Trebino *et al.*, "Measuring ultrashort laser pulses in the time-frequency domain using frequency-resolved optical gating", *Review of Scientific Instruments*, vol. 68, no. 9, pp. 3277–3295, 1997. DOI:10.1063/1.1148286

[99] B. Marchetti *et al.*, "X-Band TDS Project", in *International Particle Accelerator Conference (8th)*, 8th International Particle Accelerator Conference, Copenhagen (Denmark), 14 May 2017 - 19 May 2017. Geneva: JACoW, 2017, pp. 184–187. DOI:10.18429/JACoW-IPAC2017-MOPAB044

[100] J. Zhu, "Design Study for Generating Sub-femtosecond to Femtosecond Electron Bunches for Advanced Accelerator Development at SINBAD", Dissertation, University of Hamburg, 2017, dissertation, University of Hamburg, 2017. DOI:10.3204/PUBDB-2018-01379

[101] "Accelerator, radiation and x-ray optics simulation framework", https://github.com/ocelot-collab/ocelot.

[102] T. Roberts, "G4beamline", http://www.muonsinternal.com/muons3/G4beamline.

[103] M. K. Weikum, G. Andonian, R. W. Assmann, U. Dorda, and Z. M. Sheng, "Reconstruction of sub-femtosecond longitudinal bunch profile measurement data", *Journal of Physics: Conference Series*, vol. 874, p. 012079, 2017. DOI:10.1088/1742-6596/874/1/012079

[104] F. Mayet, "Acceleration and Phase Space Manipulation of Relativistic Electron Beams in Nano- and Micrometer-Scale Dielectric Structures", Dissertation, Universtät Hamburg, Hamburg, 2019, dissertation, Universtät Hamburg, 2019. DOI:10.3204/PUBDB-2019-03861

[105] "Paul Scherrer Institut", https://www.psi.ch/en.

[106] S. Borrelli *et al.*, "Generation and measurement of sub-micrometer relativistic electron beams", *Communications Physics*, vol. 1, no. 1, p. 52, 2018. DOI:10.1038/s42005-018-0048-x

[107] B. Schmidt *et al.*, "Longitudinal Bunch Diagnostics using Coherent Transition Radiation Spectroscopy", arXiv:1803.00608, Tech. Rep. DESY-18-027; arXiv:1803.00608, 2018. DOI:10.3204/PUBDB-2018-01372

[108] E. Prat *et al.*, "Outline of a dielectric laser acceleration experiment at SwissFEL", *Nuclear Instruments and Methods in Physics Research Section A: Accelerators, Spectrometers, Detectors and Associated Equipment*, vol. 865, pp. 87 – 90, 2017, physics and Applications of High Brightness Beams 2016. DOI:10.1016/j.nima.2017.01.016

[109] F. Mayet *et al.*, "A Concept for Phase-Synchronous Acceleration of Microbunch Trains in DLA Structures at SINBAD", in *JACoW*, 8th International Particle Accelerator Conference, Copenhagen (Denmark), 14 May 2017 - 19 May 2017. Geneva: JACoW, 2017, pp. 3260–3263. DOI:10.18429/JACoW-IPAC2017-WEPVA006

[110] N. Sudar *et al.*, "Demonstration of Cascaded Modulator-Chicane Microbunching of a Relativistic Electron Beam", *Phys. Rev. Lett.*, vol. 120, p. 114802, 2018. DOI:10.1103/PhysRevLett.120.114802

[111] B. Cowan, "Optical Damage Threshold of Silicon for Ultrafast Infrared Pulses", *AIP Conference Proceedings*, vol. 877, no. 1, pp. 837–843, 2006. DOI:10.1063/1.2409223

[112] N. Chunosov, "reZonator", www.rezonator.orion-project.org.